Analysis Note for $\gamma p \to p\phi\eta$

Bradford E. Cannon

January 21, 2019

Table of Contents

1 Identification of $\gamma p \to pK^+K^-\gamma\gamma$ Events at GlueX

In order to study potential states of bound strangeonia, it is essential to properly identify all final and initial state particles. The final state topology that will be studied for this thesis is $\gamma p \to pK^+K^-\gamma_1\gamma_2$, where the K^+K^- pair are daughter states of the ϕ meson, and the $\gamma_1\gamma_2$ pair are daughter states of the η meson. Therefore, the beginning of this analysis section will focus on the particle identification of the proton, kaons, and final state photons, as well as the incident beam and target proton. Once identification of all particles has been well established, this analysis will then provide evidence that the final event sampling enforces exclusivity.

1.1 Spring 2017 Run Period

The data presented here is the result of the successful Spring 2017 Low Intensity run period. The Spring 2017 run period spanned from January 23rd to March 13th and accumulated roughly 50 billion physics events. The maximum electron beam energy used was 12 GeV, and the accelerator ran at 250 MHz while in low intensity (beam every 4 ns), and later ran at 500 MHz while in high intensity (beam every 2 ns). Upon entering Hall D, the electron beam was incident upon a radiator. During this run period, both amorphous and diamond radiators were used to produce either incoherent or coherent polarized bremsstrahlung radiation. The diamond radiator was experimentally set up to produce linear photon polarization at four different

angles; 0°, 45°, 90°, and 135°. These directions were chosen in order to provide the detector with a uniform sampling of linear polarization in the transverse direction to the incident beam. In order to yield roughly the same amount of statistics for an amorphous radiator run as compared to a diamond radiator run, a beam current of 150 nA was incident upon the amorphous radiator, while a beam current of 100 nA was incident upon the diamond radiator. Farther downstream, a 5mm collimator hole was used for all radiator configurations. Lastly, the collimated photon beam was incident upon a stationary liquid hydrogen target. This resulted in one petabyte of files and $16pb^{-1}$ of integrated luminosity.

1.2 Identification of Initial State Particles

1.2.1 Photon Beam

The first step in identifying the initial state beam photon is to select the correct beam bunch. Since the electron beam is delivered from the accelerator every four nanoseconds, the timing of when the beam particles arrive into the hall is well known and we call this the Radio Frequency (RF) time. In addition to the RF time, we also have the beam time. The beam time is defined as the time which the reconstruction converged upon a common vertex time. The common vertex time is found by using the final state charged tracks and the their timing, and back tracking them to a common point in space and time. Comparing the beam time with the RF time provides the experiment with the correct beam bunch which should be centered at zero. An example of what this distribution looks like and the cut used for it is given in Figure 1.
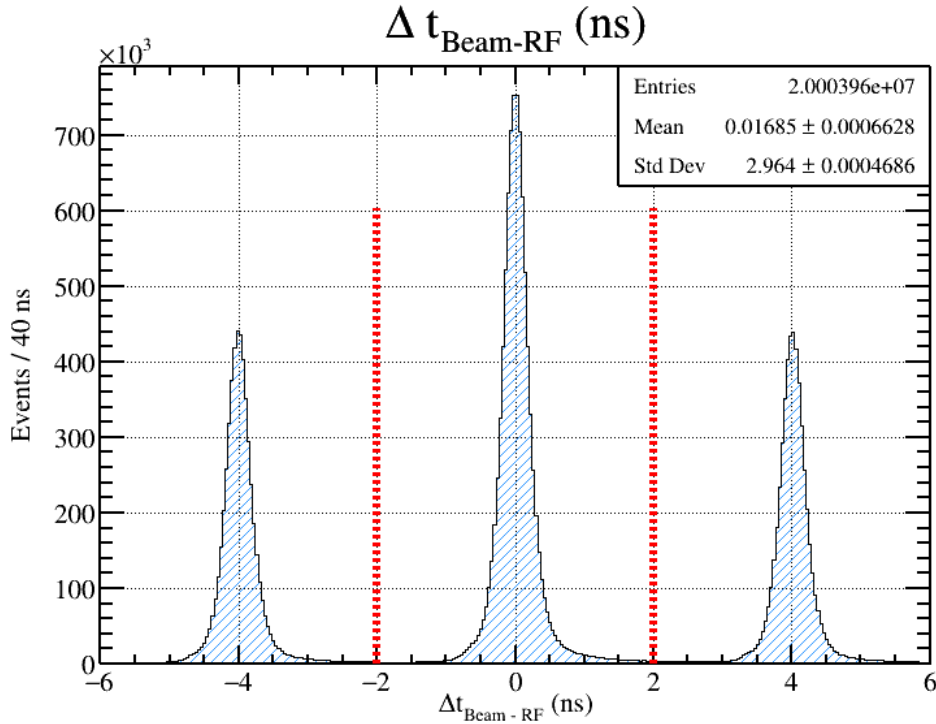
Figure 1: An example histogram of beam time as compared to the reported Radio Frequency (RF) time. In the plot there are three peaks, all of which are separated by four nanoseconds. Also included in the plot are two red dashed cut lines at ± 2 ns. These cut lines will select the beam time which agrees with the RF and will reject the other out of time beam particles.

The last cut that was made on the beam photons was the observed beam energy. Although this cut does not technically fall under the category of a particle identification, it is included in this section because it was used as a prerequisite for the rest of this analysis. Since this study will ultimately focus on a reaction which requires a high 't' momentum transfer, it is natural to only allow beam photons with high momentum to begin with. This, coupled with the fact that low energy photons produce low statistics for this channel, is the reason why a beam energy cut of $Beam_E \geq 7.5$ GeV was enforced early in the analysis. It should also be noted that this analysis will include a beam asymmetry study for strangeonia which will force the beam energy to be within the coherent peak region ($8.0 GeV - 8.8 GeV$). An example beam energy distribution with the associated cut is given in Figure 2.
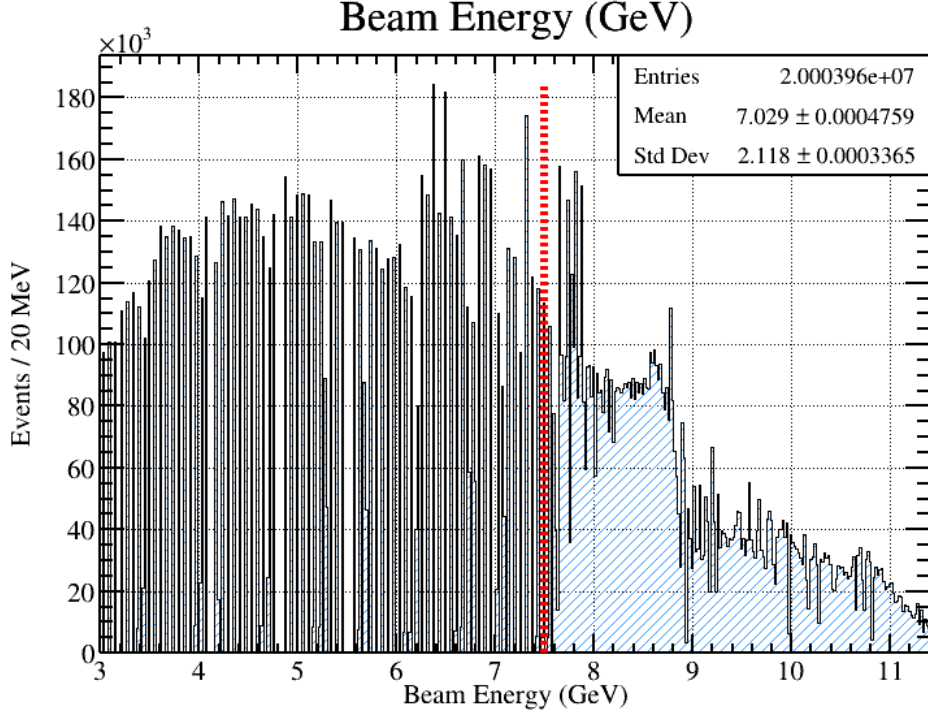
Figure 2: An example histogram of the beam energy distribution at GlueX. One can easily notice the large amount of statistics present around the coherent peak region ($8.0 GeV - 8.8 GeV$) and energies above it. Also contained in the image is a red dashed line which represents the cut value used on this data to select beam energies above 7.5 GeV.

1.2.2 Target Proton

There are two cuts needed to select the initial state proton. Both of these cuts enforce the reconstructed vertex for all final state particles to be within the geometric volume of the target chamber. Since this analysis does not contain a particle lifetime which would result in a detached vertex, it is imperative to remove backgrounds from other channels that may have this feature, such as excited baryons with a strange quark. An example of what the reconstructed vertex for the final state photons looks like in the z direction (along the beam direction) and in the x-y plane (transverse to the beam direction), as well as the associated cut values, is given in Figure 3.
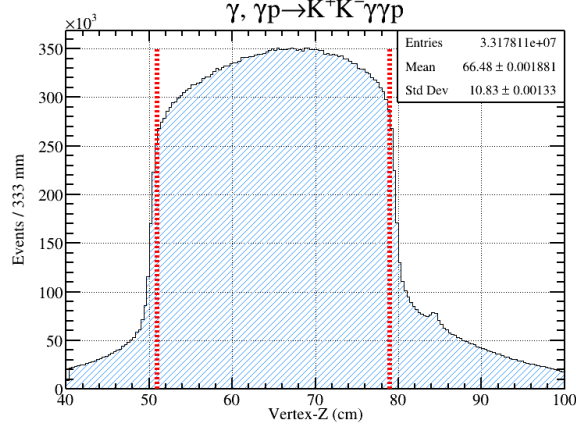
(a) Reconstructed vertex position along the beam direction for γ gamma candidates with cut lines at 51 and 79 cm.
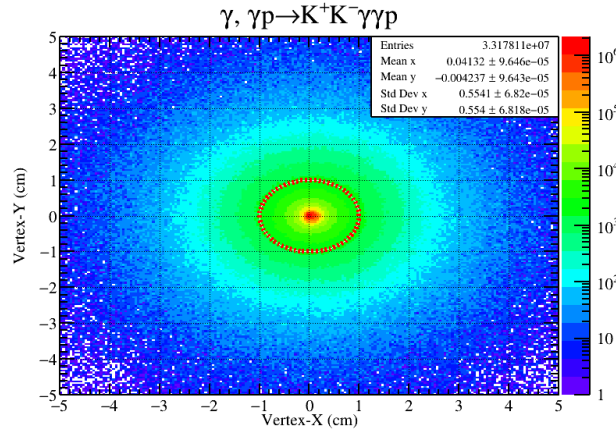
(b) Reconstructed vertex position transverse to the the beam direction for γ gamma candidates with cut a line at 1 cm in radial distance.

Figure 3: An example of what a reconstructed vertex distribution looks like for a final state γ in the reaction $\gamma p \to pK^+K^-\gamma_1\gamma_2$. The upper image is the reconstructed vertex position along the beam line, or z axis; and the lower image is the reconstructed vertex position in the directions transverse to the beam line. Both figures contain red dashed lines which represent the cut values for all reconstructed final state particles. In the z direction the cut values are $51cm \leq V_z \leq 79cm$, and in the transverse direction the cut values are $V_r \leq 1cm$. The z direction cut values are established from Log Entry 3456336 from a Spring 2017 empty target run. The transverse cuts are simply established by considering the geometric size of the target chamber.

1.3 Identification of Final State Particles

1.3.1 Recoil Proton

There are three cuts that were used to identify the recoil proton. One of the cuts is a standard dE/dX cut, which separates some of the slow moving protons from other particles of positive charge such as e^+, π^+, and K^+. Due to the higher mass of the proton in comparison to the other particles with positive charge, the proton will tend to lose more energy inside of the Central Drift Chamber. The second cut is to enforce the reconstructed vertex position of the charged proton track came from inside the target chamber. This cut is used to eliminate any background from particles that may have a detached vertex. The cut used is identical to those found and described in the Target section. The third and final cut that is used to identify the proton is the timing from the BCAL, FCAL, and TOF. An example of what these distributions look like as a function of momentum is given in Figure [4]. Since the data has a lot of pion background in these plots, it is difficult to determine what the proper timing cuts should be for all of the sub detectors. Due to this, a Monte Carlo sample of $\gamma p \rightarrow pX; X \rightarrow \phi\eta; \phi \rightarrow K^+K^-; \eta \rightarrow \gamma\gamma$ was generated and then reconstructed. This greatly reduces the background that is present in the timing plots and therefore can be used to estimate a proper timing cut for the proton and the sub detectors used to measure its time. Examples of these distributions and their associated projections onto the timing axis is given in Figure [5] through Figure [10]. A summary of all of the timing cuts used for the proton as well as all other final state particles is given in Table [1].
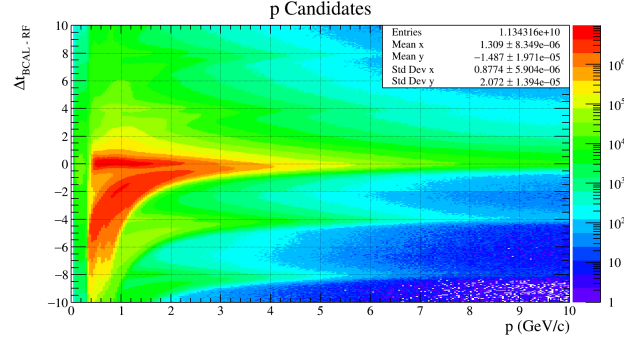
(a) Δ T Vs P for Proton candidates that have the Barrel Calorimeter as the timing detector.
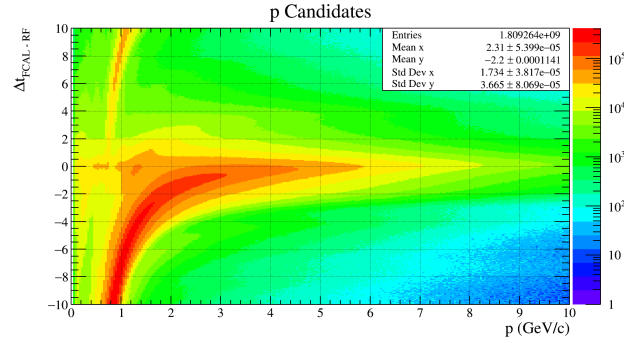
(b) Δ T Vs P for Proton candidates that have the Forward Calorimeter as the timing detector.
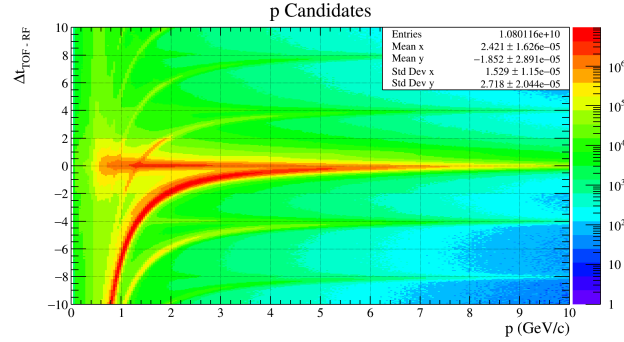
(c) Δ T Vs P for Proton candidates that have the Time of Flight as the timing detector.

Figure 4: Timing plots for proton candidates at GlueX. Protons are identified by selecting the horizontal band centered about $\Delta T = 0$. The curved line deviating below the horizontal proton line comes from miss identified π^+ tracks. The additional curved lines above and below $\Delta T = 0$ come from π^+ tracks that are associated with the wrong RF bunch.

Figure 5: A timing plot for generated protons after reconstruction. The horizontal axis is the reconstructed momentum of the proton and the vertical axis is the timing difference between the BCAL and RF. The enhancement of statistics in the lower right portion of the plot comes from miss identified kaons that were also included in the Monte Carlo.

Figure 6: A projection of the statistics from Figure [5] onto the vertical (timing) axis between the momentum range of 0.3-1.5 GeV/C. This projection range was chosen so that the distortion from the lower kaon band was minimized. A Gaussian fit was performed and is included in the figure where the mean and width of the distribution are given in the legend.
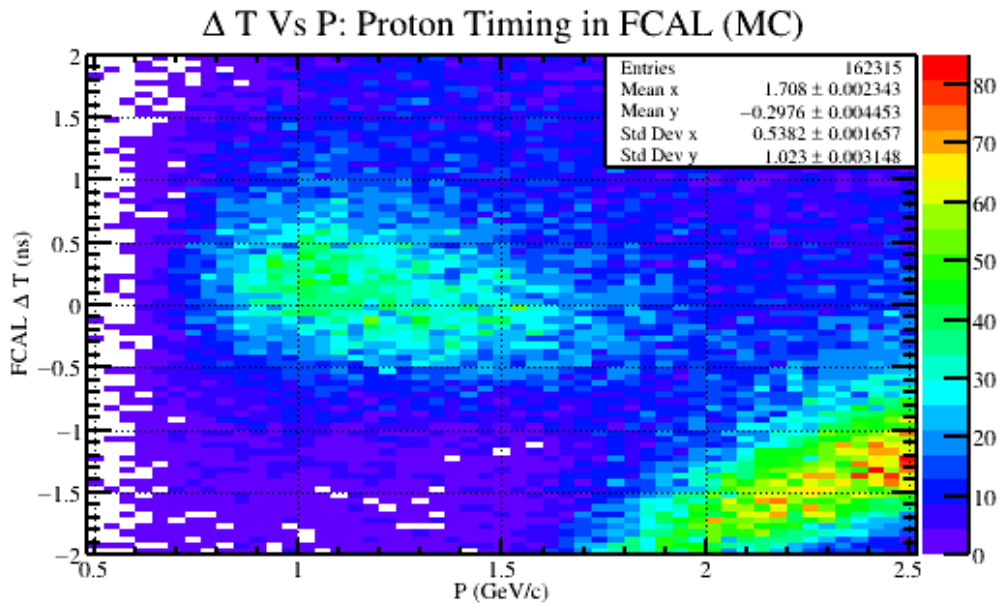
Figure 7: A timing plot for generated protons after reconstruction. The horizontal axis is the reconstructed momentum of the proton and the vertical axis is the timing difference between the FCAL and RF. The enhancement of statistics in the lower right portion of the plot comes from miss identified kaons that were also included in the Monte Carlo.

11
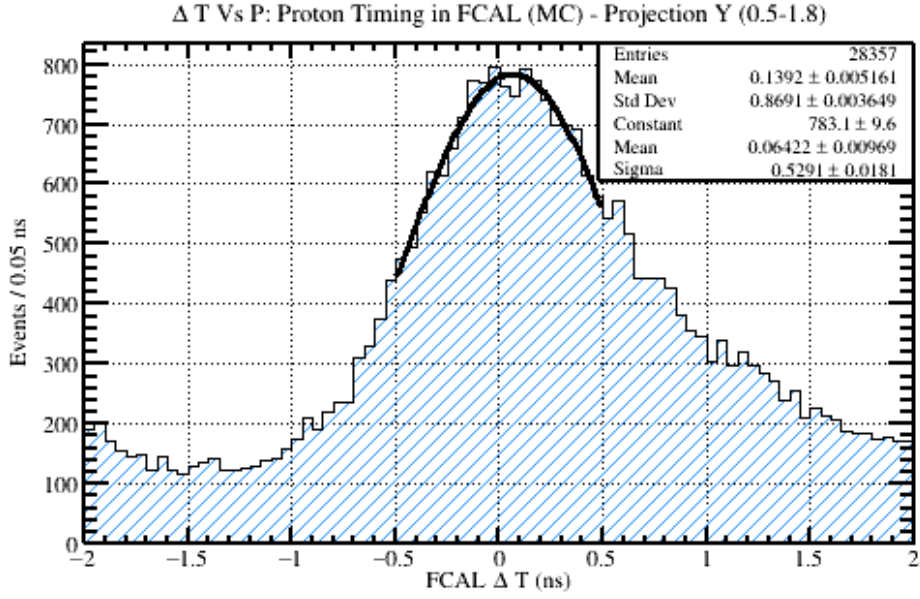
Figure 8: A projection of the statistics from Figure [7] onto the vertical (timing) axis between the momentum range of 0.5-1.8 GeV/C. This projection range was chosen so that the distortion from the lower kaon band was minimized. A Gaussian fit was performed and is included in the figure where the mean and width of the distribution are given in the legend.
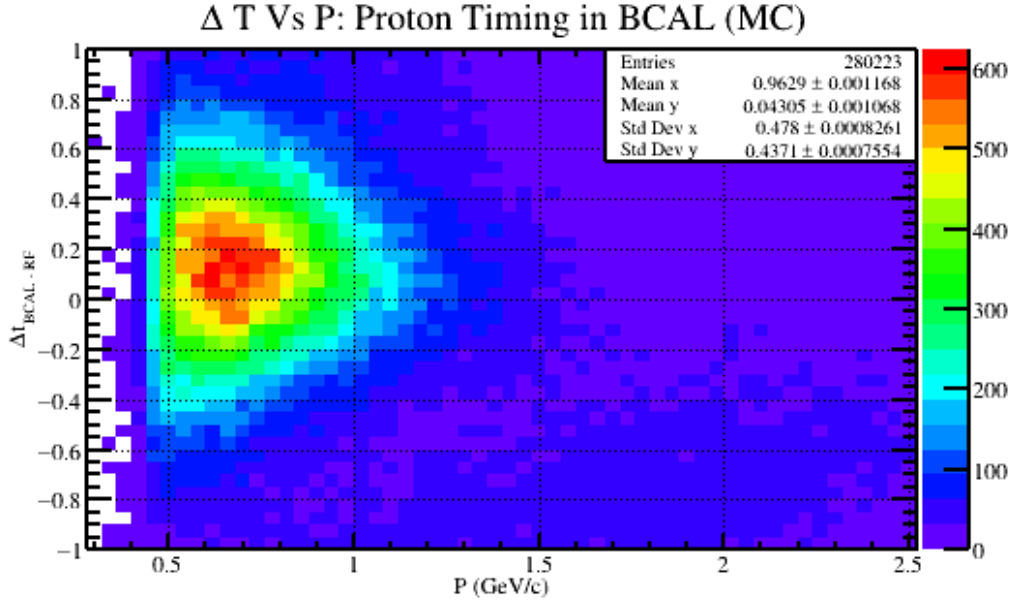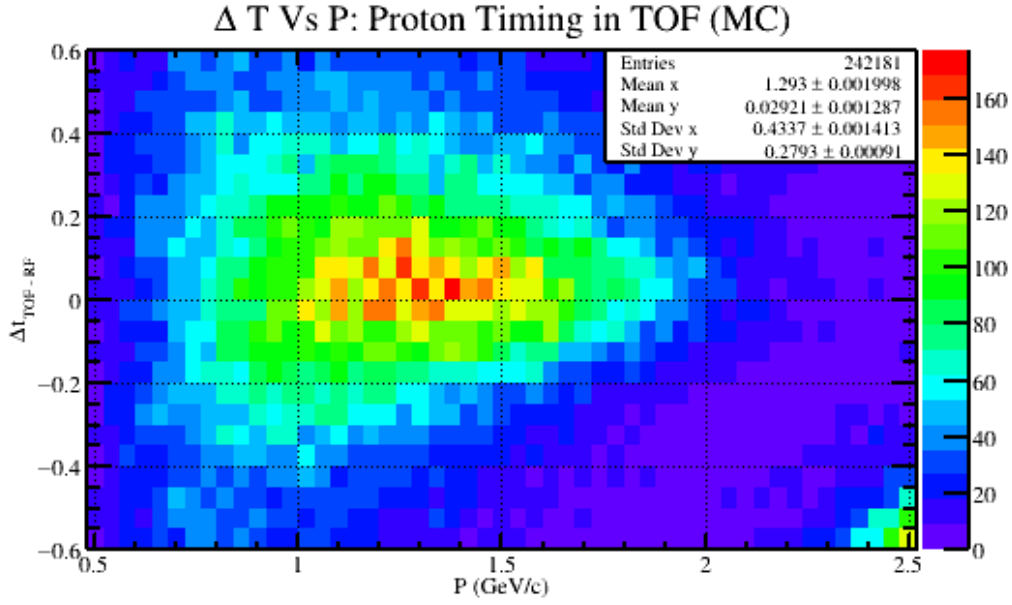
Figure 9: A timing plot for generated protons after reconstruction. The horizontal axis is the reconstructed momentum of the proton and the vertical axis is the timing difference between the TOF and RF. The enhancement of statistics in the lower right portion of the plot comes from miss identified kaons that were also included in the Monte Carlo.
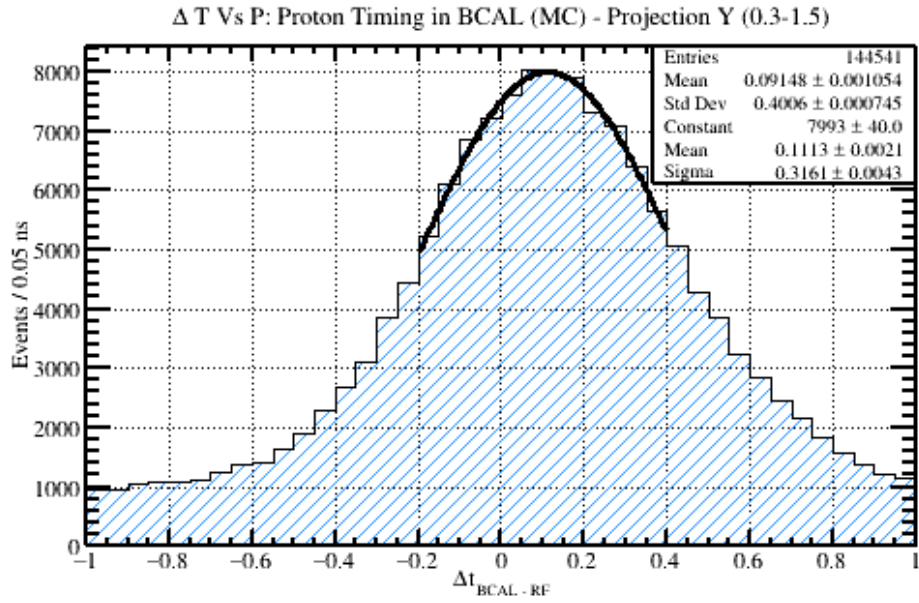
Figure 10: A projection of the statistics from Figure [9] onto the vertical (timing) axis between the momentum range of 0.5-1.8 GeV/C. This projection range was chosen so that the distortion from the lower kaon band was minimized. A gaussian fit was performed and is included in the figure where the mean and width of the distribution are given in the legend.
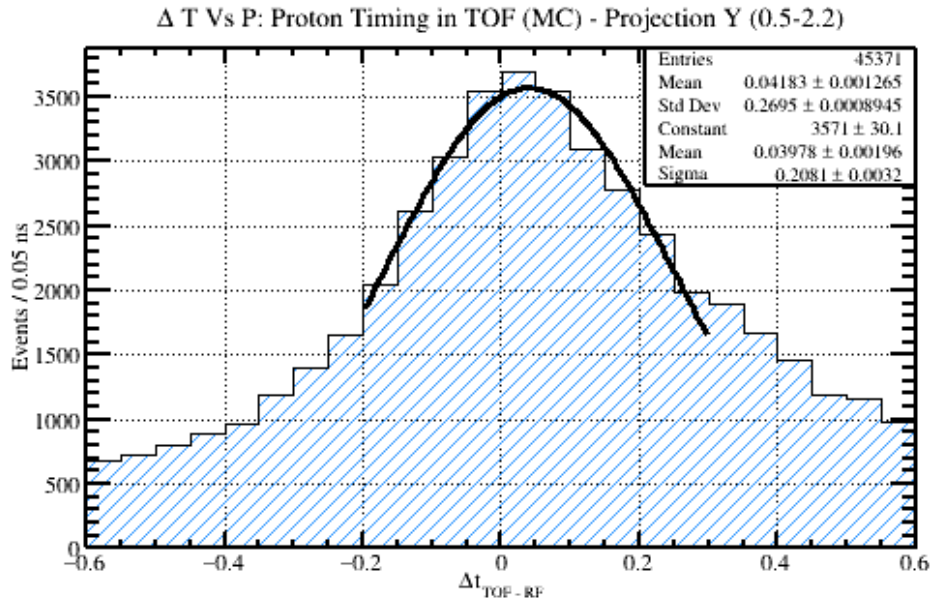
14

1.3.2 K^+

There are two cuts that were used to identify the final state K^+. The first cut is to enforce the reconstructed vertex position of the K^+ track came from inside the target chamber. This cut is used to eliminate any parent state of the K^+ that may have a longer lifetime and therefore a detached vertex. The cut used is identical to those found and described in the Target section. The other cut that is used to identify the K^+ is the timing from the BCAL, FCAL, and TOF. An example of what these distributions look like as a function of momentum is given in Figure [11]. Since the data has a lot of pion and proton background in these plots, it is difficult to determine what the proper timing cuts should be for all of the sub detectors. Due to this, a Monte Carlo sample of $\gamma p \to pX; X \to \phi\eta; \phi \to K^+K^-; \eta \to \gamma\gamma$ was generated and then reconstructed. This greatly reduces the background that is present in the timing plots and therefore can be used to estimate a proper timing cut for the K^+ and the sub detectors used to measure its time. Examples of these distributions and their associated projections onto the timing axis is given in Figure [12] through Figure [17]. It should be noted that in many of the Monte Carlo plots, there appears to be an additional band from a particle with less mass. This is a consequence of using the *hdgeant* simulator, and the fact that it will decay particles while in flight. Therefore, the band inside the Monte Carlo plots arises from the weak decay of a kaon to a muon and a neutrino. A summary of all of the timing cuts used for the K^+ as well as all other final state particles is given in Table [1].
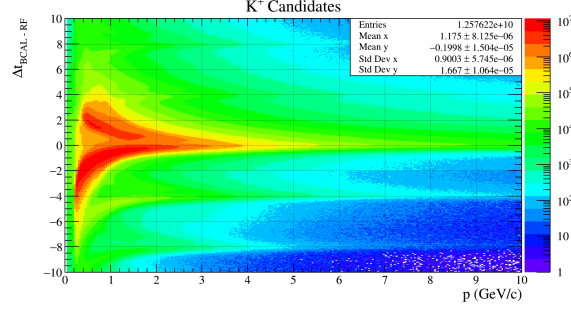
(a) Δ T Vs P for K^+ candidates that have the Barrel Calorimeter as the timing detector.
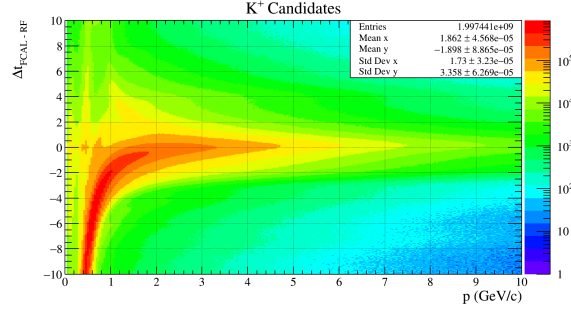
(b) Δ T Vs P for K^+ candidates that have the Forward Calorimeter as the timing detector.
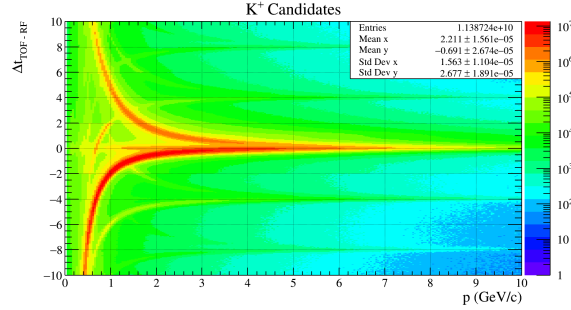
(c) Δ T Vs P for K^+ candidates that have the Time of Flight as the timing detector.

Figure 11: Timing plots for K^+ candidates at GlueX. K^+ are identified by selecting the horizontal band centered about $\Delta T = 0$. The curved line deviating below the horizontal K^+ line comes from miss identified π^+ tracks, and the curved line deviating above the horizontal K^+ line comes from miss identified proton tracks. The additional curved lines above and below $\Delta T = 0$ come from π^+ and proton tracks that are associated with the wrong RF bunch.

Figure 12: A timing plot for generated K^+ after reconstruction. The horizontal axis is the reconstructed momentum of the K^+ and the vertical axis is the timing difference between the BCAL and RF. It should be noted that the statistics in this sampling are smaller than other plots. This is due to the fact that the kinematics of the generated channel prefer to have the kaons moving in the forwards direction; and therefore provide few timing hits in the BCAL. Additionally, the extra statistics present in the upper left portion of the graph are due to protons included in this Monte Carlo sample.
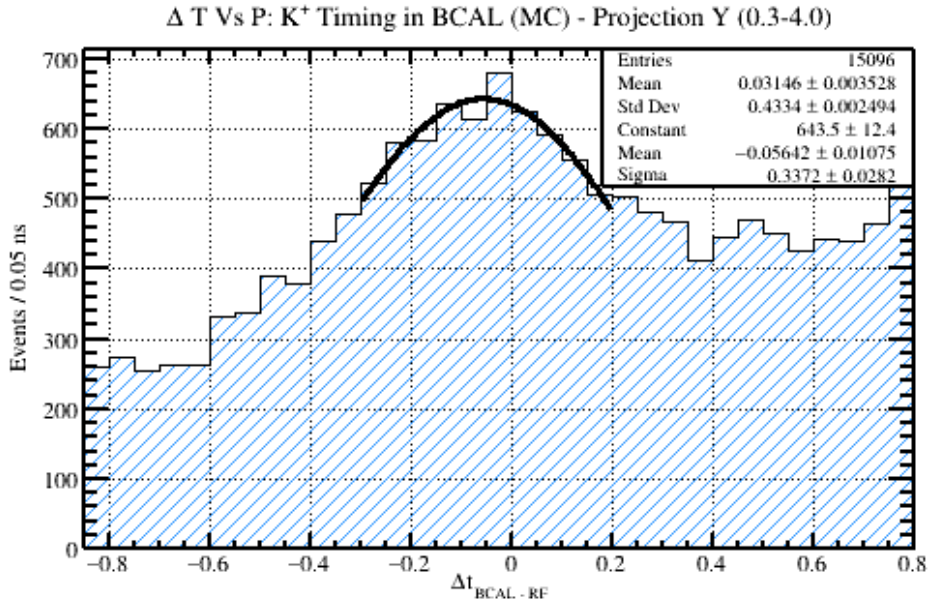
Figure 13: A projection of the statistics from Figure [12] onto the vertical (timing) axis between the momentum range of 0.3-4.0 GeV/C. A Gaussian fit was performed and is included in the figure where the mean and width of the distribution are given in the legend. The distortion of statistics towards the higher timing differences is due to protons included in this Monte Carlo study.
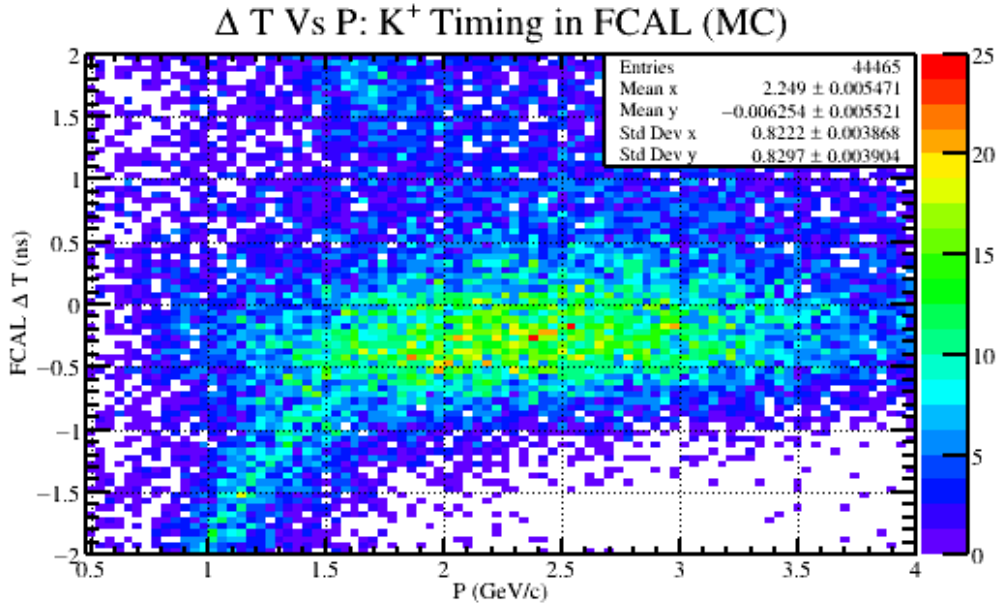
Figure 14: A timing plot for generated K^+ after reconstruction. The horizontal axis is the reconstructed momentum of the K^+ and the vertical axis is the timing difference between the FCAL and RF. The curved band that appears below the K^+ band around 1.5 GeV/c and lower comes from μ^+. Although muons were not explicitly generated, the computer program hdgeant (derived from geant) allows for some fraction of kaons to decay weakly while in flight; resulting in a observed muons.
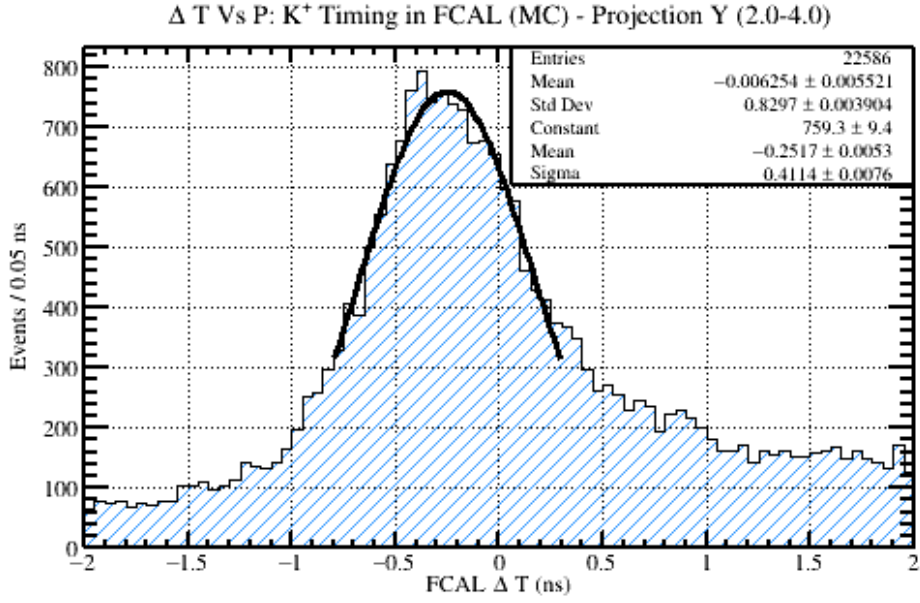
Figure 15: A projection of the statistics from Figure [14] onto the vertical (timing) axis between the momentum range of 2.0-4.0 GeV/C. This projection range was chosen so that the distortion from the lower muon band and upper proton band was minimized. A Gaussian fit was performed and is included in the figure where the mean and width of the distribution are given in the legend.
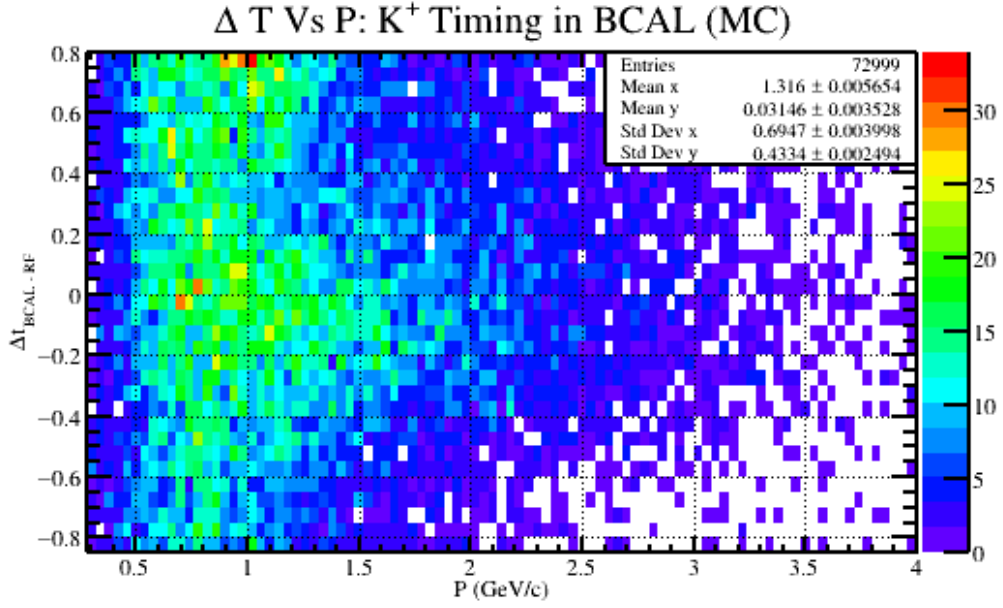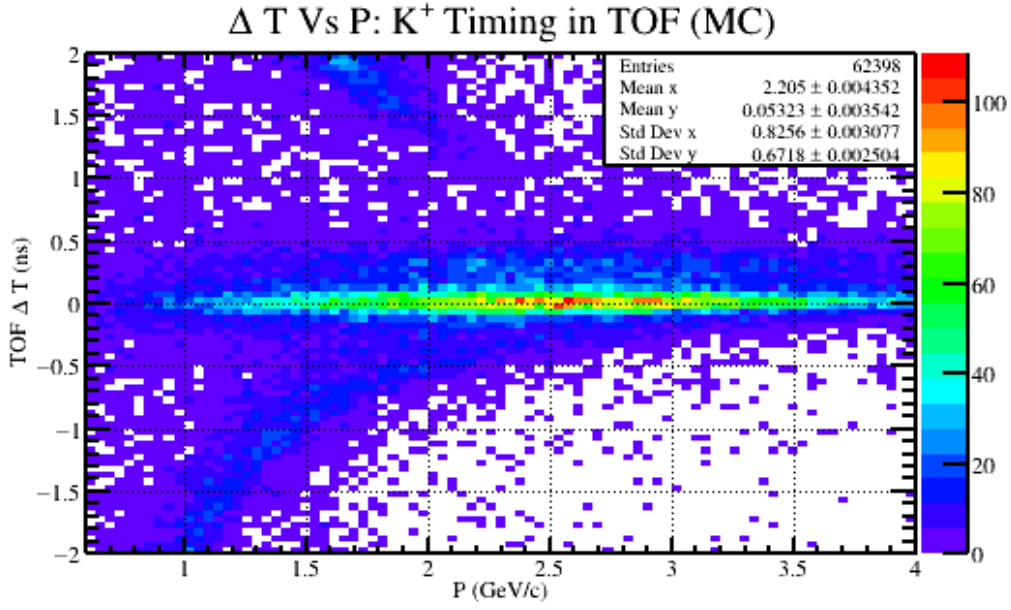
Figure 16: A timing plot for generated K^+ after reconstruction. The horizontal axis is the reconstructed momentum of the K^+ and the vertical axis is the timing difference between the TOF and RF. The curved band that appears below the K^+ band around 2.5 GeV/c and lower comes from μ^+; and the band near the top of the plot comes from protons. Although muons were not explicitly generated, the computer program hdgeant (derived from geant) allows for some fraction of kaons to decay weakly while in flight; resulting in an observed muon.
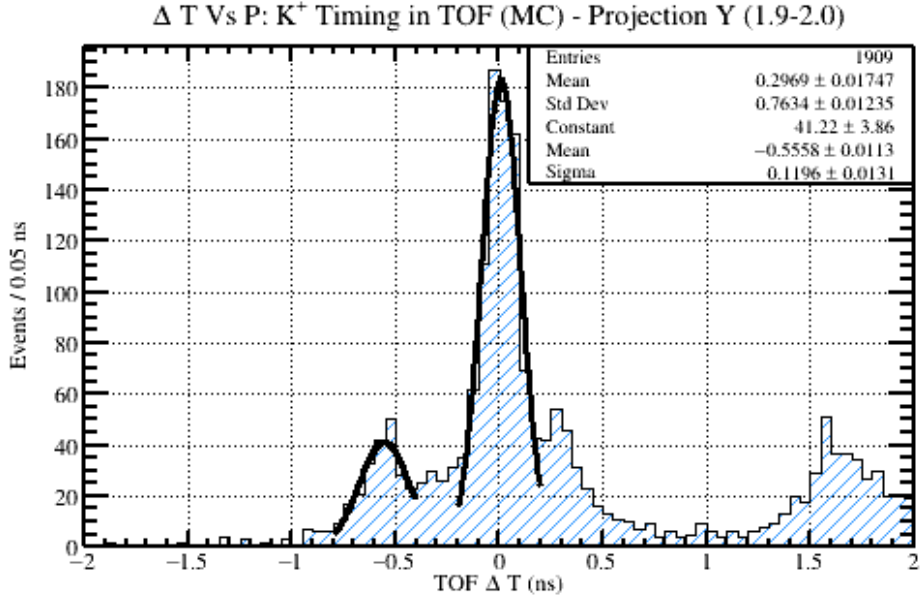
Figure 17: A projection of the statistics from Figure [16] onto the vertical (timing) axis between the momentum range of 1.9-2.0 GeV/C. This projection range is one out of many that were studied from Figure [16]. The purpose of this study is to determine the amount of muon contamination in the kaon band as a function of momentum. The results of this study are provided in Figure [18]. Lastly, two Gaussian fits were performed on this data. The mean and width of these Gaussian fits are recorded in Figure [18] for each momentum range.
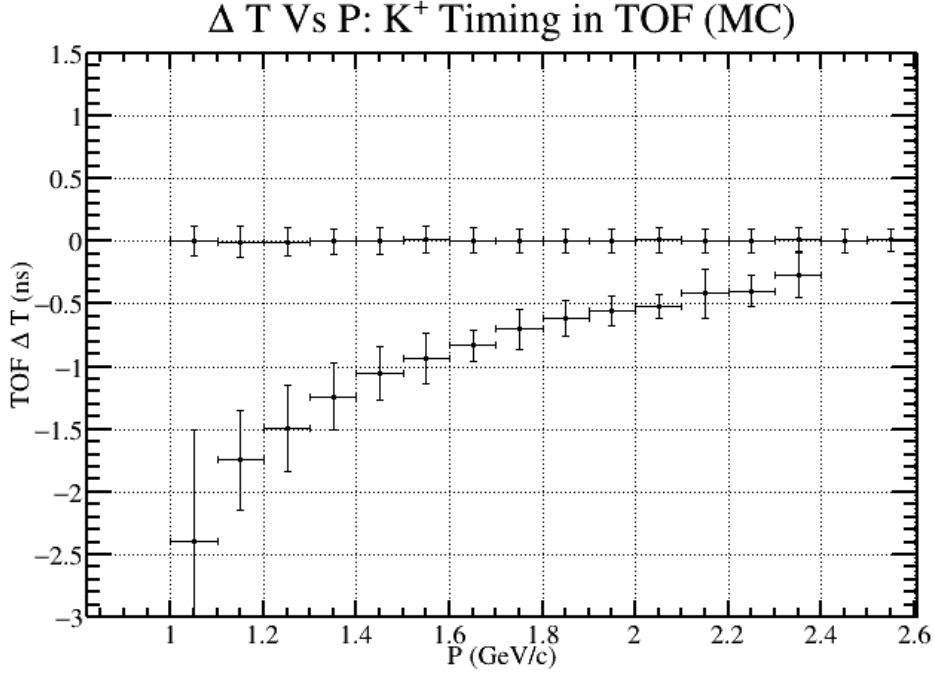
Figure 18: The image above is the result of the timing study performed on Figure [16]. Using that figure, a number of projection histograms were fit using different momentum ranges. An example of one of these fits is given in Figure [17]. The data points close to 0 ΔT correspond to the Gaussian fits performed on the kaon signal, and the data points that approach that band from the bottom correspond to the Gaussian fits performed on the muon signal. The horizontal position of each point is in the middle of the projection range, and the vertical position of each point was assigned based on the mean value of the Gaussian fit for each particle. The horizontal error bars are the size of the projection range, which is always 0.1 GeV/c. The vertical error bars are determined by the width of the Gaussian fits. The average of the widths of the kaon peaks is 0.1ns which is the value used to determine the timing cut in Table 1.

1.3.3 K^-

Just like its antiparticle, the K^- has two identifying cuts; the vertex and timing cuts. The vertex cut is used to eliminate any parent state of the K^- that may have a longer lifetime and therefore a detached vertex. The cut used is identical to those found and described in the Target section. The timing cuts for the K^- are for the BCAL, FCAL, and TOF sub detectors. Since

23

the timing distributions from data (Figure [19]) have too much background in them, a Monte Carlo sample of $\gamma p \to pX; X \to \phi\eta; \phi \to K^+K^-; \eta \to \gamma\gamma$ was generated and then reconstructed. This greatly reduces the background that is present in the timing plots and therefore can be used to estimate a proper timing cut for the K^- and the sub detectors used to measure its time. Examples of these distributions and their associated projections onto the timing axis is given in Figure [20] through Figure [25]. It should be noted that in many of the Monte Carlo plots, there appears to be an additional band from a particle with less mass. This is a consequence of using the *hdgeant* simulator, and the fact that it will decay particles from while in flight. Therefore, the band inside the Monte Carlo plots arises from the weak decay of a kaon to a muon and a neutrino. A summary of all of the timing cuts used for the K^- as well as all other final state particles is given in Table [1].
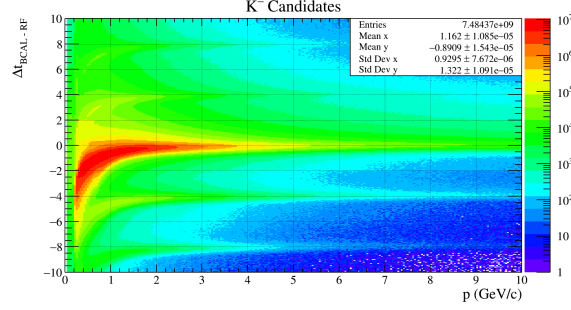
(a) Δ T Vs P for K^- candidates that have the Barrel Calorimeter as the timing detector.
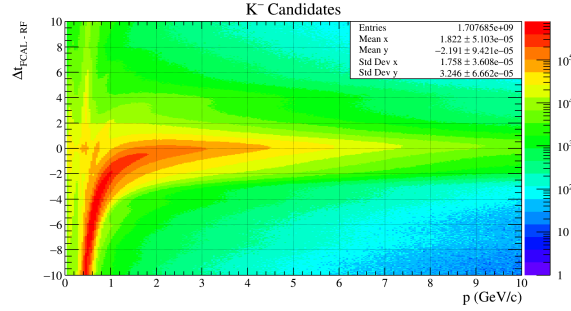
(b) Δ T Vs P for K^- candidates that have the Forward Calorimeter as the timing detector.
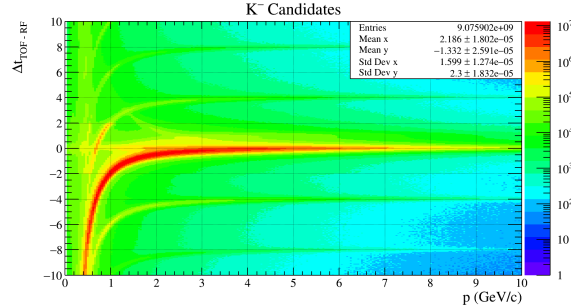
(c) Δ T Vs P for K^- candidates that have the Time of Flight as the timing detector.

Figure 19: Timing plots for K^- candidates at GlueX. K^- are identified by selecting the horizontal band centered about $\Delta T = 0$. The curved line deviating below the horizontal K^- line comes from miss identified π^- tracks. The additional curved lines above and below $\Delta T = 0$ come from π^- tracks that are associated with the wrong RF bunch.
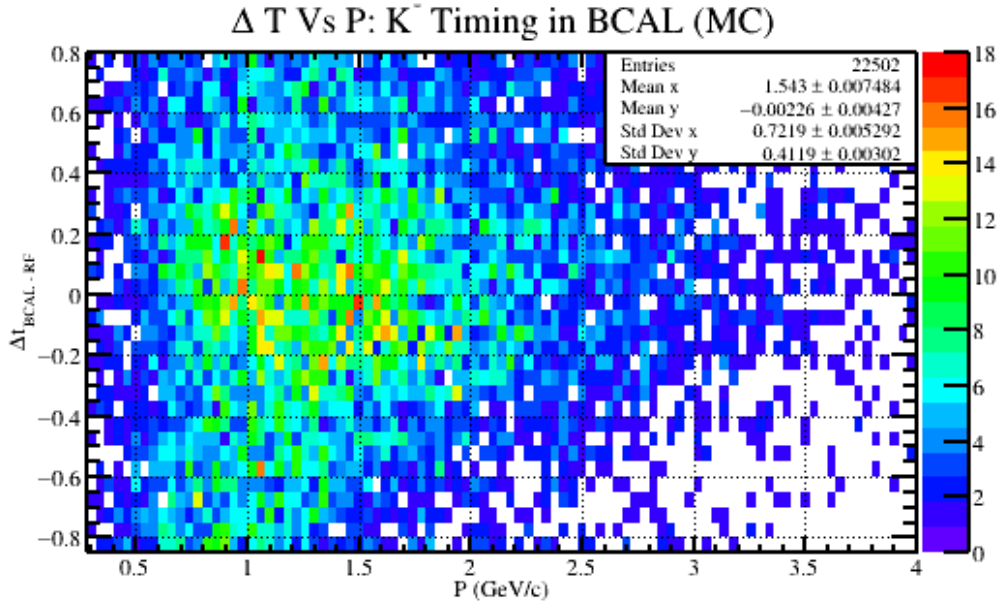
Figure 20: A timing plot for generated K^- after reconstruction. The horizontal axis is the reconstructed momentum of the K^- and the vertical axis is the timing difference between the BCAL and RF. It should be noted that the statistics in this sampling are smaller than other plots. This is due to the fact that the kinematics of the generated channel prefer to have the kaons moving in the forwards direction; and therefore provide few timing hits in the BCAL. Additionally, the extra statistics present in the lower left portion of the graph are due to muons. Although muons were not explicitly generated, the computer program hdgeant (derived from geant) allows for some fraction of kaons to decay weakly while in flight; resulting in observed muons.
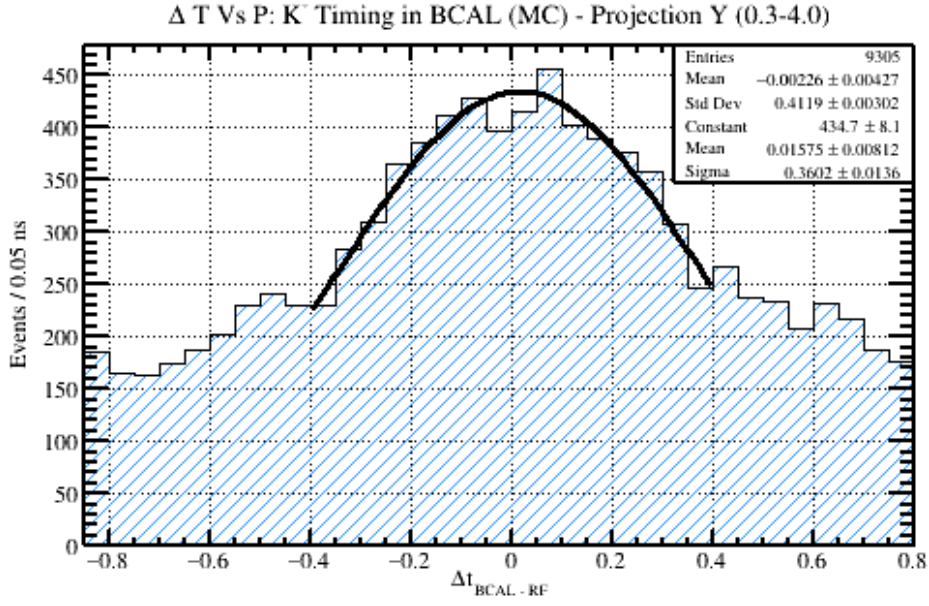
Figure 21: A projection of the statistics from Figure [20] onto the vertical (timing) axis between the momentum range of 0.3-4.0 GeV/C. A Gaussian fit was performed and is included in the figure where the mean and width of the distribution are given in the legend.
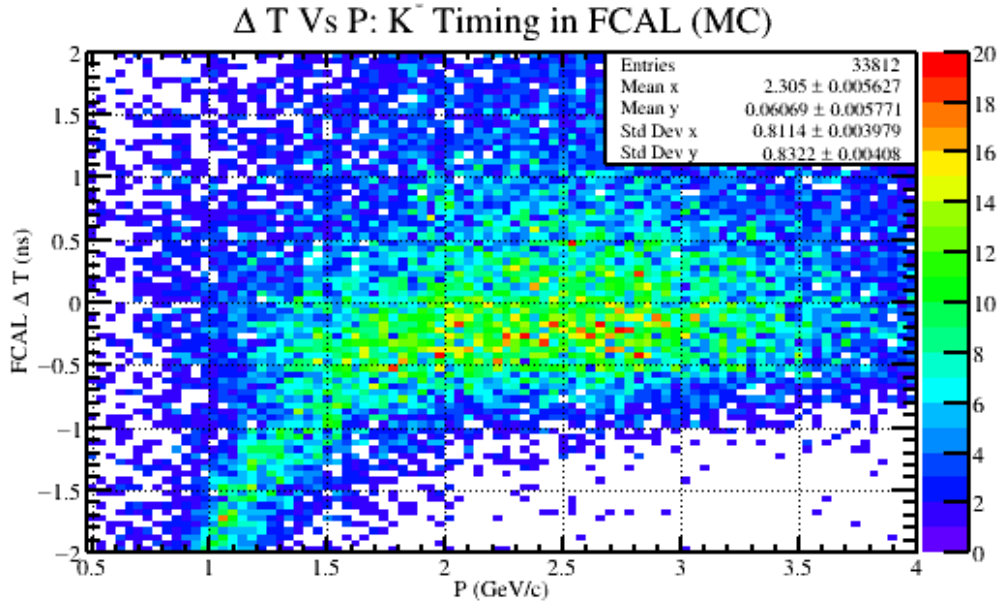
Figure 22: A timing plot for generated K^- after reconstruction. The horizontal axis is the reconstructed momentum of the K^- and the vertical axis is the timing difference between the FCAL and RF. The curved band that appears below the K^- band around 1.5 GeV/c and lower comes from μ^-. Although muons were not explicitly generated, the computer program hdgeant (derived from geant) allows for some fraction of kaons to decay weakly while in flight; resulting in an observed muon.

28
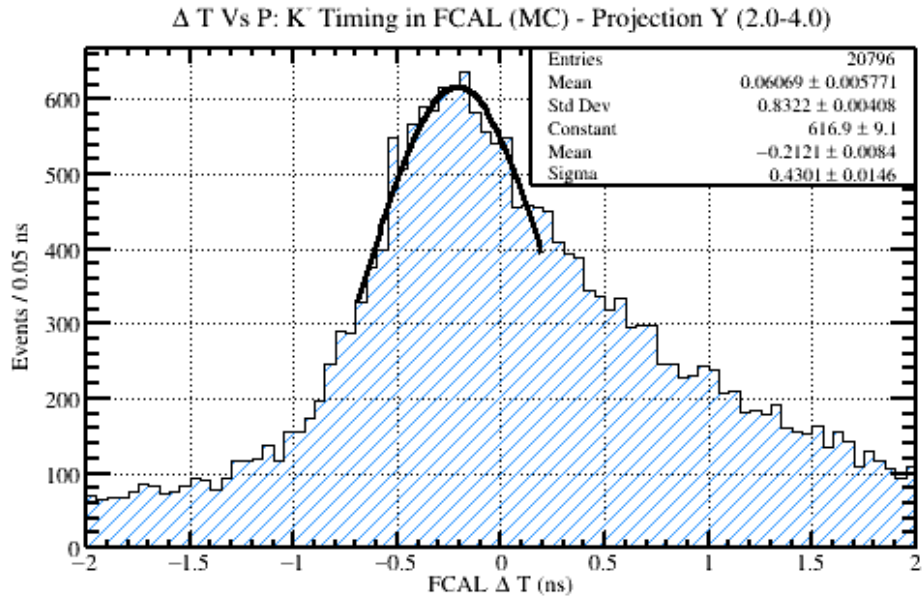
Figure 23: A projection of the statistics from Figure [22] onto the vertical (timing) axis between the momentum range of 2.0-4.0 GeV/C. This projection range was chosen so that the distortion from the lower muon band was minimized. A Gaussian fit was performed and is included in the figure where the mean and width of the distribution are given in the legend.

Figure 24: A timing plot for generated K^- after reconstruction. The horizontal axis is the reconstructed momentum of the K^- and the vertical axis is the timing difference between the TOF and RF. The curved band that appears below the K^- band around 2.5 GeV/c and lower comes from μ^-. Although muons were not explicitly generated, the computer program hdgeant (derived from geant) allows for some fraction of kaons to decay weakly while in flight; resulting in an observed muon.
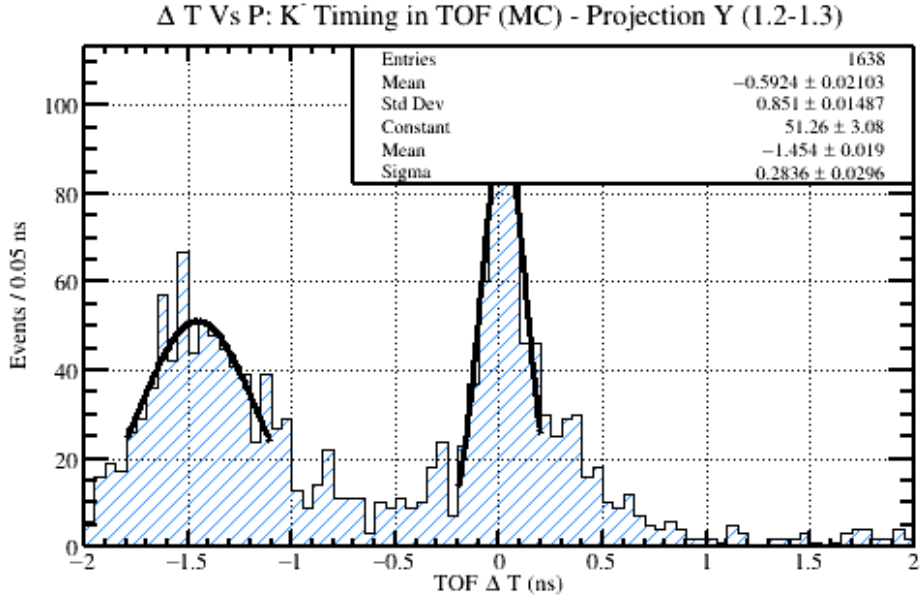
Figure 25: A projection of the statistics from Figure [24] onto the vertical (timing) axis between thprotone momentum range of 1.2-1.3 GeV/C. This projection range is one out of many that were studied from Figure [24]. The purpose of this study is to determine the amount of muon contamination in the kaon band as a function of momentum. The results of this study are provided in Figure [26]. Lastly, two Gaussian fits were performed on this data. The mean and width of these Gaussian fits are recorded in Figure [26] for each momentum range.

Figure 26: The image above is the result of the timing study performed on Figure [24]. Using that figure, a number of projection histograms were fit using different momentum ranges. An example of one of these fits is given in Figure [25]. The data points close to 0 ΔT correspond to the Gaussian fits performed on the kaon signal, and the data points that approach that band from the bottom correspond to the Gaussian fits performed on the muon signal. The horizontal position of each point is in the middle of the projection range, and the vertical position of each point was assigned based on the mean value of the Gaussian fit for each particle. The horizontal error bars are the size of the projection range, which is always 0.1 GeV/c. The vertical error bars are determined by the width of the Gaussian fits. The average of the widths of the kaon peaks is 0.1ns which is the value used to determine the timing cut in Table 1.

1.3.4 γ

Unlike the other final state particles with charge, the final state photons only have two timing cuts and no vertex cuts. There are no vertex cuts because the photon has no net charge and can therefore not leave a charged track inside the detector to reconstruct. Without a charged track to reconstruct, it is impossible for the reconstruction to backtrack where the particle originated from. In addition, there is also no timing cut for the TOF. This is due to the fact that the time of flight can only interact with charged particles, and therefore cannot interact with photons. The timing cuts for the γ only come from the BCAL, FCAL. Since the timing distributions from data (Figure [27]) have too much neutron background in them, a Monte Carlo sample of $\gamma p \rightarrow pX; X \rightarrow \phi\eta; \phi \rightarrow K^+K^-; \eta \rightarrow \gamma\gamma$ was generated and then reconstructed. This greatly reduces the background that is present in the timing plots and therefore can be used to estimate a proper timing cut for the γ and the sub detectors used to measure its time. Examples of these distributions and their associated projections onto the timing axis is given in Figure [28] through Figure [31]. A summary of all of the timing cuts used for the photon as well as all other final state particles is given in Table [1].

BCAL γ Candidates

Entries	4.680355e+10
Mean x	0.4268 ± 1.808e−06
Mean y	0.6197 ± 8.862e−06
Std Dev x	0.3822 ± 1.278e−06
Std Dev y	1.874 ± 6.267e−06

(a) Δ T Vs Shower Energy for γ candidates that have the Barrel Calorimeter as the timing detector.

FCAL γ

Entries	2.269053e+10
Mean x	0.7107 ± 6.346e−06
Mean y	0.5189 ± 1.432e−05
Std Dev x	0.8543 ± 4.488e−06
Std Dev y	1.928 ± 1.013e−05

(b) Δ T Vs Shower Energy for γ candidates that have the Forward Calorimeter as the timing detector.

Figure 27: Timing plots for γ candidates at GlueX. γ are identified by selecting the horizontal band centered about $\Delta T = 0$. Large enhancement in statistics at low momentum and out of time with the γ line comes from slow moving and poorly times neutrons. The additional horizontal lines above and below $\Delta T = 0$ come from γ showers that are associated with the wrong RF bunch.
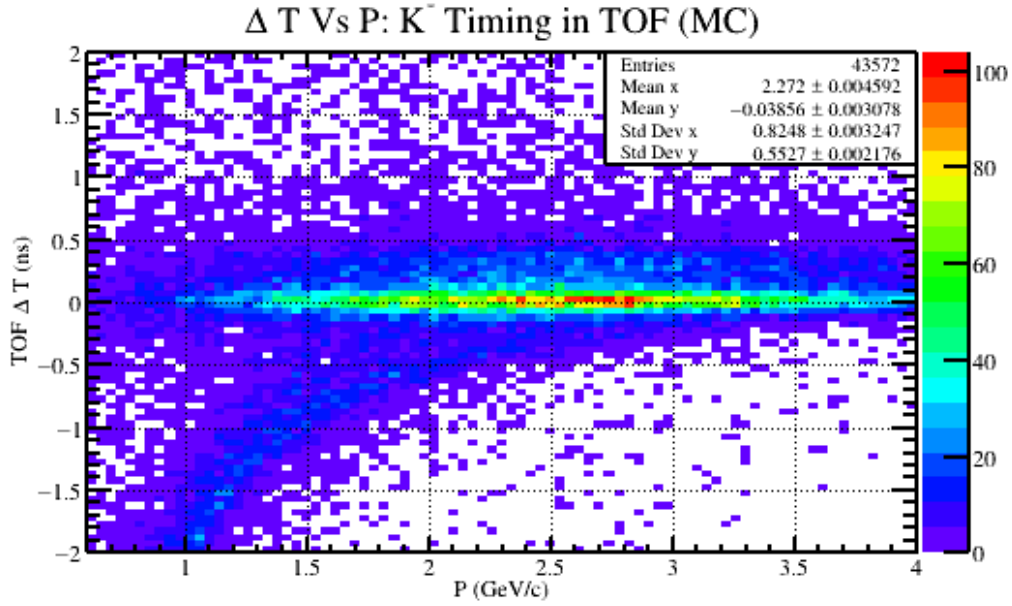
34
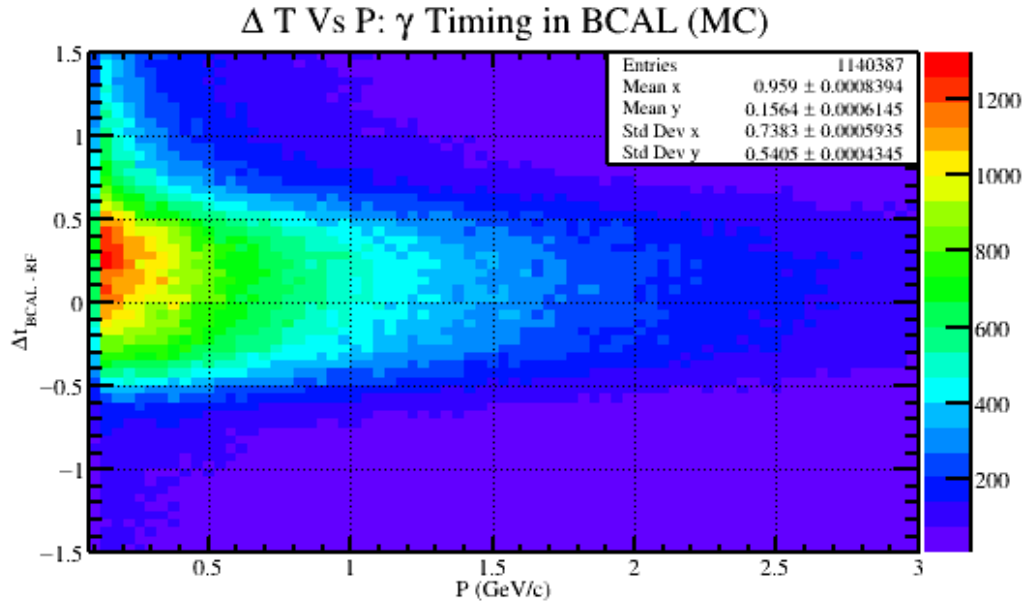
Figure 28: A timing plot for generated γ after reconstruction. The horizontal axis is the reconstructed momentum of the γ and the vertical axis is the timing difference between the BCAL and RF.
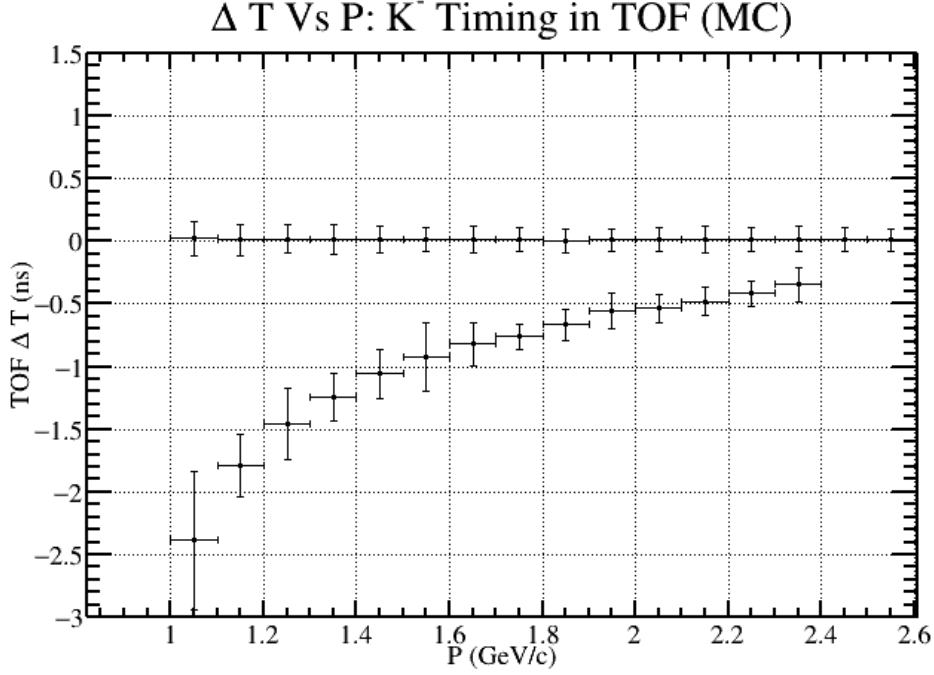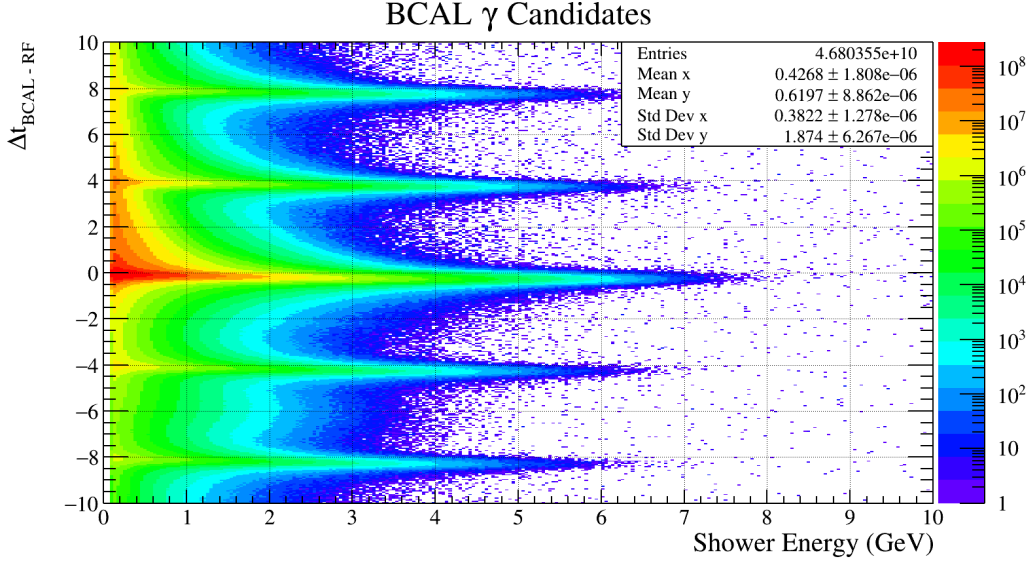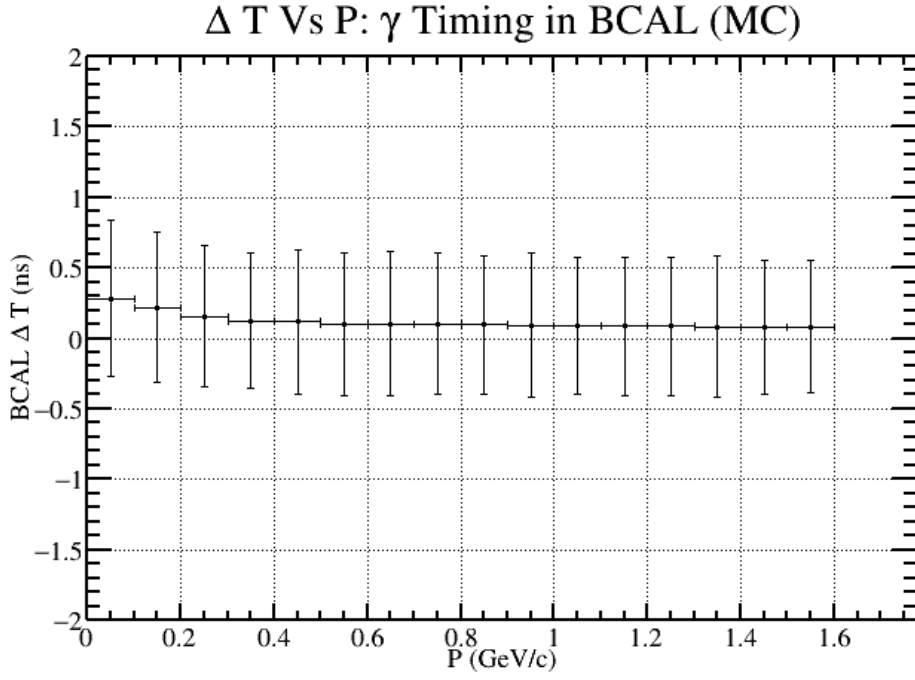
Figure 29: The image above is the result of the timing study performed on Figure [28]. Using that figure, a number of projection histograms were fit using different momentum ranges. The horizontal position of each point is in the middle of the projection range, and the vertical position of each point was assigned based on the mean value of the Gaussian fit. The horizontal error bars are the size of the projection range, which is always 0.1 GeV/c. The vertical error bars are determined by the width of the Gaussian fit. The average of the widths of the photon peaks is $\sim 0.5ns$ which is the value used to determine the timing cut in Table [1].

36
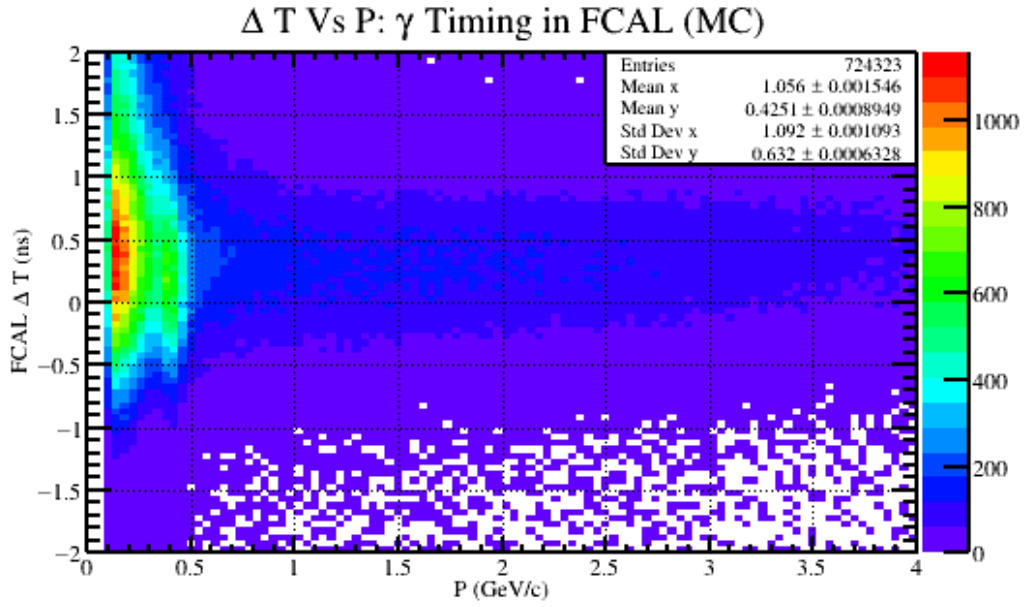
Figure 30: A timing plot for generated γ after reconstruction. The horizontal axis is the reconstructed momentum of the γ and the vertical axis is the timing difference between the FCAL and RF.
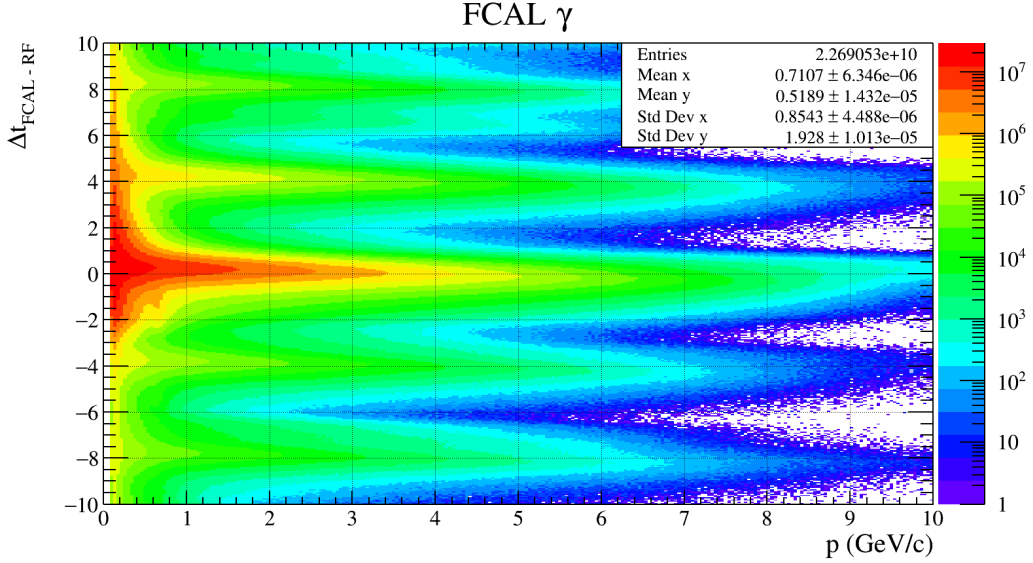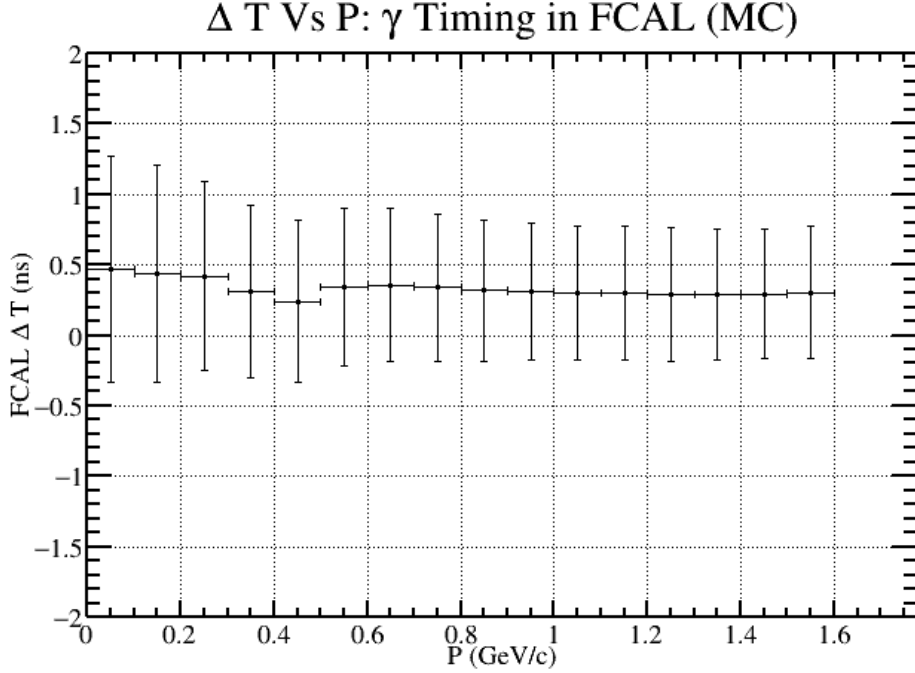
Figure 31: The image above is the result of the timing study performed on Figure [30]. Using that figure, a number of projection histograms were fit using different momentum ranges. The horizontal position of each point is in the middle of the projection range, and the vertical position of each point was assigned based on the mean value of the Gaussian fit. The horizontal error bars are the size of the projection range, which is always 0.1 GeV/c. The vertical error bars are determined by the width of the Gaussian fit. The average of the widths of the photon peaks is $\sim 0.55ns$ which is the value used to determine the timing cut in Table [1].

2   Additional Cuts for $\gamma p \rightarrow pK^+K^-\gamma\gamma$

2.0.1   Kaon Timing Selection Cut

After the particle identification cuts had been made on the data, it was found that there was still a large amount of background in the K^+K^- invariant mass plot. This background was in all likelihood due to misidentified pions that were mistaken for kaons. This can happen because of the timing and momentum resolutions inherent in any particle physics experiment. Furthermore, as can be seen in many of the timing plots provided, pions and kaon are in fact indistinguishable at high momentum. An example of what

the K^+K^- invariant mass histogram looks like after all particle identification cuts can be seen in Figure 32.
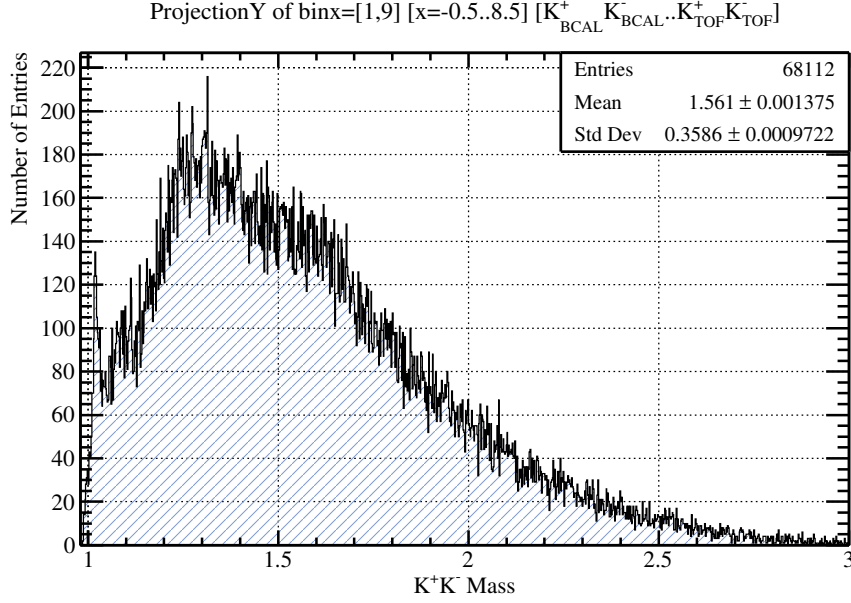
Figure 32: A histogram showing the K^+K^- invariant mass after particle identification cuts. The figure clearly shows a large amount of background at masses higher than the ϕ. This is due to the misidentification of pions for kaons.

Due to this background, a study was performed over 5 percent of the data in order to understand both where it may be coming from. The answer to this question was found by splitting up the K^+K^- invariant mass into different sub detectors which are responsible for the timing of the kaons. At GlueX, the three sub detectors which are responsible for providing timing and particle identification for charged particles are the Barrel Calorimeter, the Forward Calorimeter, and the Time of Flight. Since both the K^+ and the K^- can interact with any three of these sub detectors, there are nine total possible timing combinations that need to be considered. In order to properly understand these combinations, a two dimensional color histogram was provided to show how the K^+K^- invariant mass changes as a function of sub detector timing for the kaons (Figure 33).
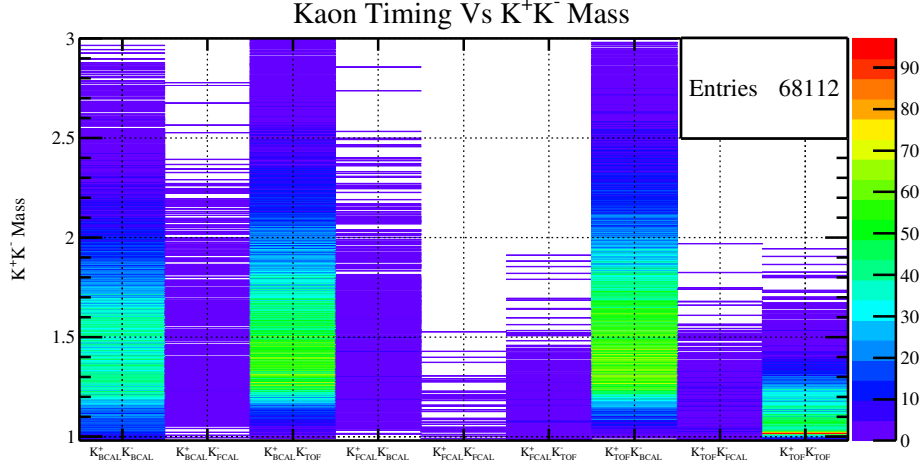
Figure 33: A two dimensional color histogram of the K^+K^- invariant mass versus the timing detectors for the kaons.

There are three important observations that can be made from Figure 33. One observation is that there is an overwhelming amount of background which comes from the Barrel Calorimeter timing for both K^+ and K^-. The second observation is that the Forwards Calorimeter has little to no statistics what so ever. This is due to the fact that the GlueX reconstruction algorithm prefers timing from sub detectors that have the best timing resolution. Since the Time of Flight and the Forwards Calorimeter are in the same geometric direction, this means that they tend to share a lot of the same charged tracks. Since the timing resolution of the Time of Flight detector is better than the Forward Calorimeter, the majority of forward going charged tracks have timing from the Time of Flight. The last observation of Figure 33 is that merely all of the events which appear to have a ϕ meson reconstructed in them only exist in the last bin which is the TOF/TOF timing bin. More specifically, it appears that most of the relevant $\phi\eta$ events will only have kaon timing that came from the Time of Flight detector. Therefore, all other timing sub detectors for the kaons can be thrown out. To further emphasize this point, projections of all nine bins contained within Figure 33 have been provided (Figures 34,35,36). These figures clearly show K^+K^- invariant mass spectra which contain all background and no sign of a ϕ meson; with the exception of the TOF/TOF projection.

40
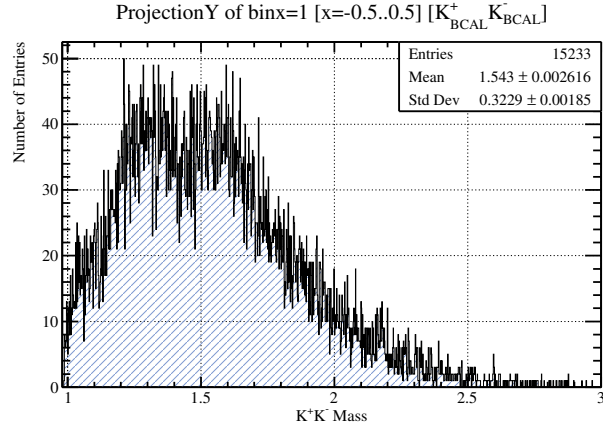
(a) Projection of $K^+_{BCAL}K^-_{BCAL}$ bin from Figure 33.
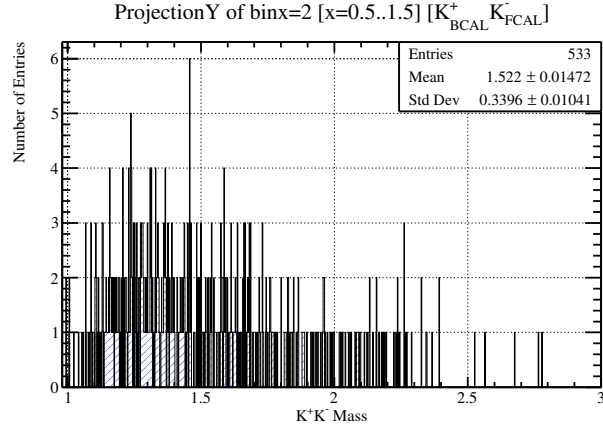
(b) Projection of $K^+_{BCAL}K^-_{FCAL}$ bin from Figure 33.
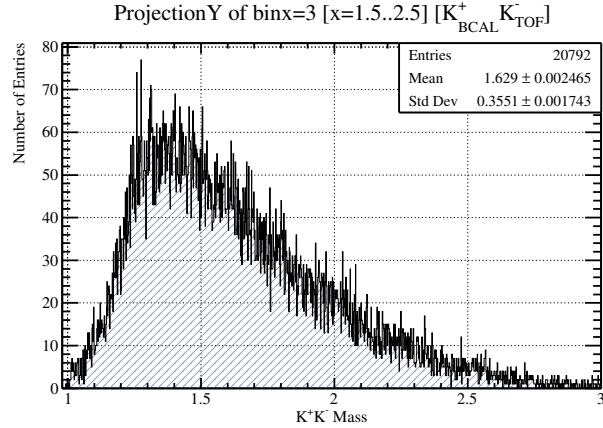
(c) Projection of $K^+_{BCAL}K^-_{TOF}$ bin from Figure 33.

Figure 34: Projections of $K^+_{BCAL}K^-_X$ bins from Figure 33.
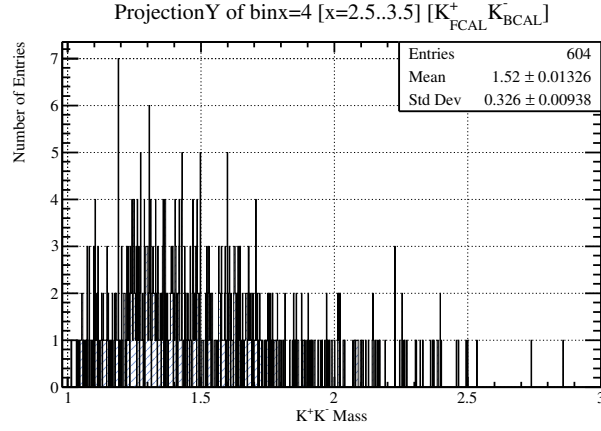
(a) Projection of $K^+_{FCAL}K^-_{BCAL}$ bin from Figure 33.
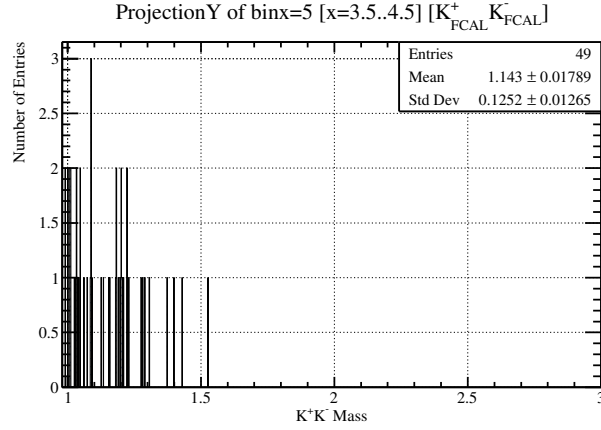
(b) Projection of $K^+_{FCAL}K^-_{FCAL}$ bin from Figure 33.
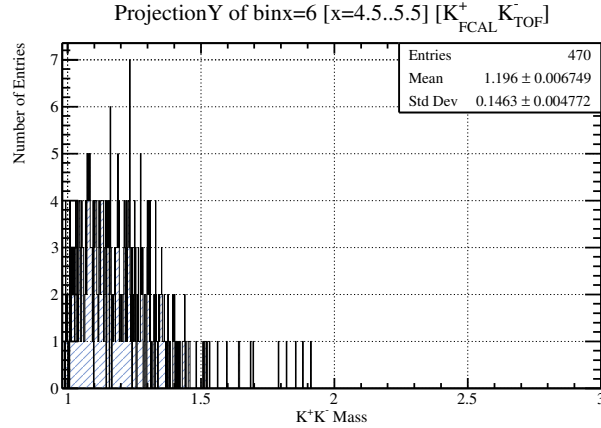
(c) Projection of $K^+_{FCAL}K^-_{TOF}$ bin from Figure 33.

Figure 35: Projections of $K^+_{FCAL}K^-_X$ bins from Figure 33.

42
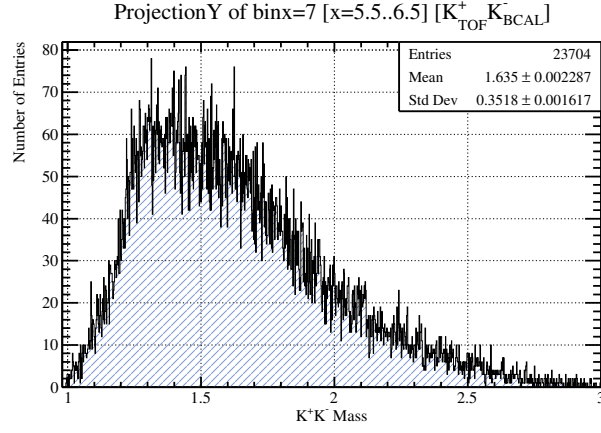
(a) Projection of $K^+_{TOF}K^-_{BCAL}$ bin from Figure 33.
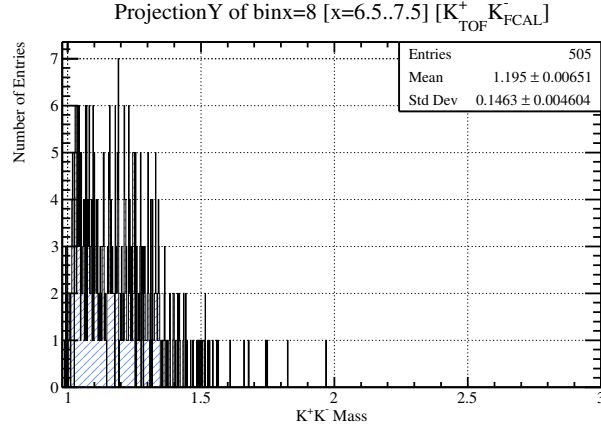
(b) Projection of $K^+_{TOF}K^-_{FCAL}$ bin from Figure 33.
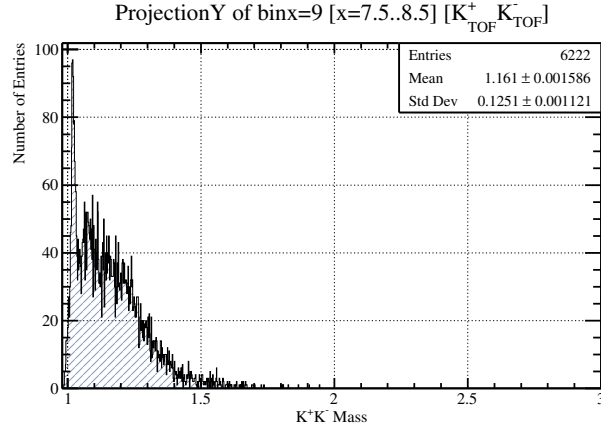
(c) Projection of $K^+_{TOF}K^-_{TOF}$ bin from Figure 33.

Figure 36: Projections of $K^+_{TOF}K^-_X$ bins from Figure 33.

43

2.0.2 Strangeness Conservation Cut

One key aspect to performing a $\phi\eta$ analysis is to both identify the ϕ and the η mesons while also reducing the amount of background in each of their invariant mass spectra. One of the issues with the K^+K^- invariant mass spectra is the fact that it contains misidentified pions. This background causes a peak in the K^+K^- invariant mass around $1.2 GeV/c^2$. This peak is a manifestation of a ρ^0 which can decay to a $\pi^+\pi^-$ final state. An example of this background is illustrated nicely in Figure 37.
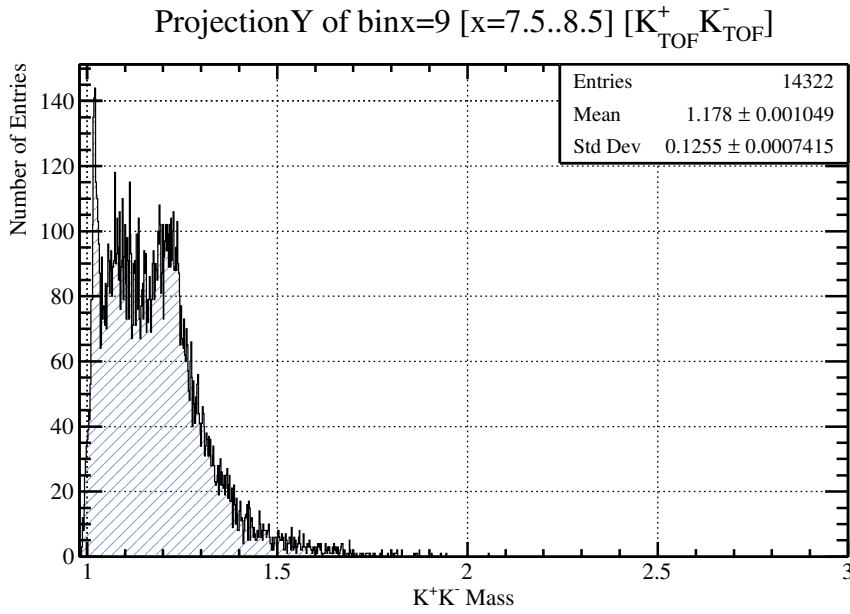
Figure 37: An example K^+K^- invariant mass histogram without a strangeness conservation cut. A clear rho peak can be seen around roughly $1.2 GeV/c^2$. The histogram which has a reduced pion background can be seen in Figure 36c.

One important aspect of QCD and the quark model is the conservation of quark flavor in hadronic decays, or decays which involve the interaction of the strong nuclear force. Conservation of quark flavor states that the initial number flavored quarks minus the initial number of corresponding anti-quarks of the same flavor, must be conserved. An example of this can be any strong interaction which is being studied with the GlueX spectrometer. The experiment has an initial state photon which has no net quark content, plus a proton which has two up quarks and one down quark. Since the GlueX experiment is designed to study hadronic interactions, the final state must have a net quark flavor of two up quarks and one down quark. Considering

the $\gamma p \to p\phi\eta$ interaction, it is clear that this requirement is met. The initial and final state proton are identical in quark flavor, and the ϕ and η mesons have no net quark flavor to them. Moreover, since the K^+K^- decay of the ϕ meson is being considered, the overall strangeness of this decay needs to be conserved as well. To state this more explicitly, the K^+ meson consists of a $u\bar{s}$ composite state, while the the K^- meson consists of a $s\bar{u}$ composite state. Since each kaon carries either a strange or anti-strange quark, it is only necessary to observe one kaon well. The method of only identifying one kaon well is called strangeness conservation.

Strangeness conservation is used to both preserve good $\phi\eta$ statistics, while also reducing the amount of background under the ϕ peak (Figure 37). Since the Time of Flight detector is the only timing detector used for the kaons in this analysis, it is only necessary to consider the particle identification from that sub detector. In order to understand how strangeness conservation is implemented in this analysis, Figure 38 is provided. Contained within this figure is the timing versus momentum plot for the K^+, identical to Figure 18. Also contained within this diagram is a red line which represents the cut that will be used to separate particles with 'good strangeness' as opposed to particles that 'do not have good strangeness'. This red line is not drawn randomly, or by eye, but is rather derived from simple equations of physics.

The flight time it takes for any relativistic particle to travel a distance δX at a velocity V in the lab frame, can be expressed using Equation 1.

$$t = \frac{\delta X}{V} = \frac{\delta X}{\beta c} \tag{1}$$

Furthermore, it is well known from Special Relativity that $\beta = E/P$. Using the relativistic equation for invariant mass, we can rewrite Equation 1 as Equation 2.

$$t = \frac{\delta X}{c} \frac{\sqrt{m_i^2 + P^2}}{P} \tag{2}$$

Since Equation 2 is true for any particle, we can then use it to describe the timing difference between pions and kaons in the lab frame, as measured by the Time of Flight. This final equation will take the form of Equation 3.

$$\delta t = \frac{\delta X}{c} \frac{\sqrt{m_\pi^2 + P^2} - \sqrt{m_K^2 + P^2}}{P} \tag{3}$$

The parameters δX, c, m_π, and m_K are known for Equation 3 since one is the speed of light, two are well known invariant masses of sub atomic particles, and the other is the distance from the center of the target chamber to the wall of the time of flight. Although charged particles will bend while

traveling inside a static magnetic field, this effect is minimal due to the high forward momentum of the kaons in this reaction. Therefore, the only two variables left over are δt and P which serve as the vertical and horizontal axis variables, respectively.

One last modification of Equation 3 is needed in order to take the form seen in Figure 38. If the equation is left the way that it is, the red line would simply bisect the pion curve, and would therefore not work well as a background cut. Therefore, Equation 3 is shifted up by $0.2ns$. This parameter was chosen based on the timing study that was performed on the Monte Carlo and is therefore a 2σ timing shift. It should be noted that since the K^+ and K^- mesons are anti-particles, as well as the π^+ and π^-, the same equation can be used to separate background for both kaons.
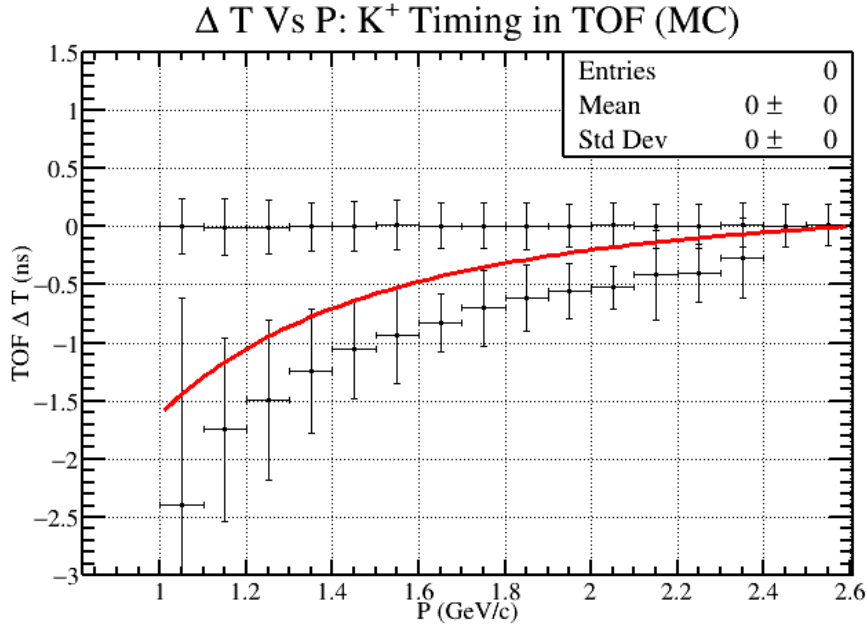
Figure 38: A histogram which provides the strangeness conservation cut used for kaons that are detected by the Time of Flight detector. This is identical to Figure 18, except that it includes a red line which represents Equation 3, with a timing shift of $0.2ns$.

Given Equation 3 and Figure 38, strangeness conservation can now be addressed. In order to enforce strangeness conservation, it is imperative to identify one 'good kaon'. Good kaons will have three primarily characteristics to them. One characteristic is that the timing will be centered around $\delta t = 0$, the second is that its timing will only come from the Time of Flight, and

46

third is that it will be to the left or above of the red line given in Figure 38. Any particle that is to the right or below the red line is not guaranteed to be a kaon, and is therefore 'unknown'. Strangeness conservation allows us to preserve more statistics because all that is needed to justify the observation of a final state which includes a K^+K^- is one 'good kaon'. Therefore, any combination that the has either a K^+ or a K^- with the characteristics mentioned above will be accepted. The only combinations that will be rejected ones which both kaon candidates fail the characteristics mentioned above. To emphasize the importance and effectiveness of this cut, one should see what the K^+K^- invariant mass looks like without strangeness conservation (Figure 37), and then compare it to the K^+K^- invariant mass with strangeness conservation (Figure 36c).

2.0.3 Fiducial Photon Cut and Two Photon Cut

Before performing this Monte Carlo study, it was well known that there was a lot of photon background seen in the data. After studying the data for quite some time, it was found that a two photon cut would destroy most of the background associated with photons and would also result in an observed η resonance in a $\gamma\gamma$ invariant mass plot. At the time, it was unknown why the cut appeared to throw out a lot of photon background while simultaneously appearing to enhance signal. After carefully studying accepted Monte Carlo, background generated Monte Carlo (`bggen`), and data, it was found that much of this background is attributed to secondary photons. A secondary photon should be thought of as a photon that did not originate from any photoproduction reaction, nor from any expected decay of parent states. Therefore, a secondary photon can be thought of as a photon that arose from an interaction within the GlueX spectrometer from a final state particle. An example of a secondary photon that would be present in $\gamma p \rightarrow p\phi\eta$ data can be explained by means of high momentum and forward going kaons (Figures [54][55]). Since it is very likely that most of the kaons in this channel will interact with either the Time of Flight detector or the Forward Calorimeter, it is expected that these particle will deposit a lot of energy in this region of the spectrometer. These high momentum particles will cause a signal in one or both of these detectors and will also cause a 'splash' effect near the signal region. This splash effect can cause some of the blocks in the Forward Calorimeter to absorb the extra energy and therefore become reconstructed photons in the data. The additional reconstructed photons will therefore cause the number of photons reconstructed in an event to be fictitiously higher than what was actually present within the detector. To first order, this perhaps explains why doing a two photon cut on data

47

will both greatly reduce background and enhance a signal. However, many important questions will still remain about this cut. How much signal do we lose by simply performing a two photon cut? Furthermore, is there a better way to cut out the background and preserve as many signal events as possible? This subsection will show that this effect does in fact manifest itself in both Monte Carlo and data; and will perform an analysis on Monte Carlo and data to show the best way of reducing secondary photons.

The first evidence that suggests the existence of secondary photons in $\gamma p \to p\phi\eta; \phi \to K^+K^-; \eta \to \gamma\gamma$ accepted Monte Carlo can be seen by simply plotting the invariant mass of a reconstructed $\gamma\gamma$ pair (Figure [39]). The data which went into this plot was created by throwing $\gamma p \to p\phi\eta; \phi \to K^+K^-; \eta \to \gamma\gamma$ into the GlueX detector and then simulating its behavior with `hdgeant` and `mcsmear`. The invariant mass spectrum in Figure [39] shows a clear peak from the generated η meson on top of a background that spans to low mass. If this sample initially only threw two photons exactly equal to the η meson invariant mass, then why are there so many low mass photon combinations that appear to be in the shape of background? To answer this question, we can separate our reconstructed Monte Carlo particles into two categories: particles that were generated and particles that were not generated. In doing so, we can see where this background comes from and also how to possibly reduce it.
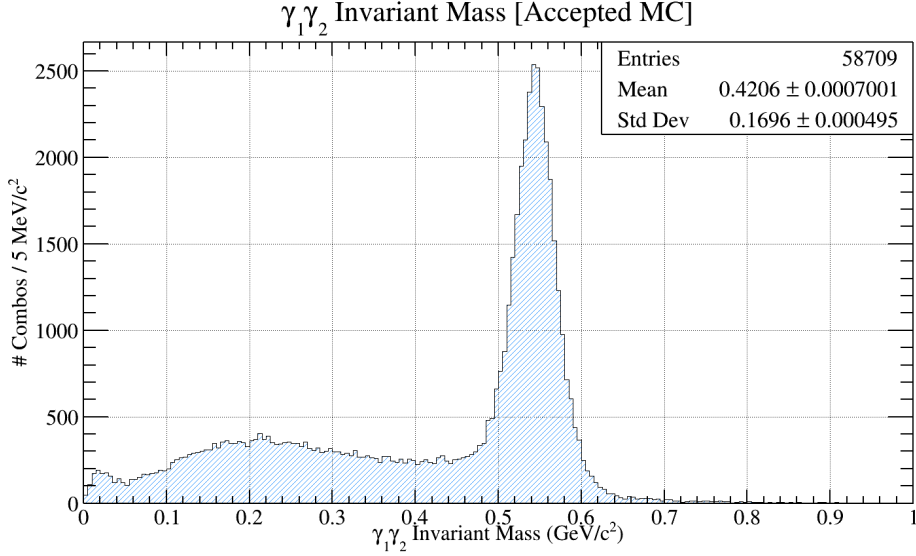
Figure 39: Invariant mass of the reconstructed $\gamma_1\gamma_2$ pair from accepted Monte Carlo. This Monte Carlo data originally came from a $\gamma p \rightarrow p\phi\eta; \phi \rightarrow K^+K^-; \eta \rightarrow \gamma\gamma$ generated topology. An interesting feature of this invariant mass spectra is that it shows a clear η peak, but also contains a background as well. The source of this background is thoroughly studied in subsection 2.0.3.

We will first describe the background seen in Figure [39] by displaying P Vs θ and ϕ Vs θ plots for the thrown photons and the secondary photons in Figure [40]. The most important feature to take away from these plots is the tendency for secondary photons to be at a shallow angle relative to the beam direction (below 12°) while also having a low three momentum magnitude (below 500 MeV/c). Simply knowing the distribution of these photons gives us some insight into where they came from. Since neutral photons can only be detected by either the Forward Calorimeter or the Barrel Calorimeter and most of these photons appear in the forward direction, it is clear that FCAL showers are causing these photons to appear.

49
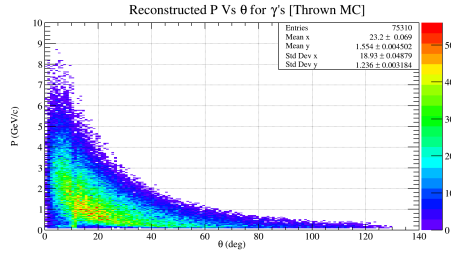
(a) P Vs θ distribution for thrown Monte Carlo photons.
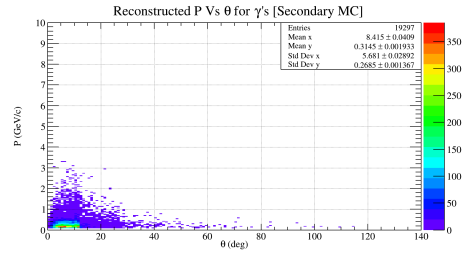
(b) P Vs θ distribution for secondary Monte Carlo photons.
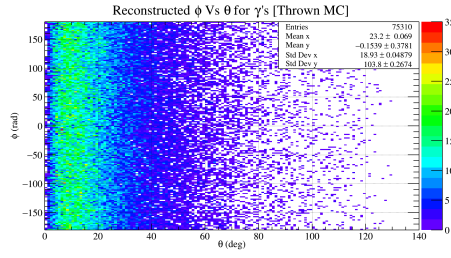
(c) ϕ Vs θ distribution for thrown Monte Carlo photons.
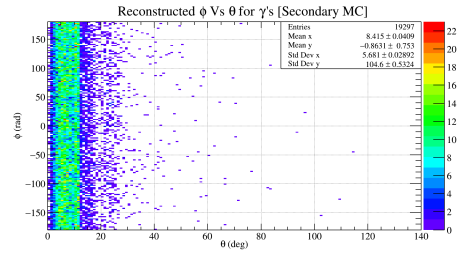
(d) ϕ Vs θ distribution for secondary Monte Carlo photons.

Figure 40: P Vs θ and ϕ Vs θ distributions for thrown (left column) and secondary (right column) photons inside accepted Monte Carlo data.

50

The reconstructed invariant mass for a given $\gamma\gamma$ combination within an event as a function of the number of photons reconstructed within an event can also be shown. By using our Monte Carlo samples, we can also separate these plots into thrown and secondary photons, identical to what we did in Figure [40]. The reconstructed invariant mass of two photons versus the number of reconstructed photons in an event is given in Figure [41]. There are two important observations that should be taken away from the two sub figures. In Figure 41a a clear η resonance can be seen which spans a large number of reconstructed photons per event. What this sub figure tells us right away is that performing a two photon cut on the data is not good for signal events. In fact, after fitting a Gaussian function to the η peaks between 3 and 10 reconstructed photons, it was found that $\sim$8,000 combinations would be lost out of a total of $\sim$30,000; resulting in a 26 percent loss of events. The second important feature seen in Figure 41b is the fact that most of the secondary photons exist in events which reconstruct more than two photons per event. Therefore, it is imperative to cut secondary photons while also preserving the event photons that exist in events which yield a large number of reconstructed photons.
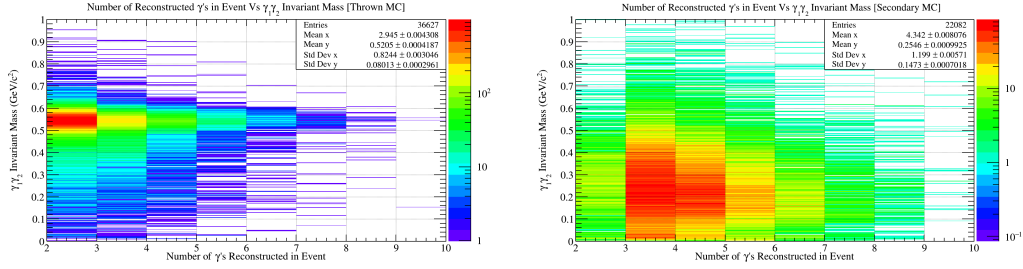
(a) Number of photons reconstructed in an event versus $\gamma_1\gamma_2$ Invariant Mass for thrown photons.

(b) Number of photons reconstructed in an event versus $\gamma_1\gamma_2$ Invariant Mass for secondary photons.

Figure 41: Comparing how the invariant mass for a given $\gamma\gamma$ pair changes depending on the number of reconstructed photons in an event and whether or not the photons were thrown or secondary photons.

There are a number of ways to cut the secondary photons seen in accepted Monte Carlo. The first and most obvious way would be to cut photons that are both below 12° θ and lower than 500 MeV/c in three momentum magnitude. However, since this analysis will eventually include a cut on Kinematic Fit confidence level, the effect of this cut on secondary photons will be studied first. This portion of the study will now include three sets of data: accepted Monte Carlo, background generated Monte Carlo `bggen`, and data. The fist plot that will be shown is the Kinematic Fit confidence level versus the reconstructed $\gamma_1\gamma_2$ invariant mass for all three data sets (Figure [42]). In each plot one can easily see an η peak at higher confidence level along side background which is typically at much lower confidence level. Using the accepted Monte Carlo from Figure [42a] it was determined that a preliminary Kinematic Fit confidence level cut would be placed at the value $1x10^{-6}$.
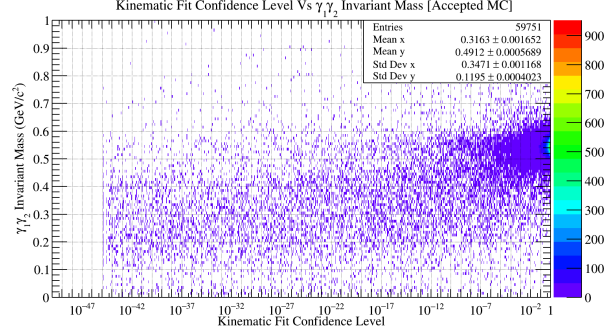
(a) Kinematic Fit confidence level (scaled logarithmically) versus $\gamma_1\gamma_2$ Invariant Mass for accepted Monte Carlo.
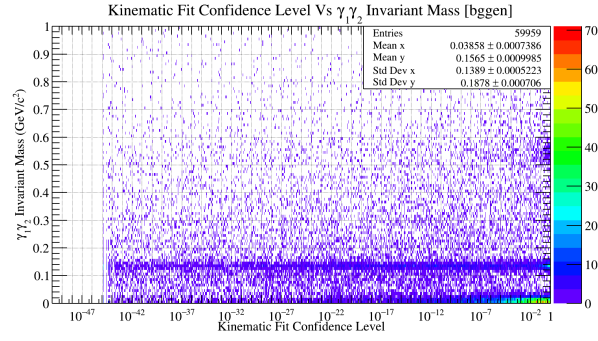
(b) Kinematic Fit confidence level (scaled logarithmically) versus $\gamma_1\gamma_2$ Invariant Mass for background generated Monte Carlo.
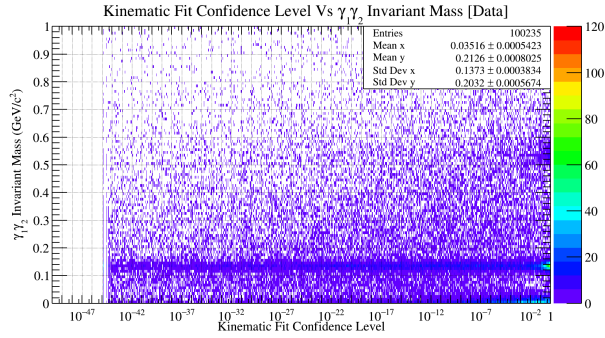
(c) Kinematic Fit confidence level (scaled logarithmically) versus $\gamma_1\gamma_2$ Invariant Mass for data.

Figure 42: Kinematic Fit confidence level (scaled logarithmically) versus $\gamma_1\gamma_2$ Invariant Mass for accepted Monte Carlo, background generated Monte Carlo, and data.

After performing a confidence level cut of $1x10^{-6}$ it is clear that much of the secondary photons are destroyed. One way of seeing the effect of this cut is by looking at the number of reconstructed photons in an event versus the $\gamma_1 \gamma_2$ invariant mass distributions (Figure [43]). Comparing Figure [43a] with Figure [41a], one can easily see that the Kinematic Fit confidence level cut moved many of the η's from high photon reconstruction number per event to low photon reconstruction number per event. This migration of events is due to the fact that the Kinematic Fitter is cutting many secondary photons out of events and therefore decreasing the number of photons reconstructed per event. Furthermore, comparing Figure [43b] with Figure [41b], one can simply look at the density of events within the two dimensional histogram to realize that an overwhelming amount of secondaries has been cut, roughly 94 percent.
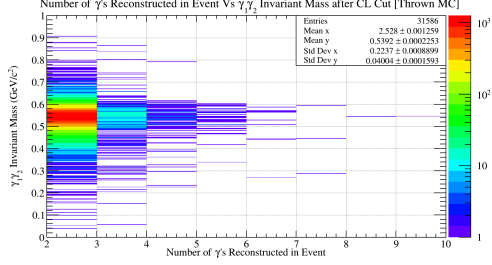
(a) Number of photons reconstructed in an event versus $\gamma_1\gamma_2$ Invariant Mass for thrown photons after a Kinematic Fit confidence level cut of $1x10^{-6}$.
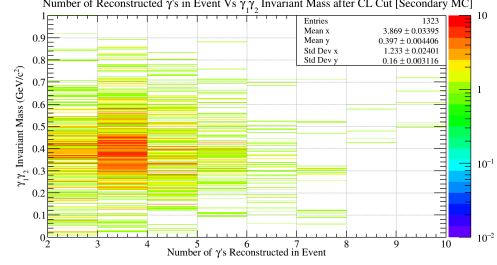
(b) Number of photons reconstructed in an event versus $\gamma_1\gamma_2$ Invariant Mass for secondary photons after a Kinematic Fit confidence level cut of $1x10^{-6}$.
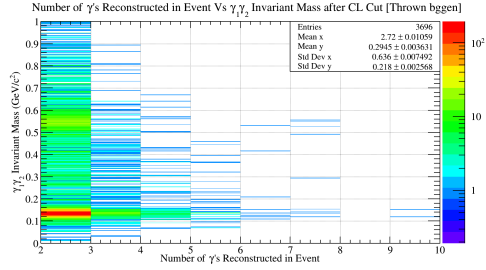
(c) Number of photons reconstructed in an event versus $\gamma_1\gamma_2$ Invariant Mass for thrown photons from `bggen` data after a Kinematic Fit confidence level cut of $1x10^{-6}$.
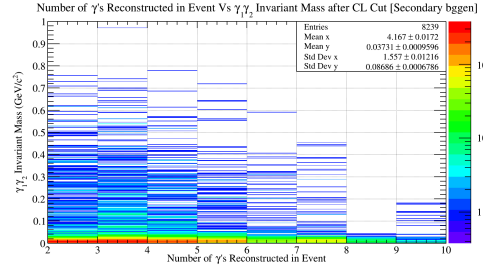
(d) Number of photons reconstructed in an event versus $\gamma_1\gamma_2$ Invariant Mass for secondary photons from `bggen` data after a Kinematic Fit confidence level cut of $1x10^{-6}$.
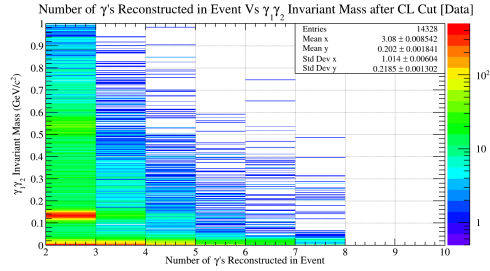
(e) Number of photons reconstructed in an event versus $\gamma_1\gamma_2$ Invariant Mass for data after a Kinematic Fit confidence level cut of $1x10^{-6}$.

Figure 43: Number of photons reconstructed in an event versus $\gamma_1\gamma_2$ Invariant Mass for accepted Monte Carlo, `bggen`, and data after a Kinematic Fit confidence level cut of $1x10^{-6}$.

Seeing that there is still a non negligible amount of secondary photons left in accepted Monte Carlo and `bggen`, the next cut that will be applied to all of the data is a P Vs θ cut, where $P < 500 MeV/c$ and $\theta < 12$ °. After enforcing these cuts on all photons, the distribution of number of photons reconstructed in an event versus $\gamma_1\gamma_2$ Invariant Mass is shown once again in Figure [44]. It is easy to see that most, if not all of the η signal has migrated to the two photon bin and simultaneously much of the secondary background has been reduced in all data sets. Due to this, a two photon cut is now necessary to do in order to reduce some of the left over background at higher number of reconstructed photons per event.
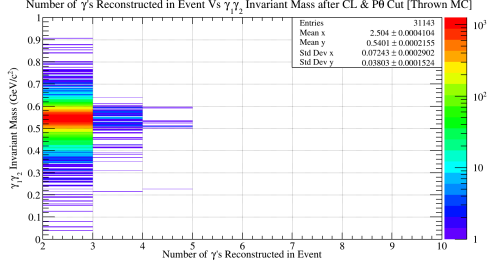
(a) Number of photons reconstructed in an event versus $\gamma_1\gamma_2$ Invariant Mass for thrown photons after a confidence level cut of $1x10^{-6}$ and a P Vs θ cut.
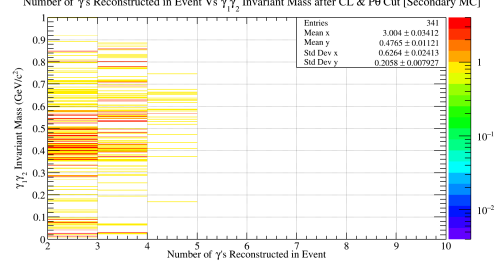
(b) Number of photons reconstructed in an event versus $\gamma_1\gamma_2$ Invariant Mass for secondary photons after a confidence level cut of $1x10^{-6}$ and a P Vs θ cut.
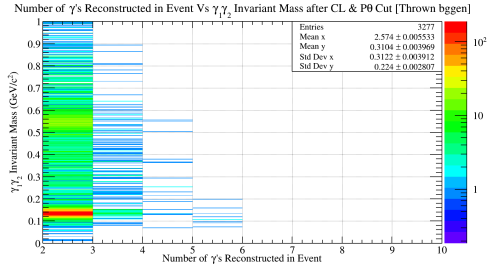
(c) Number of photons reconstructed in an event versus $\gamma_1\gamma_2$ Invariant Mass for thrown photons from `bggen` data after a confidence level cut of $1x10^{-6}$ and a P Vs θ cut.
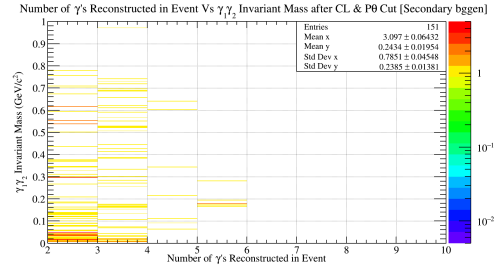
(d) Number of photons reconstructed in an event versus $\gamma_1\gamma_2$ Invariant Mass for secondary photons from `bggen` data after a confidence level cut of $1x10^{-6}$ and a P Vs θ cut.
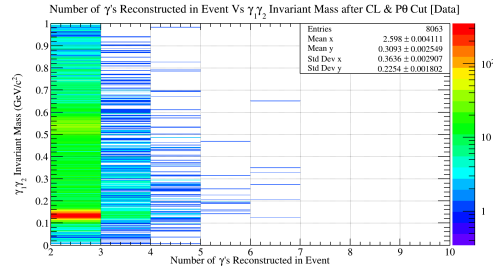
(e) Number of photons reconstructed in an event versus $\gamma_1\gamma_2$ Invariant Mass for data after a confidence level cut of $1x10^{-6}$ and a P Vs θ cut.

Figure 44: Number of photons reconstructed in an event versus $\gamma_1\gamma_2$ Invariant Mass for accepted Monte Carlo, `bggen`, and data after a confidence level cut of $1x10^{-6}$ and a P Vs θ cut.

57

In this section it was shown that it is necessary to perform a P Vs θ cut of $P < 500 MeV/c$ and $\theta < 12$ °and a two photon cut. After completing this sequence of cuts, it was found that 94 percent of background data was cut, while preserving 93 percent of signal data.

2.1 Exclusivity

The last cuts that need to take place in order to observe $\gamma p \rightarrow p\phi\eta$ are two; one which reduces the number of photons from the beam, and the other which cuts on the missing mass squared of the system. After all cuts had been made, it was found that there were still residual combinations from events which came directly from the beam photons and not the final state particles. After the proper beam timing cut, the event selection will then loop over available combinations in order to select the best available beam photon. This is done by selecting the beam photon which reconstructs the missing mass squared which is closest to zero. After enforcing this criteria, it is guaranteed that only one combination per event will survive. After this selection of events, an additional cut is placed on the data which enforces exclusivity. This is done by only allowing events with a missing mass squared between $-0.02 GeV^2/c^4 \leq MM^2 \leq 0.02 GeV^2/c^4$. The enforcement of exclusivity removes any background that did not prorperly conserve the measured four momentum from the $\gamma p \rightarrow pK^+K^-\gamma\gamma$ reaction. To finalize this section Table 2 is a summarized list of all cuts performed by this analysis.

2.2 Tabular Summary of Particle Identification Cuts

3 Investigation of $\phi\eta$ correlation by means of K^+K^- Vs $\gamma_1\gamma_2$ Invariant Mass Plot

The image illustrated in Figure 45 is the data in question. On the vertical axis is the K^+K^- invariant mass and on the horizontal axis is the $\gamma_1\gamma_2$ invariant mass. To be absolutely clear, this is a plot of invariant mass versus invariant mass and is therefore not a Dalitz Plot. Some interesting features contained within the image are the clear vertical bands for the π^0 and η resonances which have large decay modes to $\gamma\gamma$ final states. In addition, one can also observe a horizontal band slightly above $1 \frac{GeV}{c^2}$ which corresponds to the ϕ meson decaying to a K^+K^- final state. This analysis will focus on the region where the ϕ meson and η meson bands cross in order to determine if their intersection region contains some type of correlation.

Particle	Detector	ΔT Cut [ns] (2σ)
Proton	BCAL	$\pm$ 0.6
Proton	FCAL	$\pm$ 1.0
Proton	TOF	$\pm$ 0.4
K^+	BCAL	$\pm$ 0.7
K^+	FCAL	$\pm$ 0.8
K^+	TOF	$\pm$ 0.2
K^-	BCAL	$\pm$ 0.7
K^-	FCAL	$\pm$ 0.8
K^-	TOF	$\pm$ 0.2
γ	BCAL	$\pm$ 1.0
γ	FCAL	$\pm$ 1.1

Table 1: A table with timing cut values for all final state particles in the reaction $\gamma p \to pK^+K^-\gamma_1\gamma_2$. The values of the timing cuts change depending on both the particle species and detector system resolution. It should be noted that the final state photons only have the calorimeters as possible timing detectors. This is due to the fact that they do not interact with the TOF detector.

#	Description of Cut	Reference
1	Timing cuts for all final state particles	Table 1
2	Vertex cuts for all final state particles	Figures 3a, 3b
3	Beam timing cut	Figure 1
4	Beam energy cut	Figure 2
5	Proton dE/dX cut	[Paper]
6	Fiducial cut for final state photons	Subsec: 2.0.3
7	Kaon timing only from TOF	Figure 36c
8	Strangeness Conservation	Figure 38
9	Two Photon Cut	Subsec: 2.0.3
10	γ_{Beam} with MM^2 closest to zero	Subsec:2.1

Table 2: A list which summarizes all cuts used to identify $\gamma p \to pK^+K^-\gamma\gamma$.
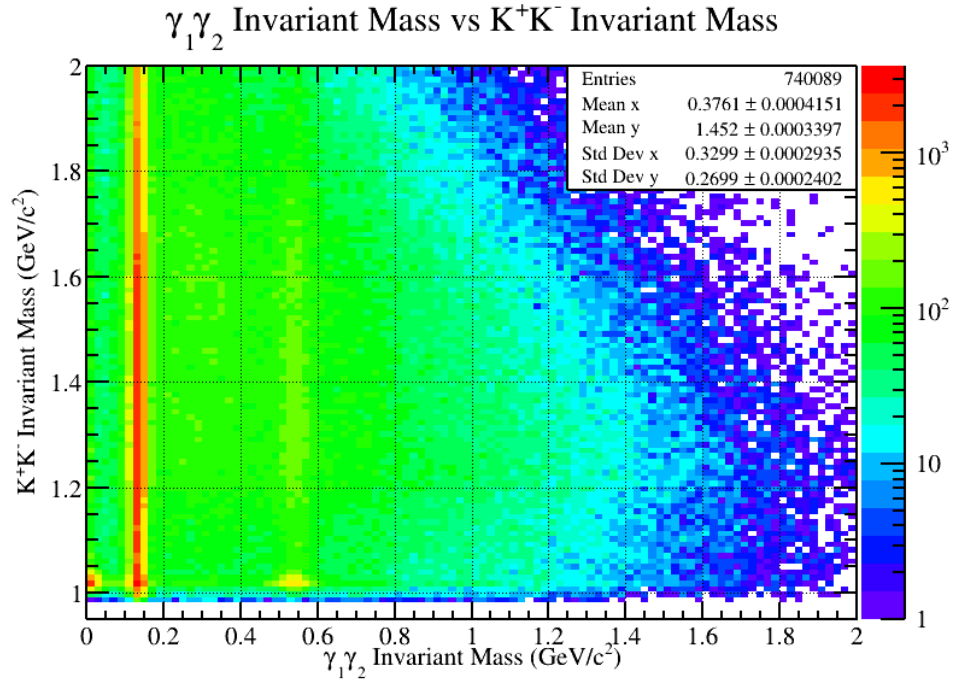
Figure 45: A two dimensional invariant mass plot with the K^+K^- invariant mass on the vertical axis, the $\gamma_1\gamma_2$ invariant mass on the horizontal axis, and a logarithmically scaled z axis. Some interesting features contained within the image are the clear vertical bands for the π^0 and η resonances which have large decay modes to $\gamma\gamma$ final states. In addition, one can also observe a horizontal band slightly above 1 $\frac{GeV}{c^2}$ which corresponds to the ϕ meson decaying to a K^+K^- final state.

3.1 Cuts on the 2D Invariant Mass Plot

In order to analyze the $\phi\eta$ region of this data, only events which fall within $\pm 10\sigma_\phi$ away from the ϕ peak and $\pm 10\sigma_\eta$ away from the η peak will be considered. This was done by taking different slices of either the $\gamma\gamma$ or K^+K^- data, then projecting the invariant mass distribution onto the opposite axis. For example, there were five different ϕ mass regions studied in this analysis. Each fit corresponds to a different $\gamma\gamma$ mass range. The $\gamma\gamma$ mass ranges are all $4\sigma_\eta$ in width, and span a total mass range of $m_\eta - 10\sigma$ to $m_\eta + 10\sigma$. An illustrated example with labeled cut lines is provided in Figure 46. It should be noted that the analysis of the η mass was not studied symmetrically about the ϕ due to the fact that going more than $m_\phi - 6\sigma_\phi$ away from the ϕ peak would result in no events because of the K^+K^- threshold.
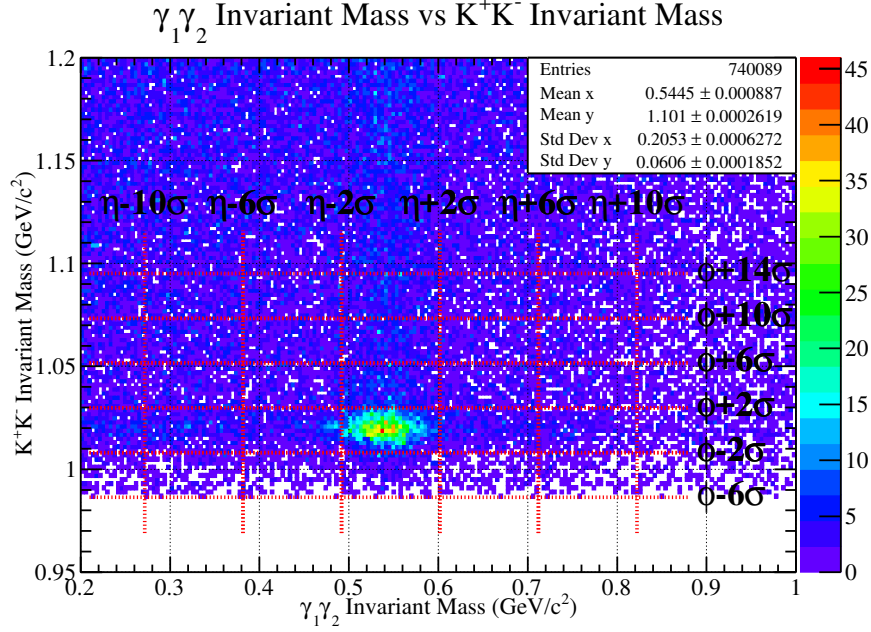
Figure 46: An illustrated example of the cuts used for studying the correlation of $\phi\eta$. The figure above is a two dimensional invariant mass plot which clearly shows an η band spanning the vertical direction at $\sim 0.547 GeV/c^2$ and a ϕ band spanning the horizontal direction at $\sim 1.02 GeV/c^2$. The red vertical and horizontal cut lines provide the ranges used to study $\phi\eta$ correlation. Examples of what the projected ranges look like are provided in Figures [47][48].

3.2 Projections and Fits for ϕ and η

Once the data had been cut and projected in the ten different mass regions, the ϕ and η peaks were fit. In the instance of the ϕ meson, the signal plus background events were fit with a Gaussian plus a second degree polynomial. The fit range used in each histogram projection for the ϕ meson spans from $m_\phi - 6\sigma_\phi$ to $m_\phi + 30\sigma_\phi \ \frac{GeV}{c^2}$. The unusually large fit range was necessary in order to properly estimate the background surrounding the ϕ mass. In the instance of the η meson, the signal plus background events were fit with a Gaussian plus a first degree polynomial due to the relatively flat background surrounding the η peak. The fit range used for the η meson spans $m_\eta \pm 6\sigma_\eta \ \frac{GeV}{c^2}$. The resulting fits are provided in the images below where the blue line represents the fit for all events (signal plus background), the green line represents the Gaussian fit (signal events), and the red line represents the polynomial fit (background events). Each histogram contains a title with brackets at the end. The arguments encapsulated by the brackets is the cut range that was used for that particular projection sample.
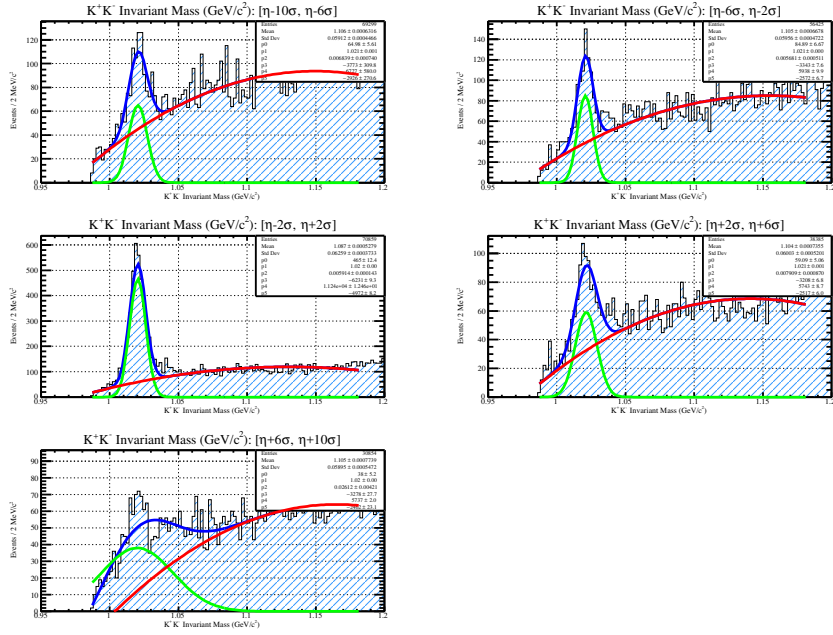
Figure 47: A collection of different K^+K^- Invariant Mass projections as a function of $\gamma_1\gamma_2$ Invariant Mass cut range. Each sub figure includes a red line which is a second degree polynomial used to estimate the shape of the background, a green line which is a Gaussian used to estimate the ϕ signal peak, and a blue line which the sum total of the polynomial fit and Gaussian fit. Lastly, each sub figure also includes the $\gamma_1\gamma_2$ Invariant Mass cut range used to produce the projected figure. This information is in the title of the histogram, inside the brackets.
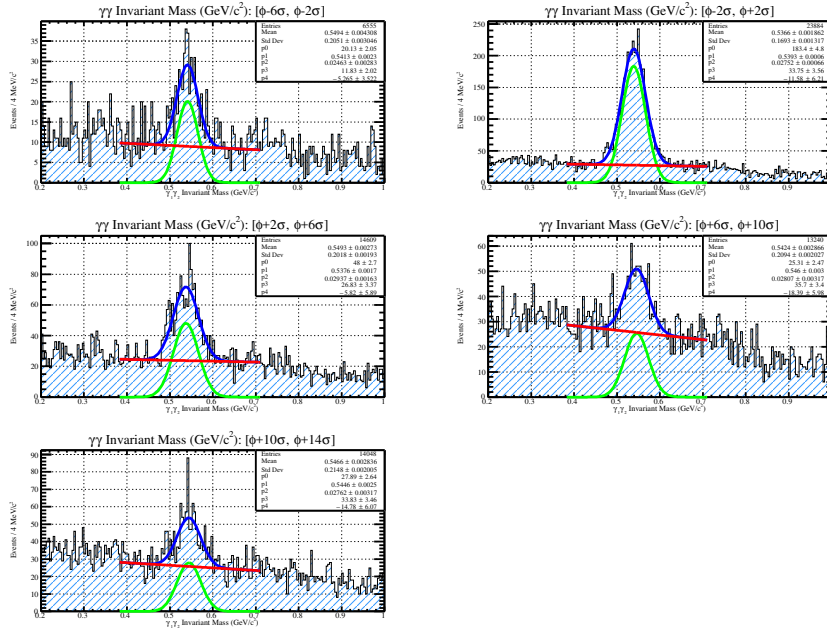
Figure 48: A collection of different $\gamma_1\gamma_2$ Invariant Mass projections as a function of K^+K^- Invariant Mass cut range. Each sub figure includes a red line which is a first degree polynomial used to estimate the shape of the background, a green line which is a Gaussian used to estimate the η signal peak, and a blue line which the sum total of the polynomial fit and Gaussian fit. Lastly, each sub figure also includes the K^+K^- Invariant Mass cut range used to produce the projected figure. This information is in the title of the histogram, inside the brackets.

3.3 Integration Results for ϕ and η

After obtaining accurate fits for all regions, integration of the Gaussian fit functions was performed. Each Gaussian fit was integrated in the range of $m \pm 2\sigma_m$, where m represents either m_ϕ or m_η mass coupled with the addition or subtraction of two standard deviations in each direction. Integration of the Gaussian fits provides an accurate estimate for the number of signal events that exists for that particular sampling of $\gamma\gamma$ Vs K^+K^- phase space. The estimated number of signal events have been added to the 2D mass plot below, with the exception of the $\phi\eta$ intersection region which will be discussed in more detail in the Conclusion section.
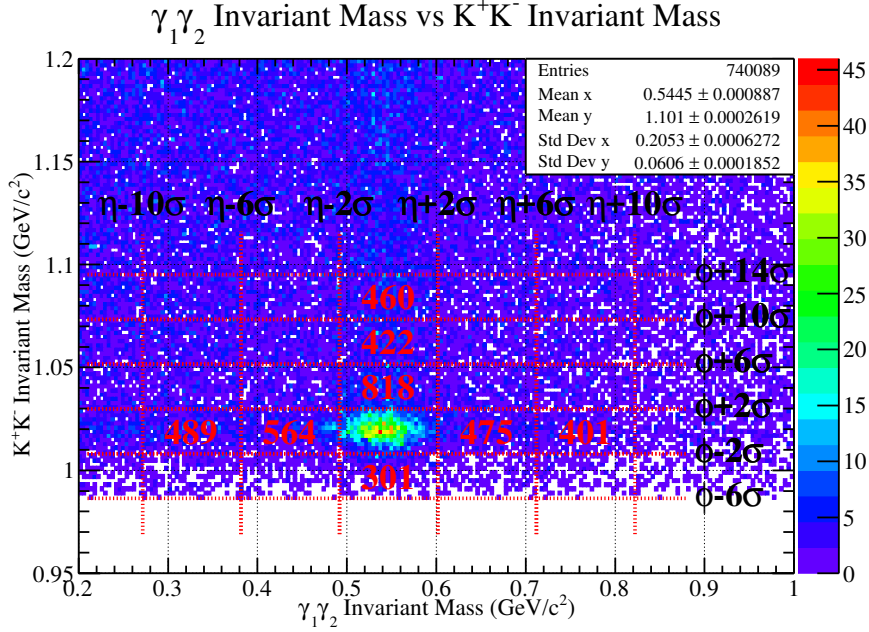
Figure 49: The above figure provides the number of events for each projection range studied. These numbers were calculated by means of integrating the Gaussian fit for either the ϕ or η between $\pm 2\sigma$. The vertical column of numbers represents the number of η events for a given K^+K^- Invariant Mass, and the horizontal row of numbers represents the number of ϕ events for a given $\gamma_1\gamma_2$ Invariant Mass. The number of events observed in the intersection region was not included in the figure due to the amount of space available. There numbers can be found in the Conclusion section.

3.4   Additional Statistics Study

In addition to the analysis mentioned above, an additional study has been included which simply samples the phase space and records the number of events within that sample. To do this, the same cut ranges as before were used. The only difference is that only the 3x3 grid surrounding the $\phi\eta$ intersection region. Each region is a box cut which is exactly $4\sigma_\phi$ x $4\sigma_\eta$ in area. Each area is given an index to denote the specific region of phase space that is being sampled and an illustration is provided below.
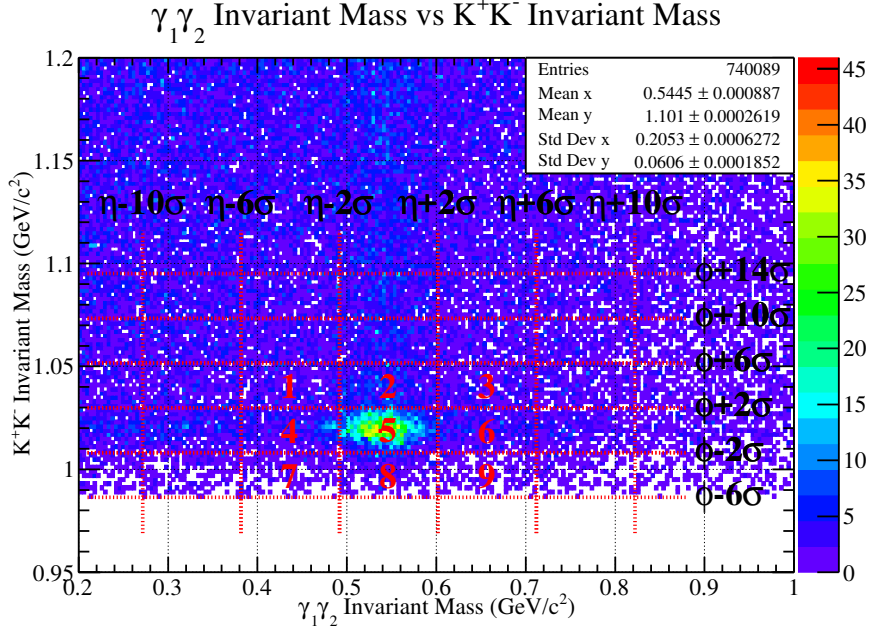
Figure 50: An illustration to provide the reader with an idea of how the second statistics study is performed. All of the cut ranges are identical to the first statistics study. The numbers provided in the figure do not represent events, but simply indicate the index associated with a certain area of $\phi\eta$ phase space.

Using the diagram as a reference, it is easy to see that the average number of background events within this phase space can be calculated using the formula $N_{BG} = (A_1 + A_3 + A_7 + A_9)/4$. Additionally, the average number of ϕ and η events plus background can be calculated using $N_{BG} + N_\phi = (A_4 + A_6)/2$ and $N_{BG} + N_\eta = (A_2 + A_8)/2$, respectively. Lastly, quantification of the number of correlated events in region 5 is possible by using $N_{BG} + N_\phi + N_\eta +$

66

$N_{correlated} = A_5$. A figure with the number of events contained within each region of phase space is given below.
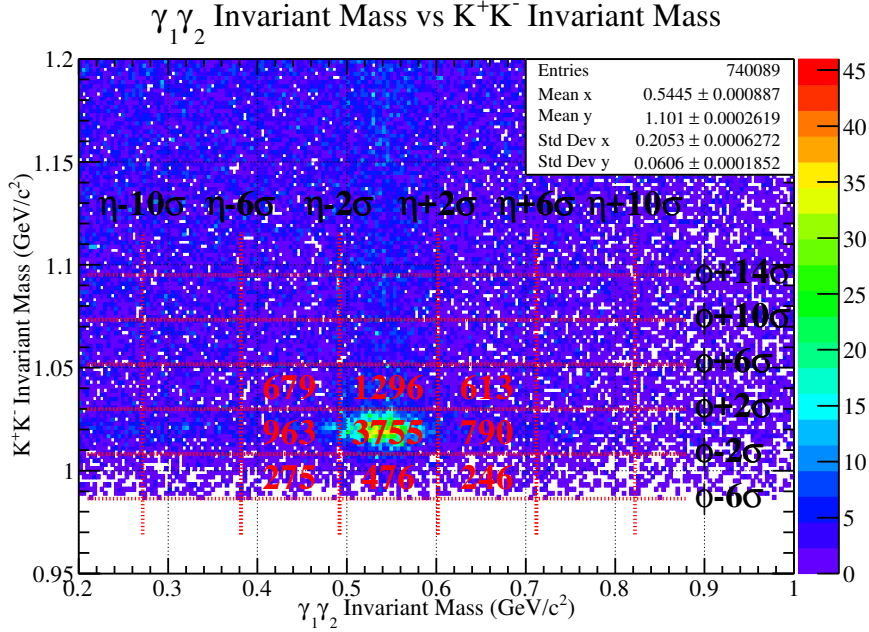
Figure 51: This figure shows the total number of counts in each box. To b be clear, the numbers in each are do not represent the total number of events, but rather the precise amount of statistics contained. Upon inspection, one can see evidence of $\phi\eta$ correlation, which is explained in the Conclusion section.

The first step of this simplistic analysis is to determine what the average number of background events is, which is calculated to be 453. Knowing this, the number of ϕ and η events can now be determined by using the equations $N_{BG} + N_\phi = (A_4 + A_6)/2$ and $N_{BG} + N_\eta = (A_2 + A_8)/2$, and then subtracting the average number of background events. Upon doing this, it was fount that N_ϕ is 423 and N_η is 433. To complete this analysis, the number of correlated events can now be estimated by using the equation $N_{BG} + N_\phi + N_\eta + N_{correlated} = A_5$, and subtracting N_{BG}, N_ϕ, and N_η. The total number of correlated events is 2446. This calculations shows once again that there is an overflow of events within the $\phi\eta$ intersection region that cannot be explained by the presence of background or the addition of events from the ϕ and η bands.

3.5 Conclusion of K^+K^- Vs $\gamma_1\gamma_2$ Invariant Mass Plot Study

Given that the number of estimated signal events has been calculated for the ϕ and η bands which neighbor the $\phi\eta$ intersection region, the expected number of events will be in the $\phi\eta$ intersection region using averages can be estimated. Taking the numbers from the two dimensional plot above and rounding to the nearest integer, the average number of signal events in the ϕ band is $\overline{\phi_{events}} \sim 482$, and the average number of signal events in the η band is $\overline{\eta_{events}} \sim 500$. Therefore, it is estimated that the number of signal events within the $\phi\eta$ intersection region should be just shy of 1000 events if there is no correlation present. After integrating the Gaussian fit for the ϕ and η mesons in the $\phi\eta$ intersection region, it was found that there were 3194 events corresponding to the ϕ fit, and 2993 events corresponding to the η fit. Both of these fits not only yield roughly the same number of events, but they also produce an event estimate which is a factor of three higher than what would have been there from the ϕ and η bands alone. The large increase in event statistics within the $\phi\eta$ intersection region strongly suggests that some type of correlation is present within this area of K^+K^- $\gamma\gamma$ phase space. It should be clearly noted that the nature of this correlation is not identified at this time. Moreover, it is unclear from this study as to whether or not the bound stats is mesonic or baryonic in nature. Additional studies on this area of phase space need to be performed in order to establish that this spike in statistics is not coming from the $\gamma p \rightarrow N^*\phi$, $N^* \rightarrow p\eta$ topology.

4 Monte Carlo Features of $\gamma p \rightarrow p\phi\eta$

In order to better understand the acceptance of the $\gamma p \rightarrow p\phi\eta$ topology in the GlueX spectrometer, a generated Monte Carlo sample was analyzed. More specifically, the exact sample that was produced was $\gamma p \rightarrow pX; X \rightarrow \phi\eta; \phi \rightarrow K^+K^-; \eta \rightarrow \gamma\gamma$. This Monte Carlo sample consisted of 170 k generated events for each of the run numbers 030408, 030620, 030802, and 031029. There run numbers were chosen because the first two have beam polarizations in the PARA/PERP directions at low intensity, and the second two have PARA/PERP orientations at high intensity. The total number of generated $\phi\eta$ events is therefore 680 k. The events were generated using a coherent bremsstrahlung beam energy spectrum and a t-slope of 4 $(GeV/c^2)^2$. To be more clear, the thrown beam particles were not polarized in this sample; only the beam energy spectrum matched that of a polarized beam spectrum (Figure [52]). All final state particle kinematics were generated using

the ROOT object TGenPhaseSpace. The generated final state phase space was flat and therefore did not include any spin information from parent or daughter states. The $\gamma, K^+, K^-, \phi, \eta$, and p particles were generated using the invariant mass values provided in the PDG. The photoproduced X mass was randomly distributed between the lower kinematic limit $m_\phi + m_\eta$ and the upper kinematic limit which is a function of the thrown beam energy.
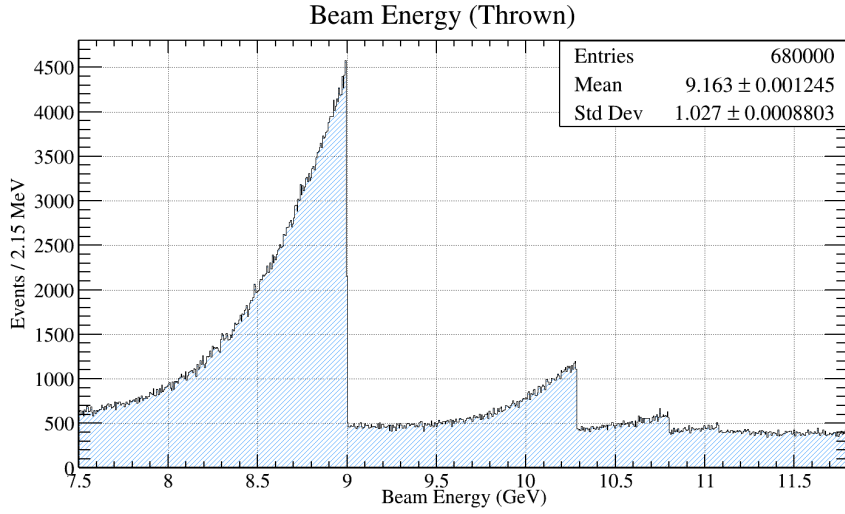
Figure 52: A histogram which includes the thrown beam statistics from the generated Monte Carlo example. In the figure one can easily see the coherent peak which maximizes at 9 GeV. Additionally, one can also see other secondary peaks at higher energy.

An example of what the generated beam energy distribution looks like for this Monte Carlo sample is given in Figure [52]. It should be noted that this particular Monte Carlo sample only generated beam energies between the values of $7.5 - 11.8$ GeV. The reason for the lower energy boundary of the beam energy spectrum is to both cut out potential areas of background due to low energy beam photons and to allow a larger sampling of polarized photons when a beam asymmetry study is performed with actual data. The high energy cut off of 11.8 GeV is simply there to match the high energy cut off of the Spring 2017 run.

69
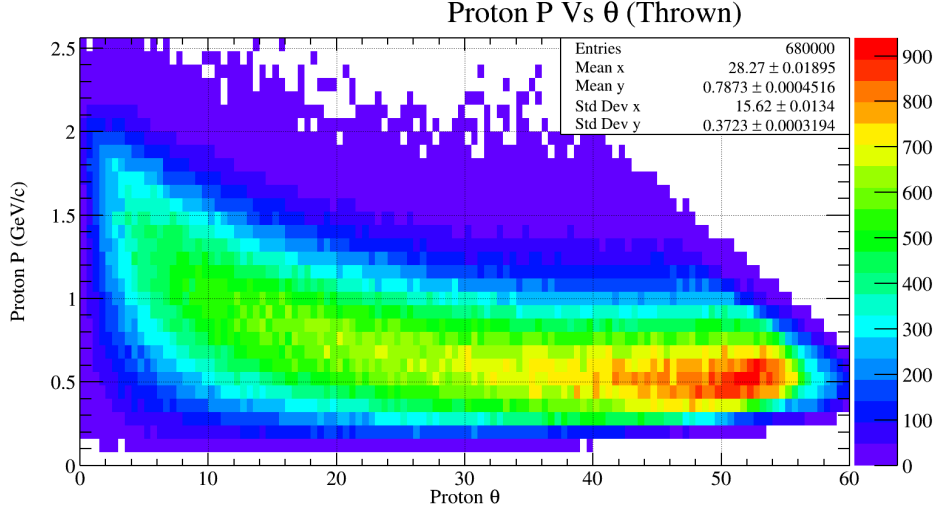
Figure 53: A two dimensional histogram which includes the thrown kinematic information of the recoil proton. In the histogram, the horizontal axis represents the generated θ angle in the lab frame, and the vertical axis represents the generated momentum magnitude in the lab frame. One interesting feature of this Monte Carlo data is that the protons kinematics appear to be constrained between $[0.2 - 2.0]GeV/c$ in momentum, and $[0.0 - 60.0]$ in angle.

Momentum versus theta distributions are also provided in Figures [53], [54], [55], and [56]. These figures are not accepted Monte Carlo, they are only the generates four vectors of the final state particles before running hdgeant, mcsmear, or `hd_root`. Still, the figures provide some insight into the expected kinematic distributions of the final state particles. For example, Figure [53] displays the momentum versus theta distribution for the recoil proton. This figure shows that we should expect the proton to have a very low momentum and high recoil angle relative to the beam direction for this final state.
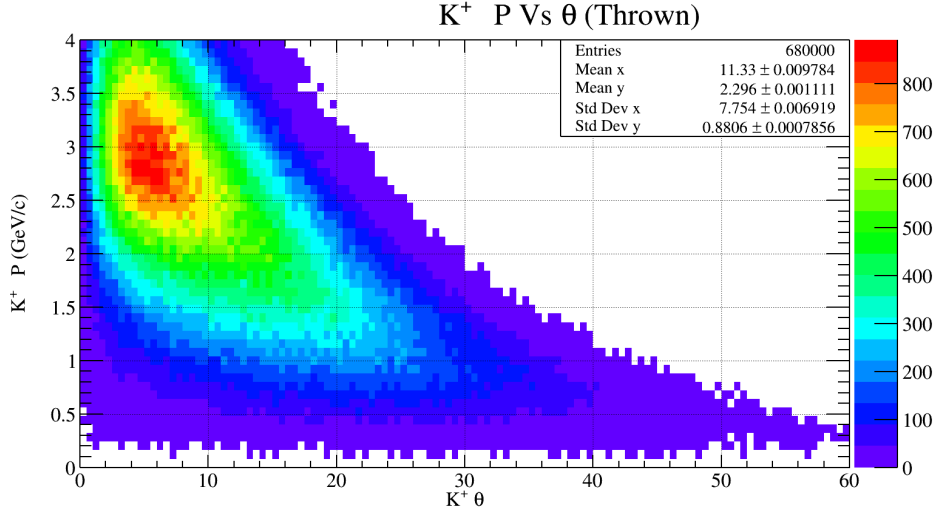
Figure 54: A two dimensional histogram which includes the thrown kinematic information of the generated K^+. In the histogram, the horizontal axis represents the generated θ angle in the lab frame, and the vertical axis represents the generated momentum magnitude in the lab frame.
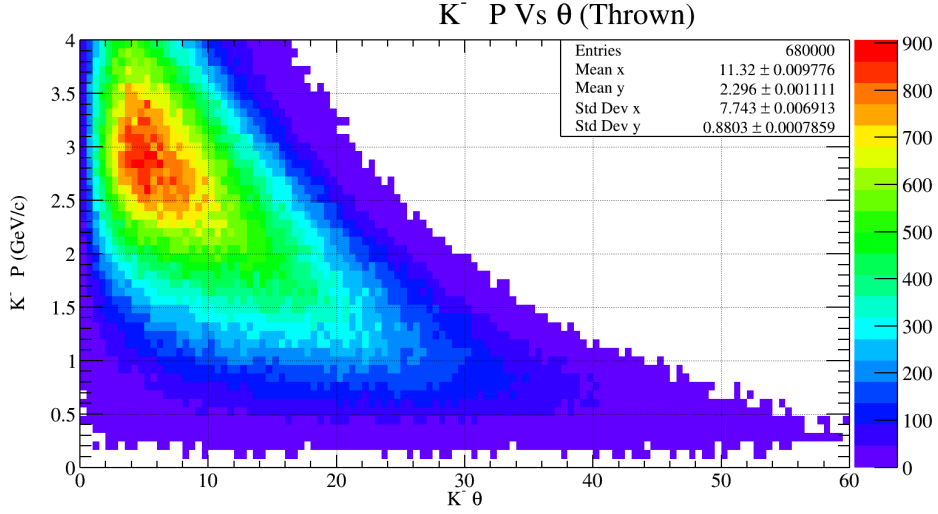
Figure 55: A two dimensional histogram which includes the thrown kinematic information of the generated K^-. In the histogram, the horizontal axis represents the generated θ angle in the lab frame, and the vertical axis represents the generated momentum magnitude in the lab frame.

Additionally. Figures [54][55] show the same plot but for K^+ and K^-,

71

respectively. In these figures, it is clear that Kaons will preferentially travel towards the TOF/FCAL and with a momentum that should include a lot of pion contamination (see Figures [18][26] for more information on pion contamination at high momentum).
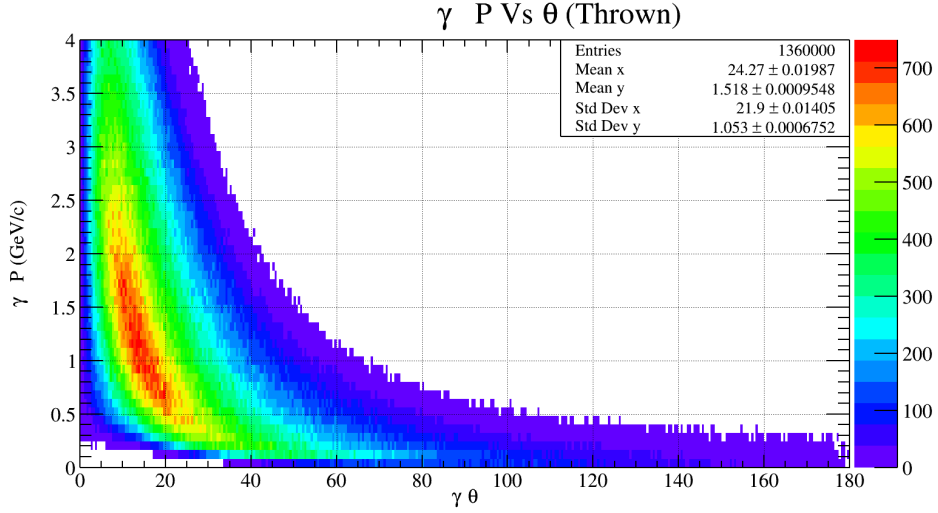
Figure 56: A two dimensional histogram which includes the thrown kinematic information of the generated photons. In the histogram, the horizontal axis represents the generated θ angle in the lab frame, and the vertical axis represents the generated momentum magnitude in the lab frame.
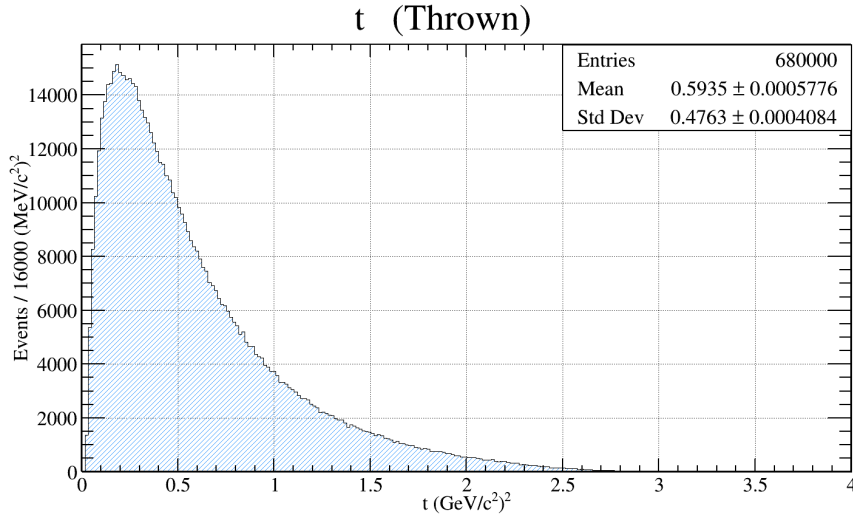
Figure 57: A histogram which includes the generated spectrum for the Mandelstam variable, t. The most important feature in this histogram is the fact that the majority of generated events come from low momentum transfer.

Lastly, Figure [56] shows that the final state photons will be mostly forward going and therefore we should expect to see the majority of them interacting with the FCAL rather than the BCAL. It comes as no surprise that the Monte Carlo has generated photons and kaons that favor the forward direction, while the recoil proton has low momentum and a highly transverse direction. This is simply a consequence of the fact that a 'low t' interaction was programmed into the Monte Carlo, resulting in Figure [57].

The last few figures I wish to discuss in this section involve the study of invariant mass spectra. The first of which is the invariant mass of $\phi\eta$ (Figure [58]) which shows a flat distribution between the values of 1.5 to 3 GeV/c^2; then the distribution drops off drastically until 3.3 GeV/c^2; and then less drastically from 3.3 to 4 GeV/c^2. These features may seem incorrect at first glance since the generated Monte Carlo mass is supposed to be flat. However, upon further inspection, it is clear that these features manifest themselves within the Monte Carlo data because of the shape of the beam spectra. The best way to see this behaviour is by considering Figure [59]. This figure shows the generated mandelstam variable t on the vertical axis, and the generated $\phi\eta$ mass on the horizontal axis. Since t is the momentum transfer, it is directly correlated with the beam photon and therefore will exhibit some coherent bremsstrahlung structure. This structure can be seen in Figure [59] where there is clear evidence of the beam energy spectra influencing the behavior of the $\phi\eta$ mass. We know from Figure [52] that the most

dominant statistics will come from the coherent edge at 9 GeV and should drop off drastically beyond that point. This feature of the data is clearly seen in Figure [59] and is therefore the reason for the odd behavior seen in Figure [58].
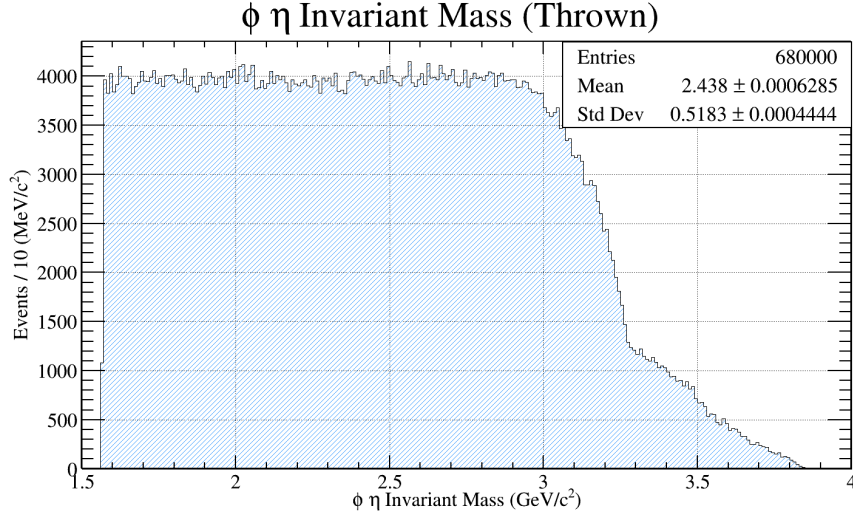
Figure 58: A histogram which includes the generated $\phi\eta$ invariant mass. In the figure one can easily see that the invariant mass of the $\phi\eta$ remains flat until it reaches $\sim 3.0 GeV/c^2$. From that point, the invariant mass falls sharply until $\sim 3.3 GeV/c^2$; and then continues to fall at a slower rate. This feature of the invariant mass is directly related to the fact that a coherent bremsstrahlung beam energy spectrum was used. The drastic drop off in statistics in the mass range of $3.0 - 3.3 GeV/c^2$ is caused by the primary coherent peak at $9.0 GeV$. To visualize this more clearly, see Figure [59].
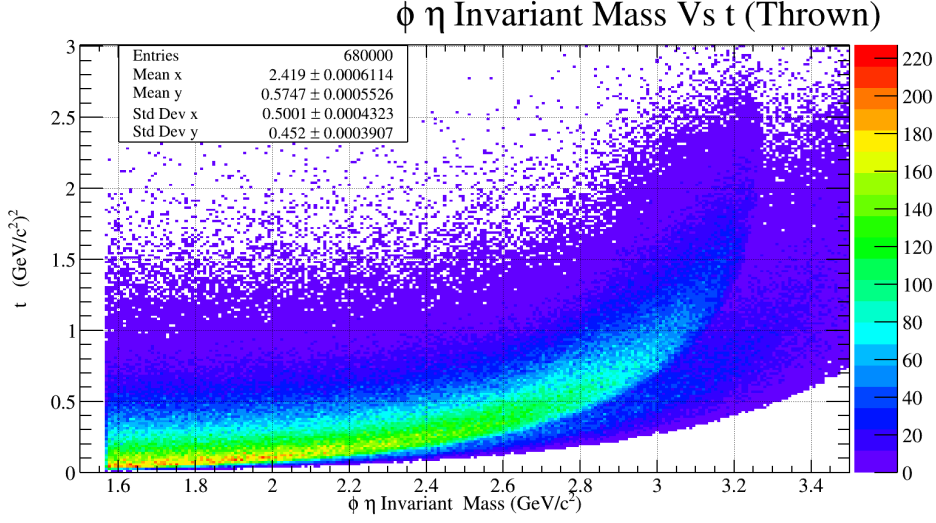
Figure 59: A two dimensional histogram which includes the generated $\phi\eta$ invariant mass on the horizontal axis and the Mandelstam t variable on the vertical axis. In the figure one can easily see the effect that the coherent peak has on the shape of the phase space. The effect can be seen in even greater detail in Figure [58].

5 Probabilistic Weightings for $\phi\eta$ Events

Throughout the course of history, physicists have tried clever ways of reducing the amount of background that is present under a given signal, or resonance. An example of this may be the classic side band subtraction, where the signal region will be defined by some average mass value, plus or minus a well defined width, or sigma. If one were to perform a cut about this region after particle identification and cuts, there may still be a good deal of background underneath the peak. In order to eliminated the background under the signal, one thing to do is use the background near the peak as reference for subtraction. To do this, one would use background events that are located at both higher and lower mass values far away from the signal, so long as the total mass range used is equal to the mass range for selecting the signal region. The side band subtraction method works well for some physics analyses, but not all. Side band subtraction is an issue with this analysis because the primary purpose is to observe structures in the $\phi\eta$ invariant mass spectra. Performing a side band subtraction is problematic because it allows events well below the $\phi\eta$ threshold mass to exist in the background spectra. Subtracting off these events from the primary signal region results in a final $\phi\eta$ invariant mass spectra which has negative event counts at low

75

$\phi\eta$ mass values. Therefore, it is imperative to seek alternative background subtraction methods. The method that will be presented in this analysis uses a probabilistic weighting procedure which will be explained in this section.

5.1 Introduction to Probabilistic Event Weightings

One of the issues with a side band subtraction method is that it treats all events with a relative weight of one. The purpose of this section is to describe and propose a new method which does not treat all events with a value of one, but instead assigns a fractional weight to an event based off of a quality factor, or Q-factor. The quality value idea was first introduced in 2008 by M. Williams, M. Bellis, and C. A. Meyer in a paper titled "*Separating Signals from Non-Interfering Backgrounds using Probabilistic Event Weightings.*". The paper considers a generic situation in which there is a data set of n total events described by m coordinates, which will be written as $\vec{\xi}$. Within the data set, there exists n_s total signal events and n_b total background events, and therefore $n = n_s + n_b$. In addition, both the signal and the background distributions are functions of the coordinates, such that $S(\vec{\xi})$ can be thought of as a signal distribution and $B(\vec{\xi})$ can be thought of as a background distribution. Contained within the set of coordinates $\vec{\xi}$, there exists a *reference coordinate* (ξ_r) with which we know the functional form of $S(\xi_r)$ and $B(\xi_r)$ *a priori*. The reference coordinate that is used in this thesis as well as in the paper mentioned above is the invariant mass of a final state. For many invariant mass distributions, the functional form of the signal distribution, $S(\xi_r)$ can be represented with a well known signal function. Some examples of well known signal functions are Gaussian, Voigtian, and Breit-Wigner distributions. In addition, the background distribution, $B(\xi_r)$, can be represented with an nth degree polynomial function.

Since the signal and background distributions are not necessarily known *a priori* for the other coordinates, we use them to calculate a kinematic distance on an event by event basis. This is done by using the Equation (4).

$$d_{ij}^2 = \sum_{k \neq r} \left[\frac{\xi_k^i - \xi_k^j}{R_k} \right]^2 \tag{4}$$

In Equation(4), the total kinematic distance is calculated between some event i, as compared to another event j. This is done by taking the sum of the squared difference over all of the coordinates ξ_k, except for the reference coordinate ξ_r. The difference between coordinates is then normalized by the parameter R_k. The parameter R_k is the total maximum difference for a given coordinate ξ_k. An example of this may be the measurement of an azimuthal

angle which spans from 0 to 2π. Therefore, the R_k for an azimuthal angle would be 2π. Upon closer inspection, one should realize that Equation(4) is simply a representation of the Pythagorean Theorem in a normalized $m - 1$ dimensional kinematic space.

After calculating all of the kinematic distances for an event i, as compared to all other events within the data set $1...j...n$, it is then necessary to only keep the *nearest neighbors*. The nearest neighbors, by definition, are a subset of the n events which have the smallest kinematic distance with respect to the ith event that is being considering. The purpose of only keeping the nearest neighbors stems from the assumption that a signal or background event with certain kinematic measurements, will share similar kinematic values with other signal or background events, respectively. The number of nearest neighbors for a set of events n is an arbitrary amount, and does not greatly effect the quality factor calculation; so long as the amount is a small fraction of the total events n. Once the list of nearest neighbors is known for the ith event, it is then necessary to plot their reference coordinate, ξ_r, onto a histogram. This histogram should contain a well understood signal distribution $S(\xi_r, \vec{\alpha})$, and background distribution $B(\xi_r, \vec{\alpha})$, as mentioned above; where $\vec{\alpha}$ is the set of known/unknown fit parameters used to describe the signal or background distribution. The histogram will then be fit by the sum of the signal and background distributions such that $F(\xi_r, \vec{\alpha}) = S(\xi_r, \vec{\alpha}) + B(\xi_r, \vec{\alpha})$. The quality factor can then be calculated by using the reference coordinate value for the ith event and plugging it into the signal and background functions by using Equation(5), where $\hat{\alpha}$ is the set of fitted parameters for the signal or background distribution.

$$Q_i = \frac{S(\xi_r^i, \hat{\alpha}_i)}{S(\xi_r^i, \hat{\alpha}_i) + B(\xi_r^i, \hat{\alpha}_i)} \tag{5}$$

Once the quality factor is known for an event i, it can then be recorded and the analysis can loop over the next event and repeat the sequence all over again. Once all events have been run over, the quality factors for each event are used as a weight for plotting inside histograms. If the quality factor is correctly calculated for each event, the method should be able to separate signal from background. More specifically, if a histogram of the K^+K^- invariant mass is plotted with Q_i as the weight for the ith event, one should see a 'pure' ϕ peak with absolutely no background. In addition, if the K^+K^- invariant mass is plotted with $1 - Q_i$ as the weight for the ith event, one should see all background and absolutely no ϕ peak. Therefore, the sum of the signal histogram plus the background histogram should be equal to the K^+K^- invariant mass with all events having a weight of 1.

5.1.1 Determining the Number of Nearest Neighbors

After the kinematic distances are calculated for all events with respect to the ith event, they are the sorted in order from smallest kinematic distance to largest kinematic distance. Only the the nearest neighbors, or the set of events with the smallest kinematic distance, will be used to determine the quality factor of a given event. For this analysis, there were a total of 16,981 events after selection cuts, and the number of nearest neighbors used was 500. This number was chosen somewhat arbitrarily; it is important to pick the smallest number possible such that the events used truly are those which share the most similar kinematic features to the event that is being considering. If the number was extremely large with respect to the total number of events, the analysis will not work properly. Events that are background will have some nearest neighbors that are signal, and vice versa. Furthermore, the number number of nearest neighbors needs to be large enough such that a fit can converge with the filled histogram. If the number of nearest neighbors is too small, ROOT will fail to provide any signal or background information inside the histogram, and therefore calculation of a quality factor will be impossible. Considering these two constraints and testing with different values, it was found that the smallest number which did not result in *any* fitting failures was 500.

5.1.2 Fitting the K^+K^- Invariant Mass

Upon determining the nearest neighbors of the ith event, the next step is to plot and fit the set of K^+K^- and $\gamma_1\gamma_2$ invariant mass distributions. As mentioned above, it is extremely difficult to model the invariant mass distribution for the K^+K^- final state. Simply picking a signal distribution plus a polynomial background is not enough to properly parameterize the K^+K^- invariant mass near or around the ϕ peak. After attempting several different combinations of signal and background functions, it was found that the best way to accurately describe both the ϕ and the background near it is to use convoluted functions. A convolution is the operation between two functions which expresses how the shape of one function is modified by the other. The purpose for utilizing a convoluted function when attempting to fit an invariant mass histogram is to describe both the shape of the distribution as well as the inherent resolution of the data. Since both the ϕ peak and the background surrounding it contain similar resolutions, it is appropriate to fit the K^+K^- invariant mass distribution with the summation of a signal function plus a background function, both of which are then convoluted by a third function which manages the resolution.

The signal function chosen to describe the ϕ peak is a relativistic Breit-Wigner (Equation 6).

$$|Q_1(m)|^2 = A * |F_1(m) * \Delta_1(m)|^2 \tag{6}$$

Contained within this equation is a fit parameter, A, which simply scales the function in order to match the distribution. Also contained in this equation are two functions of mass, the Blatt-Weisskopf centrifugal-barrier factor for a spin 1 particle (Equation 7),

$$F_1(m) = \sqrt{\frac{2 * \sqrt{m^2 - m_K^2}}{\sqrt{m^2 - m_K^2} + 1}} \tag{7}$$

and a standard Breit-Wigner (Equation 8) for a particle with spin 1.

$$\Delta_1(m) = \frac{m_o * \Gamma_o}{m_o^2 - m^2 - im_o\Gamma_1(m)} \tag{8}$$

The Blatt-Weisskopf function plays an important role in the fit since it forces the signal function to be equal to zero when the K^+K^- mass is at threshold. It should be noted that $\sqrt{m^2 - m_K^2}$ appears throughout many of the equations mentioned. This smaller function represents the magnitude of the breakup momentum for either the K^+ or K^- daughter particle, given some parent mass m, in the rest frame of the parent particle. Additionally, the mass dependent width (Equation 9) also helps to describe the changing width of the ϕ due to the K^+K^- mass near threshold.

$$\Gamma_1(m) = \Gamma_o \frac{m_o}{m} \frac{\sqrt{m^2 - m_K^2}}{\sqrt{m_o^2 - m_K^2}} \frac{F_1^2(m)}{F_1^2(m_o)} \tag{9}$$

Finally, in many of the equations, m_K is the mass of a $K^{+/-}$, m_o is the ϕ mass value as determined by the fit, and Γ_o is the natural width of the ϕ. The value chosen for this parameter was taken from the PDG and is $\Gamma_o = 0.004266 \frac{GeV}{c^2}$.

Plotted along with the signal function is the background function which is simply a third degree polynomial, given by Equation (10).

$$b(m) = C_1 * (m - C_0)^3 + C_2 * (m - C_0)^2 + C_3 * (m - C_0) \tag{10}$$

The background equation has three free parameters and one fixed parameter. The free parameters are the coefficients in front of the powered terms of m; specifically C_1, C_2, and C_3. Since the background shape can drastically change due to the event and its nearest neighbors, these parameters are not

given any restriction on their values (Table 3). The one fixed parameter is C_0 which is set to $0.987354\frac{GeV}{c^2}$. This value is the smallest possible mass which can produce the K^+K^- final state, and is easily derived by simply performing the calculation $m_{K^+} + m_{K^-} = 2 * m_{K^\pm} = 0.987354\frac{GeV}{c^2}$. The purpose of fixing this parameter is force the polynomial background to have a root at the K^+K^- threshold. While attempting different fit functions to describe the K^+K^- invariant mass, it was found that the polynomial function often exaggerated, or over fit the area near the K^+K^- threshold. This caused an effect which resulted in weighted histograms that took away good events near the low mass side of the ϕ peak. Forcing the background function to be equal to zero at the K^+K^- threshold fixed this issue.

To complete the fit of the K^+K^- invariant mass, the signal and background function are added together, then convoluted by a Gaussian in order to compensate for the kaon resolution of the GlueX spectrometer. Although the signal and background functions mentioned above had to be programmed by hand, the convolution of these functions with a Gaussian could be fed into the ROOT library using the TF1Convolution object. More precisely, the total function used to describe the K^+K^- invariant mass for all events is given in Equation (11).

$$T(m) = \int \left[s(m') + b(m') \right] G(m - m') dm' \qquad (11)$$

In the equation above, m' is simply a dummy variable for integration, and m represents the K^+K^- invariant mass. The function $s(m')$ is a relativistic Breit-Wigner (Equation 6), and the $b(m')$ is the polynomial background function referenced in Equation (10). Finally, $G(m - m')$ is the Gaussian function which is responsible for describing the resolution. This particular Gaussian function has one free parameter, and one fixed parameter. The free parameter is the width of the Gaussian, and the fixed parameter is the mean of the Gaussian which is simply set to zero. Because the Gaussian is being convoluted over the range of the fit, the value of the mean in this instance does not matter. Adding all things together, the total function listed in Equation (11) has one independent variable, two fixed parameters, and six free parameters, half of which are restricted (Table 3). Once a fit has converged, the parameters of the total function can be extracted and used to plot a signal function and a background function. This procedure is mathematically allowed due to the distributive property of convolutions; and therefore the final background and signal function can be written in Equation (12) and Equation (13), respectively.

80

$$B(m) = \int b(m')G(m - m')dm' \tag{12}$$

$$S(m) = \int s(m')G(m - m')dm' \tag{13}$$

Examples of different fits of the K^+K^- invariant mass distributions have been provided in Figures[60][61][62]. Each figure contains a blue line which represents the total fit of the data (Equation 11), a green line which represents the signal portion of the fit (Equation 13), and a red line which represents the background portion of the fit (Equation 12). Located within each plot is also a vertical arrow which is pointed in the downward direction. This arrow represents the invariant mass value of the event for which the quality factor is being calculated. Also contained within each figure is a legend with the values of the parameters for each fit.

temp_hist

Entries	500
χ^2 / ndf	78.68 / 79
Amplitude	46.92 ± 4.82
Phi Mass	1.019 ± 0.000
p1	-1202 ± 512.9
p2	120.3 ± 28.4
Resolution	0.002777 ± 0.000542

Figure 60: A fit which will result in an extremely low quality factor due to the very few signal events in comparison to background events at the location of the arrow, or invariant mass of the event being considered.
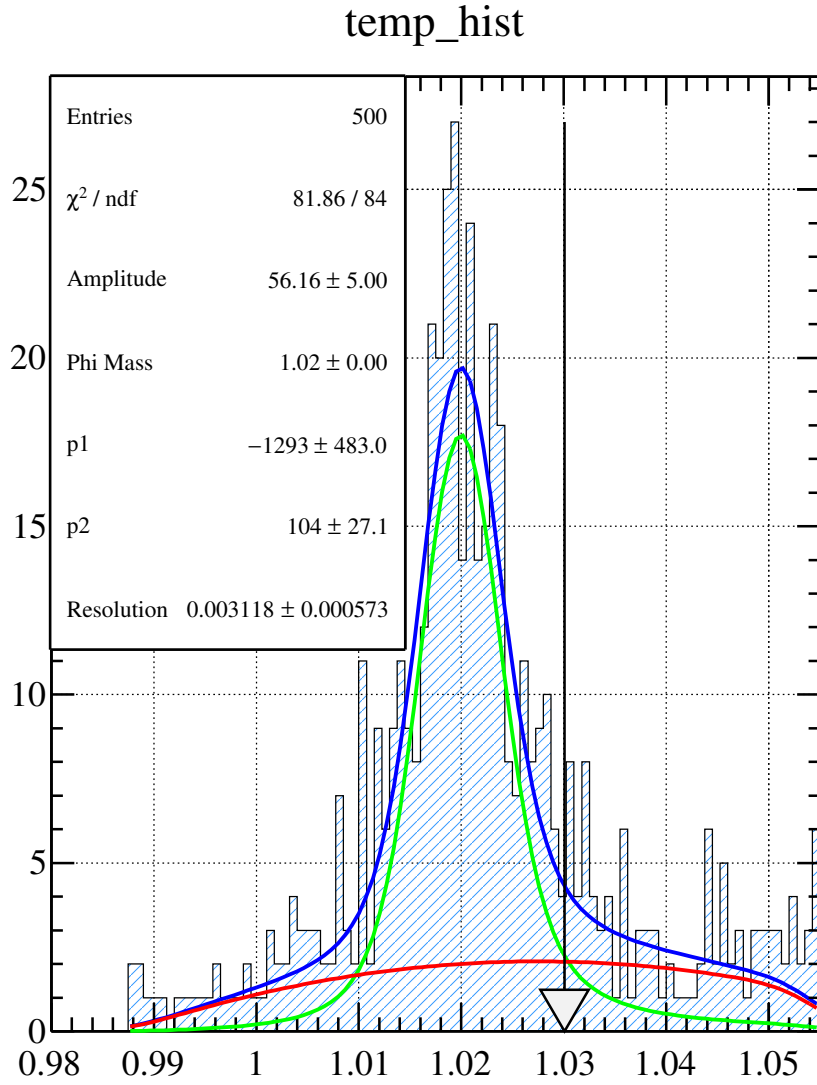
Figure 61: A fit which will result in a quality factor around 0.5, due to the fact that there are roughly the same signal and background events at the location of the arrow, or invariant mass of the event being considered.

temp_hist

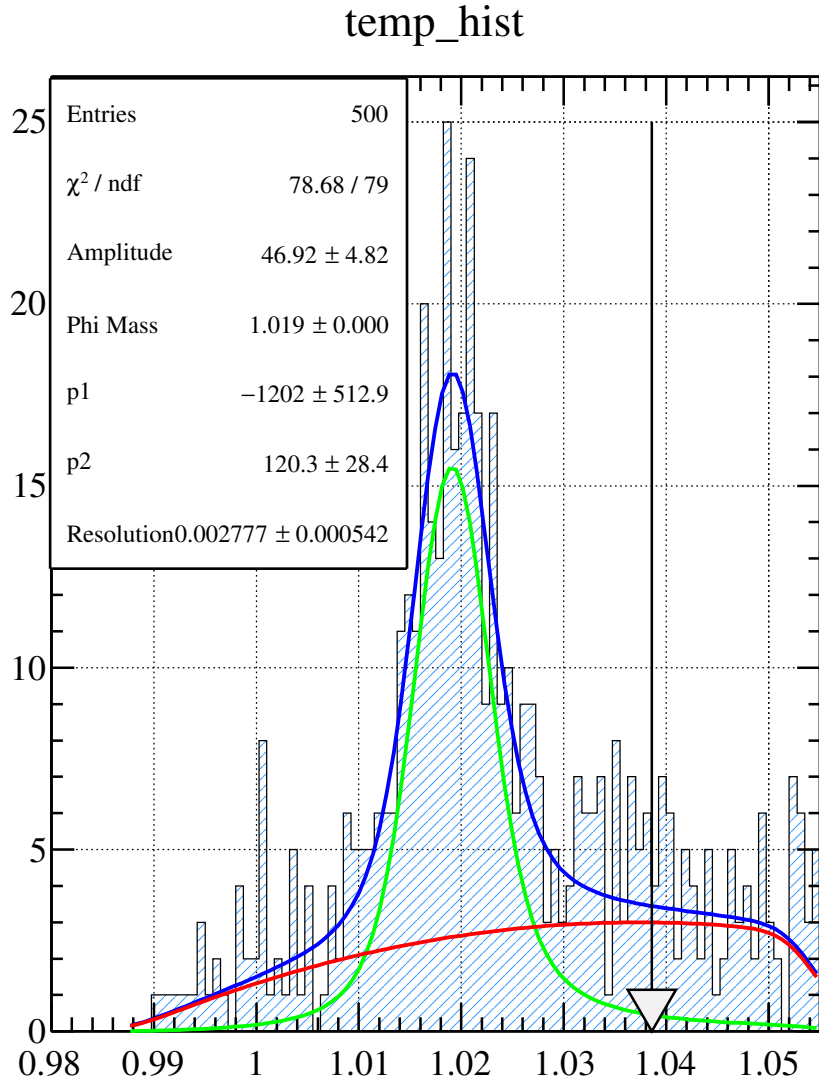|	
Entries	500
χ^2 / ndf	78.87 / 74
Amplitude	63.47 ± 5.26
Phi Mass	1.02 ± 0.00
p1	−1065 ± 515.0
p2	85.79 ± 29.36
Resolution	0.003194 ± 0.000450

Figure 62: A fit which will result in a very high quality factor due to the large number signal events in comparison to background events at the location of the arrow, or invariant mass of the event being considered.

K^+K^- Invariant Mass Functions:

Function	Parameters	Initial Values	Restricted Range
Relativistic B.W.	Amplitude	10	$0 - 100$
	m_ϕ	1.019	$1.01 - 1.03$
3rd Degree Polynomial	C_0	0.987354	Fixed
	C_1, C_2, C_3	$-1200, 200, 200$	Free
Gaussian	μ	0	Fixed
	σ	0.005	$0 - 0.05$

Table 3: A table which summarizes the parameters and functions used to fit the K^+K^- invariant mass histograms.

5.1.3 Fitting the $\gamma_1\gamma_2$ Invariant Mass

On top of fitting the K^+K^- invariant mass, it is also necessary to fit the $\gamma_1\gamma_2$ invariant mass. Fitting this distribution is far more simple than what was needed to describe the K^+K^- invariant mass. The η resonance sits on top of a simple background, and is far enough away from the dominant π^0 peak that further inspection of the background is not necessary. In addition, since the η resonance is nowhere near the threshold for $\gamma\gamma$, performing any type of advanced fit to include breakup momentum and resolution effect is not necessary. Therefore, the $\gamma_1\gamma_2$ invariant mass spectra was fit by utilizing the summation of a signal function and a background function. The signal function is a Voigtian (Equation 15), which is technically a non relativistic Breit-Wigner (Equation 14) convoluted with a Gaussian. This convolution is necessary because the GlueX resolution of the η resonance is much greater than the natural width of the η meson, which is on the order of a keV. In the total signal function (Equation 15) there is one independent variable, and three fit parameters, and one fixed parameter. The independent variable is the $\gamma_1\gamma_2$ invariant mass, and the fixed parameter is the natural width of the η meson which is listed in the PDG as $\Gamma_o = 1.31 keV$. The fit parameters of the function are the amplitude, A which simply scales the function to fit the statistics, the mass value of the η for the fit μ, and the resolution of the η. The limits and starting values of all parameters are summarized in Table 4.

$$|\Delta(m)|^2 = \frac{\Gamma_o}{(m - \mu)^2 + \frac{\Gamma_o^2}{4}} \tag{14}$$

$$S(m) = A \int |\Delta(m')|^2 G(m - m')dm' \tag{15}$$

85

The background function that was chosen to describe the $\gamma\gamma$ background was a Chebyshev polynomial (Equation 16). It should be noted that the functional form of this third order polynomial is different than the one that was used to describe the K^+K^- because there is no threshold effect that has to be accounted for in the $\gamma_1\gamma_2$ invariant mass. This function has four free fit parameters with no restrictions on value due to the variability of background shapes in this analysis.

$$B(m) = C_3 * x^3 + C_2 * x^2 + C_1 * x + C_0 \tag{16}$$

Finally, the total function that was used to ultimately fit the $\gamma_1\gamma_2$ invariant mass distributions was the sum of Equation 15 and Equation 16. A summary of all parameters and functions used to fit the $\gamma_1\gamma_2$ invariant mass is given in Table 4.

Examples of different fits of the $\gamma_1\gamma_2$ invariant mass distributions have been provided in Figures[63][64][65]. Just like the examples given for the K^+K^- invariant mass fits, each figure contains a blue line which represents the total fit of the data. The total fit in this particular instance is simply the sum of a Voigtian and a third degree Chebyshev polynomial. The figures also contain a green line which represents the signal portion of the fit and a red line which represents the background portion of the fit. These are described by a Voigtian and third degree Chebyshev polynomial, respectively. Located within each plot is also a vertical arrow which is pointed in the downward direction. This arrow represents the invariant mass value of the event for which the quality factor is being calculated. Also contained within each figure is a legend with the values of the parameters for each fit.

temp_hist_eta

Entries	500
χ^2 / ndf	74.92 / 82
Eta Amplitude	0.874 ± 0.092
Eta Mass	0.5488 ± 0.0029
Eta Resolution	0.02772 ± 0.00247
p0	−4.512 ± 2.230
p1	15.2 ± 3.5
p2	−12.93 ± 2.07
p3	6.789 ± 1.784

Figure 63: A fit which will result in an extremely low quality factor due to the very few signal events in comparison to background events at the location of the arrow, or invariant mass of the event being considered.
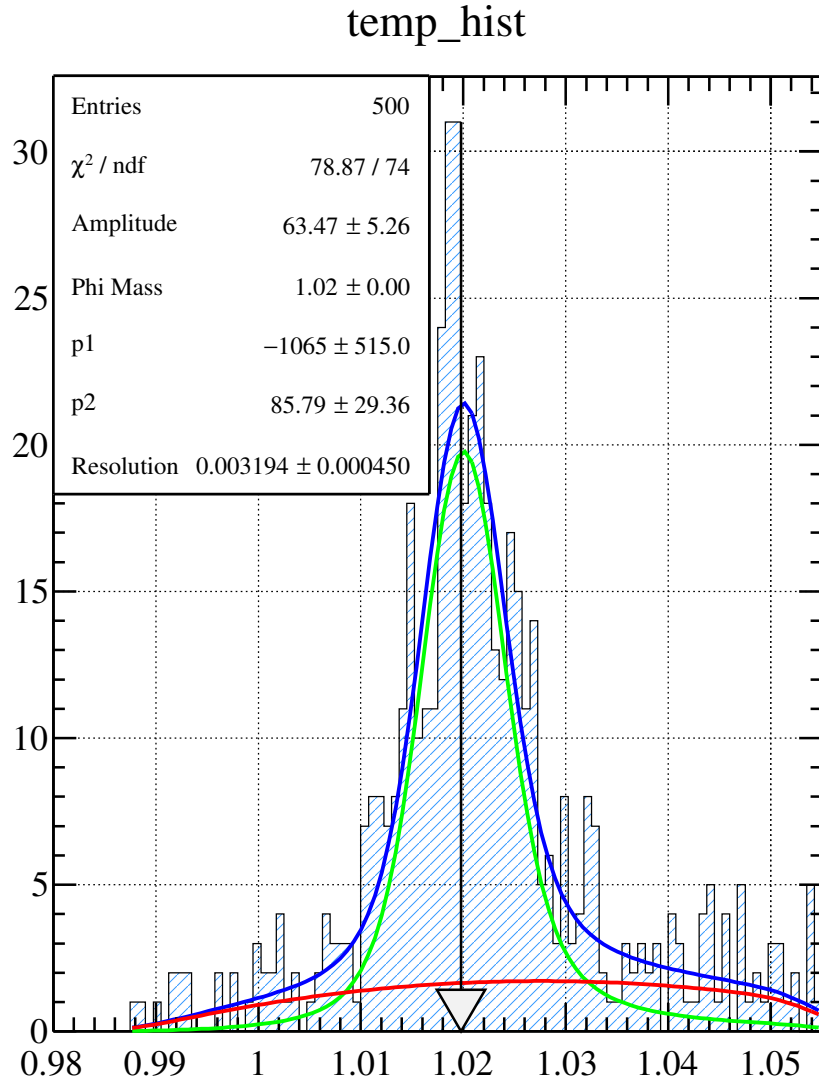
temp_hist_eta

Entries	500
χ^2 / ndf	94.08 / 91
Eta Amplitude	0.8348 ± 0.0960
Eta Mass	0.5402 ± 0.0033
Eta Resolution	0.02982 ± 0.00303
p0	−30.48 ± 2.04
p1	51.89 ± 3.23
p2	−27.04 ± 1.87
p3	6.111 ± 1.656

Figure 64: A fit which will result in a quality factor somewhat above 0.5, due to the fact that there are slightly more signal events as compared to background events at the location of the arrow, or invariant mass of the event being considered.

temp_hist_eta

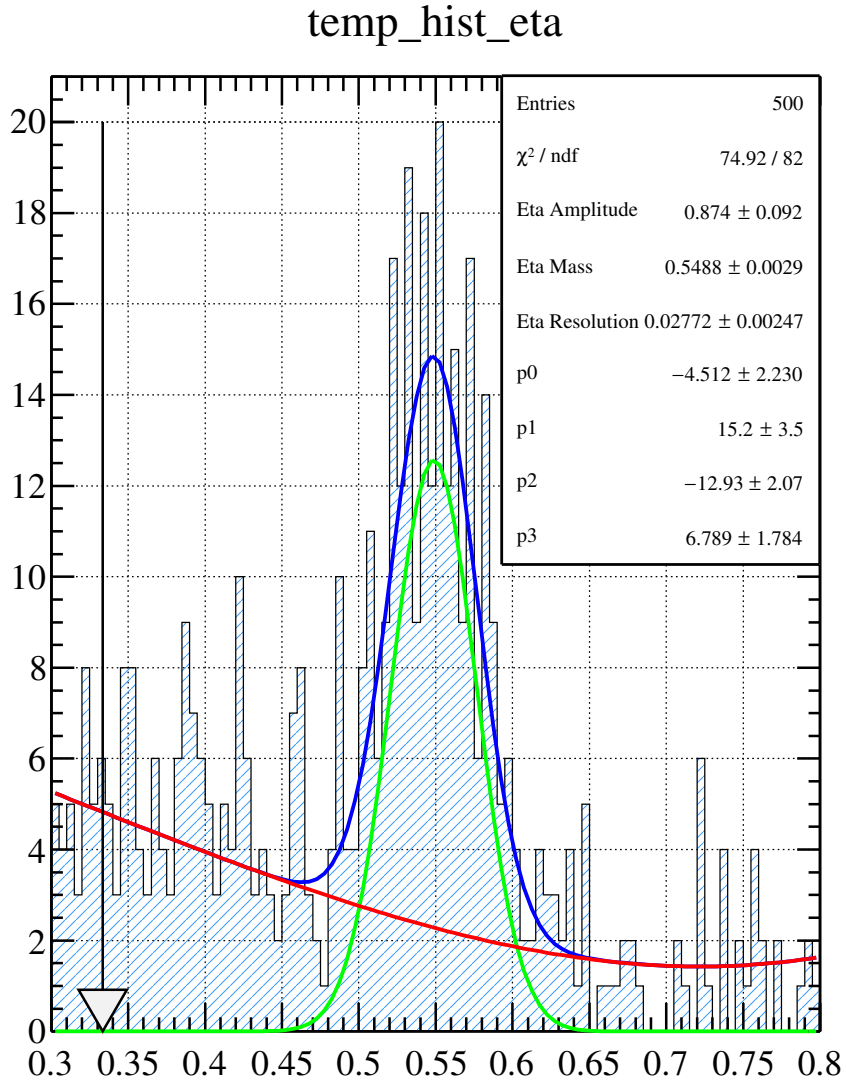| Entries | 500 |
χ² / ndf	63.65 / 78
Eta Amplitude	1.235 ± 0.099
Eta Mass	0.5404 ± 0.0019
Eta Resolution	0.02485 ± 0.00201
p0	−81.97 ± 2.15
p1	140.1 ± 3.4
p2	−73.16 ± 1.95
p3	22.12 ± 1.70

Figure 65: A fit which will result in a very high quality factor due to the large number signal events in comparison to background events at the location of the arrow, or invariant mass of the event being considered.
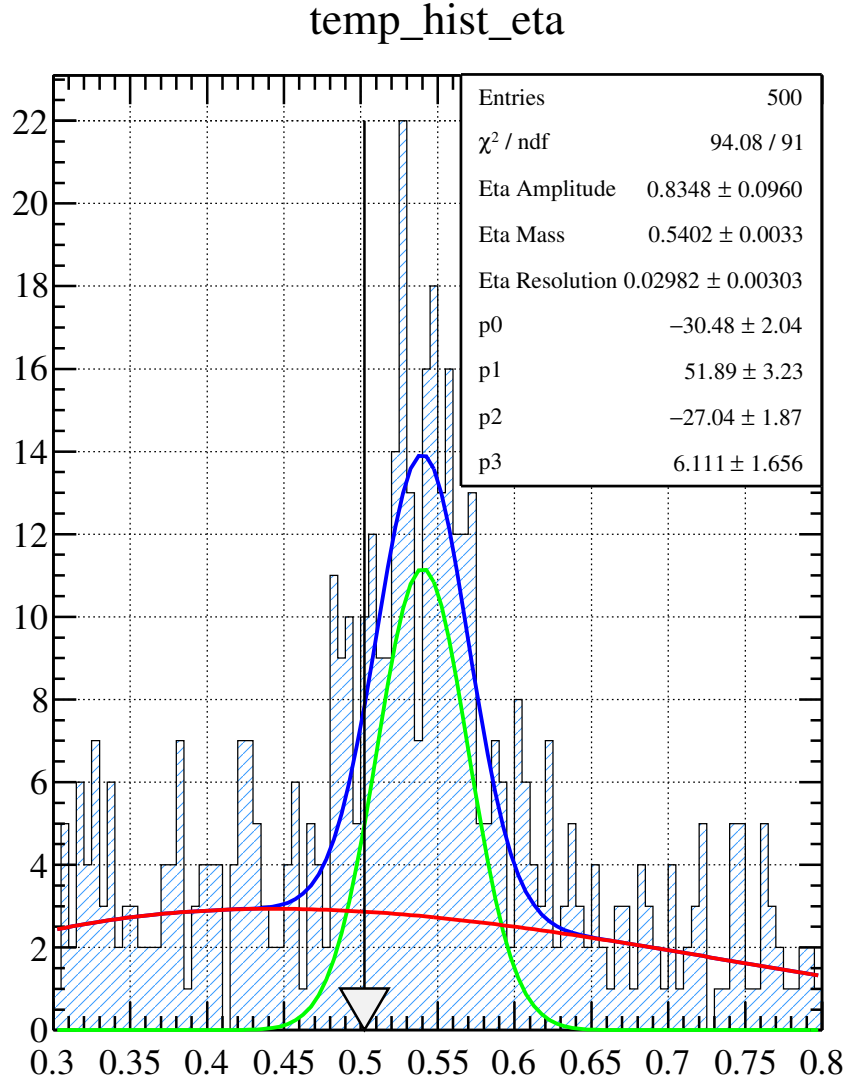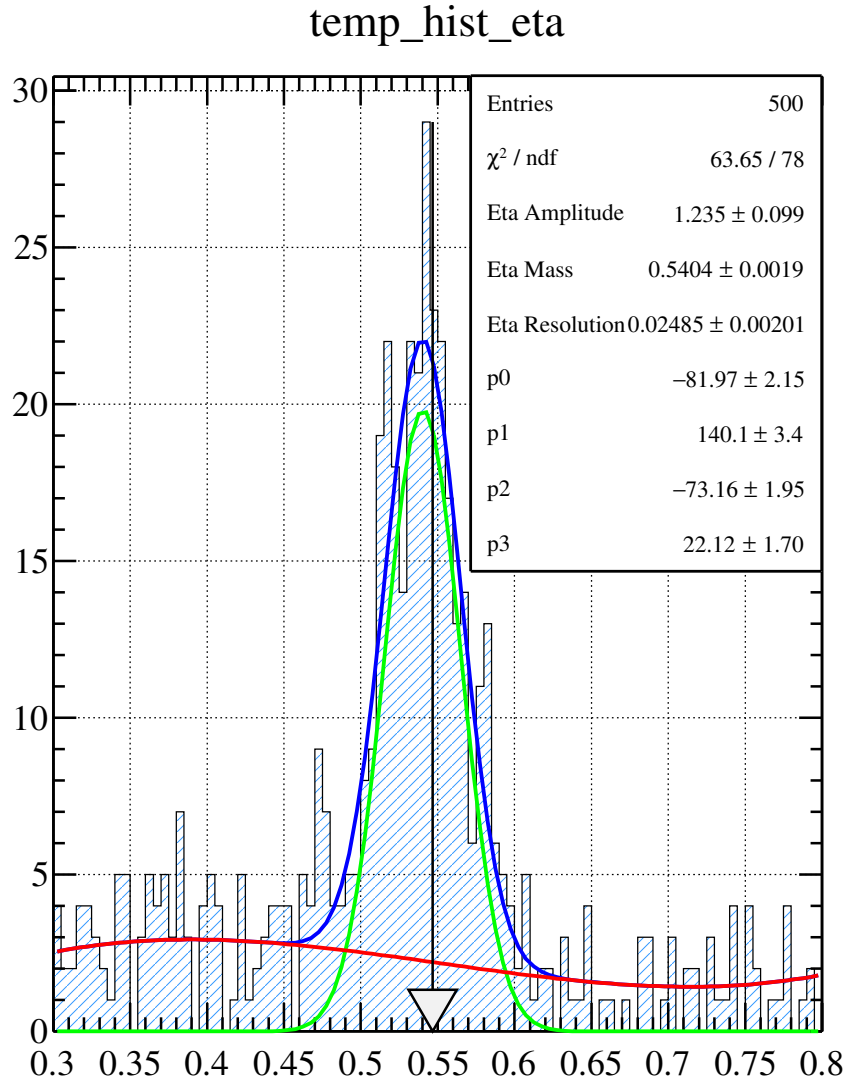
$\gamma_1 \gamma_2$ Invariant Mass Functions:

Function	Parameters	Initial Values	Restricted Range
Voigtian	Amplitude	2	$0 - 5$
	m_η	0.547	$0.52 - 0.56$
	σ	0.02	$0.001 - 0.1$
	Γ	0.00000131	Fixed
3rd Chebyshev Polynomial	C_0, C_1, C_2, C_3	None	Free

Table 4: A table which summarizes the parameters and functions used to fit the $\gamma_1 \gamma_2$ invariant mass histograms.

5.2 Three Quality Factor Methods

In order to thoroughly study the $\phi\eta$ final state, a total of three unique quality factor methods were attempted. Each of these analyses follow the standard quality factor prescription detailed in Subsection 5.1. Each analysis is unique because a different set of kinematic observables was used to find the set nearest neighbors for each event.

1. (ϕ Only) The first quality factor method considered the kinematic observables of the $K+K-$ system, and therefore can only separate the ϕ signal from the $K+K-$ background. The quality factor for this analysis will be denoted with Q_ϕ.

2. (η Only) The second quality factor method only considered the kinematics observables of the $\gamma\gamma$ system, and therefore only separates the η signal from the $\gamma\gamma$ background. The quality factor for this analysis will be denoted with Q_η.

3. ($\phi\eta$) The third and final quality factor analysis considered the kinematics observables for *both* the $K+K-$ system and the $\gamma\gamma$ system. The quality factor for this analysis will be denoted with $Q_{\phi\eta}$.

The specific list of kinematic observables and how a quality factor was calculated for each analysis is detailed in Subsections 5.2.1 and 5.2.5, respectively. It should be noted that all three analyses use the same fit functions for the K^+K^- invariant mass distribution (Subsection 5.1.2), and $\gamma\gamma$ invariant mass distribution (Subsection 5.1.3). In addition, all three analyses only accept the 500 nearest neighbors (Subsection 5.1.1).

5.2.1 Calculating the Kinematic Distance Between Events

As mentioned in Subsection 5.2 , there are a total of three unique quality factor analyses attempted in this thesis, and therefore there are three unique calculations to find the kinematic distance between events.

5.2.2 ϕ Only

The list of kinematic observables used to identify the ϕ meson and to ultimately calculate Q_ϕ are given in Table 5.

ξ_k	Coordinate	Maximum Range of Coordinate
ξ_0	$K^+_{HE\cos(\theta)}$	2
ξ_1	$K^+_{HE\phi}$	2π radians
ξ_2	$GJ, \cos(\theta)$	2
ξ_3	GJ, ϕ	2π radians
ξ_4	γ_E	4 GeV
ξ_5	t	$3.3\dfrac{GeV^2}{c^4}$
ξ_r	K^+K^- Invariant Mass	Reference Coordinate

Table 5: A table which summarizes the coordinates used to describe the $\gamma p \to pX; \ X \to \phi Y \ \phi \to K^+K^-$; final state. This set of coordinates will ultimately lead to the calculation of Q_ϕ The coordinates ξ_0 through ξ_5 are used in the kinematic distance equation, described by Equation (4). The last coordinate is the reference coordinate for this analysis.

Since this quality factor analysis is only attempting to separate the ϕ from K^+K^- background, there is no need to include any information about the η or its decay products, $\gamma\gamma$. Therefore, in order to properly identify the $\gamma p \to pX; \ X \to \phi Y \ \phi \to K^+K^-$ final state, a total of six coordinates are needed. Two of the six coordinates come from the angular distributions of the daughter states of ϕ: $K^+_{HE\cos(\theta)}$, $K^+_{HE\phi}$; where the angles ϕ and θ are the polar coordinates in the helicity reference frame, or the rest frame of the ϕ. Two more of the eight total coordinates will come from the angular distributions of ϕ. Much like the kaons, these coordinates will be $GJ, \cos(\theta)$ and GJ, ϕ; where ϕ and $\cos(\theta)$ are polar angles in the Gottfried-Jackson frame; or the rest frame of the $K^+K^-\gamma\gamma$ parent state. The last two coordinates needed are the beam energy (γ_E), and the momentum transfer, t. Since t is the well known Mandelstam variable, t is related to the beam energy and the four momentum of the $\phi\eta$ parent state, such that $t^2 = (\gamma^\mu - X^\mu)^2$; where

γ^μ is the energy-momentum four vector for the beam, and X^μ is the energy-momentum four vector for the $\phi\eta$ parent state. Since t, the beam energy γ_E, and the mass of the $K^+K^-\gamma\gamma$ parent state is known, the magnitude of the $K^+K^-\gamma\gamma$ parent state momentum is directly proportional to these measurements. Knowing the magnitude of the momentum and the mass of the $K^+K^-\gamma\gamma$ parent state allows us to fully describe the $\gamma p \to pX$; $X \to \phi Y$ $\phi \to K^+K^-$ reaction. The final detail that needs to be mentioned is the reference coordinates that are used in this quality factor analysis. Because it is imperative to have a pure ϕ signal, the reference coordinate for this procedure will be the K^+K^- invariant mass. Although this coordinate do not play a role in the calculation of the kinematic distance, it is imperative to define it as the reference coordinate which will ultimately serve as the tool to separate signal events from background events, and to calculate Q_ϕ.

5.2.3 η Only

The list of kinematic observables used to identify the η meson and to ultimately calculate Q_η are given in Table 6.

ξ_k	Coordinate	Maximum Range of Coordinate
ξ_0	$\gamma_{HE\cos(\theta)}$	2
ξ_1	$\gamma_{HE\phi}$	2π radians
ξ_2	$GJ, \cos(\theta)$	2
ξ_3	GJ, ϕ	2π radians
ξ_4	γ_E	4 GeV
ξ_5	t	$3.3\dfrac{GeV^2}{c^4}$
ξ_r	$\gamma_1\gamma_2$ Invariant Mass	Reference Coordinate

Table 6: A table which summarizes the coordinates used to describe the $\gamma p \to pX$; $X \to \eta Y$; $\eta \to \gamma\gamma$ final state. This set of coordinates will ultimately lead to the calculation of Q_η The coordinates ξ_0 through ξ_5 are used in the kinematic distance equation, described by Equation (4). The last coordinate is the reference coordinate for this analysis.

This quality factor analysis is only attempting to separate the η from $\gamma\gamma$ background, there is no need to include any information about the ϕ or its decay products, K^+K^-. Therefore, in order to properly identify the $\gamma p \to pX$; $X \to \eta Y$; $\eta \to \gamma\gamma$ final state, a total of six coordinates are needed. Two of the six coordinates come from the angular distributions of the daughter states of η: $\gamma_{HE\cos(\theta)}$, $\gamma_{HE\phi}$; where the angles ϕ and θ are the polar

coordinates in the helicity reference frame, or the rest frame of the η. Two more of the eight total coordinates will come from the angular distributions of η. Much like the photon, these coordinates will be $GJ, \cos(\theta)$ and GJ, ϕ; where ϕ and $\cos(\theta)$ are polar angles in the Gottfried-Jackson frame; or the rest frame of the $K^+ K^- \gamma\gamma$ parent state. The last two coordinates needed are the beam energy (γ_E), and the momentum transfer, t. Since t is the well known Mandelstam variable, t is related to the beam energy and the four momentum of the $\phi\eta$ parent state, such that $t^2 = (\gamma^\mu - X^\mu)^2$; where γ^μ is the energy-momentum four vector for the beam, and X^μ is the energy-momentum four vector for the $\phi\eta$ parent state. Since t, the beam energy γ_E, and the mass of the $K^+ K^- \gamma\gamma$ parent state is known, the magnitude of the $K^+ K^- \gamma\gamma$ parent state momentum is directly proportional to these measurements. Knowing the magnitude of the momentum and the mass of the $K^+ K^- \gamma\gamma$ parent state allows us to fully describe the $\gamma p \rightarrow pX$; $X \rightarrow \eta Y$; $\eta \rightarrow \gamma\gamma$ reaction. The final detail that needs to be mentioned is the reference coordinates that are used in this quality factor analysis. Because it is imperative to have a pure η signal, the reference coordinate for this procedure will be the $\gamma\gamma$ invariant mass. Although this coordinate does not play a role in the calculation of the kinematic distance, it is imperative to define it as the reference coordinate which will ultimately serve as the tool to separate signal events from background events, and to calculate Q_η.

5.2.4 $\phi\eta$

The list of kinematic observables used to identify the ϕ meson and the η meson; and to ultimately calculate $Q_{\phi\eta}$ are given in Table 7.

The final quality factor analysis is attempting to identify both the ϕ and η mesons and to also reject any background. It should be noted that the backgrounds for this analysis are different and include $\phi\gamma\gamma$, $\eta K^+ K^-$, and $K^+ K^- \gamma\gamma$. Therefore, in order to properly identify the $\gamma p \rightarrow pX$; $X \rightarrow \phi\eta$ $\phi \rightarrow K^+ K^-$; $\eta \rightarrow \gamma\gamma$ final state, a total of eight coordinates are needed. Four of the eight coordinates come from the angular distributions of the daughter states of ϕ and η. More specifically, the four coordinates are $K^+_{HE\cos(\theta)}$, $K^+_{HE\phi}$, $\gamma_{HE\cos(\theta)}$, $\gamma_{HE\phi}$; where the angles ϕ and θ are the polar coordinates in the helicity reference frame. It should be noted that since the K^+ and γ particles are daughters of different parent states, they will have different helicity frames which are relative to the rest frames of ϕ and η mesons, respectively. Two more of the eight total coordinates will come from the angular distributions of ϕ and η. Much like the K^+ and γ particles, these coordinates will be $GJ, \cos(\theta)$ and GJ, ϕ; where ϕ and $\cos(\theta)$ are polar angles in the Gottfried-Jackson frame; or the rest frame of the $\phi\eta$ parent state.

ξ_k	Coordinate	Maximum Range of Coordinate
ξ_0	$K^+_{HE\cos(\theta)}$	2
ξ_1	$K^+_{HE\phi}$	2π radians
ξ_2	$\gamma_{HE\cos(\theta)}$	2
ξ_3	$\gamma_{HE\phi}$	2π radians
ξ_4	$GJ, \cos(\theta)$	2
ξ_5	GJ, ϕ	2π radians
ξ_6	γ_E	4 GeV
ξ_7	t	$3.3\dfrac{GeV^2}{c^4}$
ξ_r	K^+K^- Invariant Mass	Reference Coordinate
ξ_r	$\gamma_1\gamma_2$ Invariant Mass	Reference Coordinate

Table 7: A table which summarizes the coordinates used to describe the $\gamma p \to pX$; $X \to \phi\eta$ $\phi \to K^+K^-$; $\eta \to \gamma\gamma$ final state. This set of coordinates will ultimately lead to the calculation of $Q_{\phi\eta}$ The coordinates ξ_0 through ξ_7 are used in the kinematic distance equation, described by Equation (4). The last two coordinates are the reference coordinates for this analysis.

The last two coordinates needed to describe the $\gamma p \to p\phi\eta$ final state is the beam energy (γ_E), and the momentum transfer, t. Since t is the well known Mandelstam variable, t is related to the beam energy and the four momentum of the $\phi\eta$ parent state, such that $t^2 = (\gamma^\mu - X^\mu)^2$; where γ^μ is the energy-momentum four vector for the beam, and X^μ is the energy-momentum four vector for the $\phi\eta$ parent state. Since t, the beam energy γ_E, and the mass of the $\phi\eta$ parent state is known, the magnitude of the $\phi\eta$ parent state momentum is directly proportional to these measurements. Knowing the magnitude of the momentum and the mass of the $\phi\eta$ parent state allows us to fully describe the $\gamma p \to p\phi\eta$ reaction. The final detail that needs to be mentioned is the reference coordinates that are used in this quality factor analysis. Because it is imperative to have a pure ϕ and η signal, there will be two reference coordinates for this procedure. One of them will be the K^+K^- invariant mass, and the other will be the $\gamma_1\gamma_2$ invariant mass. Although these coordinates do not play a role in the calculation of the kinematic distance, it is imperative to define them as the reference coordinates which will ultimately serve as the tool to separate signal events from background events, and to calculate $Q_{\phi\eta}$.

5.2.5 Calculating the Quality Factor

Once the fits of the K^+K^- and $\gamma_1\gamma_2$ invariant mass histograms have converged, the final step of calculating a quality factor can be performed. This is done by knowing the signal and background functions, as well as their fitted parameters, for both the K^+K^- and $\gamma_1\gamma_2$ distributions. Knowing the parameters of the fit will allow the user to accurately estimate the number of signal events and the number of background events for a given invariant mass value. The invariant mass value that should be used is the one which corresponds to the event that is being studied, and the parameters are determined by the fit of the invariant mass distribution of nearest neighbors. More specifically, the quality factor associated with the K^+K^- invariant mass distribution will be Equation 17.

$$Q_\phi = \frac{S(m_{KK})}{S(m_{KK}) + B(m_{KK})} \tag{17}$$

In Equation (17), the function $S(m)$ is the convoluted relativistic Breit-Wigner described by Equation (13), and the function $B(m)$ is the convoluted third degree polynomial described by Equation (12). Lastly, the m_{KK} variable describes the K^+K^- mass of the event being considered. The quality factor associated with the $\gamma_1\gamma_2$ invariant mass distribution will be Equation 18.

$$Q_\eta = \frac{S(m_{\gamma\gamma})}{S(m_{\gamma\gamma}) + B(m_{\gamma\gamma})} \tag{18}$$

In Equation 18, the function $S(m)$ is a Voigtian function, which is the convolution of a non-relativistic Breit-Wigner with a Gaussian, described by Equation 15. The function $B(m)$ is the simply a third degree Chevyshev polynomial described by Equation 16. Lastly, the $m_{\gamma\gamma}$ variable describes the $\gamma\gamma$ invariant mass of the event being considered. The last quality factor which considers both the kinematics of the ϕ and the η is given in Equation (19).

$$Q_{\phi\eta} = \frac{S(m_{KK})}{S(m_{KK}) + B(m_{KK})} * \frac{S(m_{\gamma\gamma})}{S(m_{\gamma\gamma}) + B(m_{\gamma\gamma})} \tag{19}$$

In Equation (19), the signal and background functions for the K^+K^- and $\gamma\gamma$ invariant mass distributions are the same as those mentioned in Equation 17 and Equation 18, respectively.

The key difference between all three quality factor calculations comes from the fact that they are all using a different set of kinematic variables to determine a set of nearest neighbors. Therefore, the K^+K^- invariant mass

distribution using the ϕ Only method will be different from the K^+K^- invariant mass distribution using the $\phi\eta$ method. Conversely, the $\gamma\gamma$ invariant mass distribution using the η Only method will be different from the $\gamma\gamma$ invariant mass distribution using the $\phi\eta$ method. This subtlety will result in different $\phi\eta$ invariant mass yields, depending on the quality factor method that is being considered.

5.2.6 Quality Factor Highlights

The effectiveness of the quality factor approach is highlighted in Figure 66 and Figure 67. Figure 66 shows what the K^+K^- invariant mass distribution looks like when plotting events with weights Q_ϕ and with weights $1-Q_\phi$. One can clearly see that the quality factor effectively separated the signal ϕ meson from the K^+K^- background. Figure 67 shows what the $\gamma\gamma$ invariant mass distribution looks like when plotting events with weights Q_η and with weights $1-Q_\eta$. One can clearly see that the quality factor effectively separated the signal η meson from the $\gamma\gamma$ background.
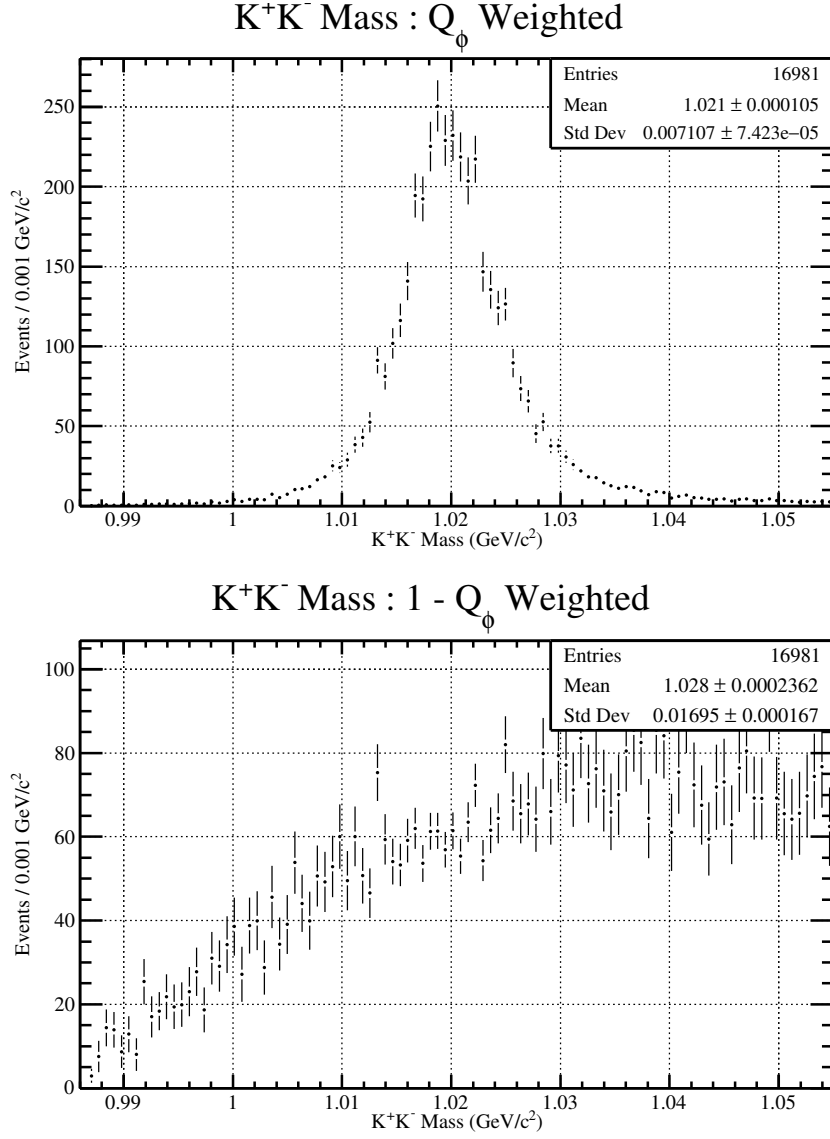
Figure 66: The K^+K^- invariant mass distribution plotted with the signal weight, Q_ϕ and the background weight $1 - Q_\phi$.
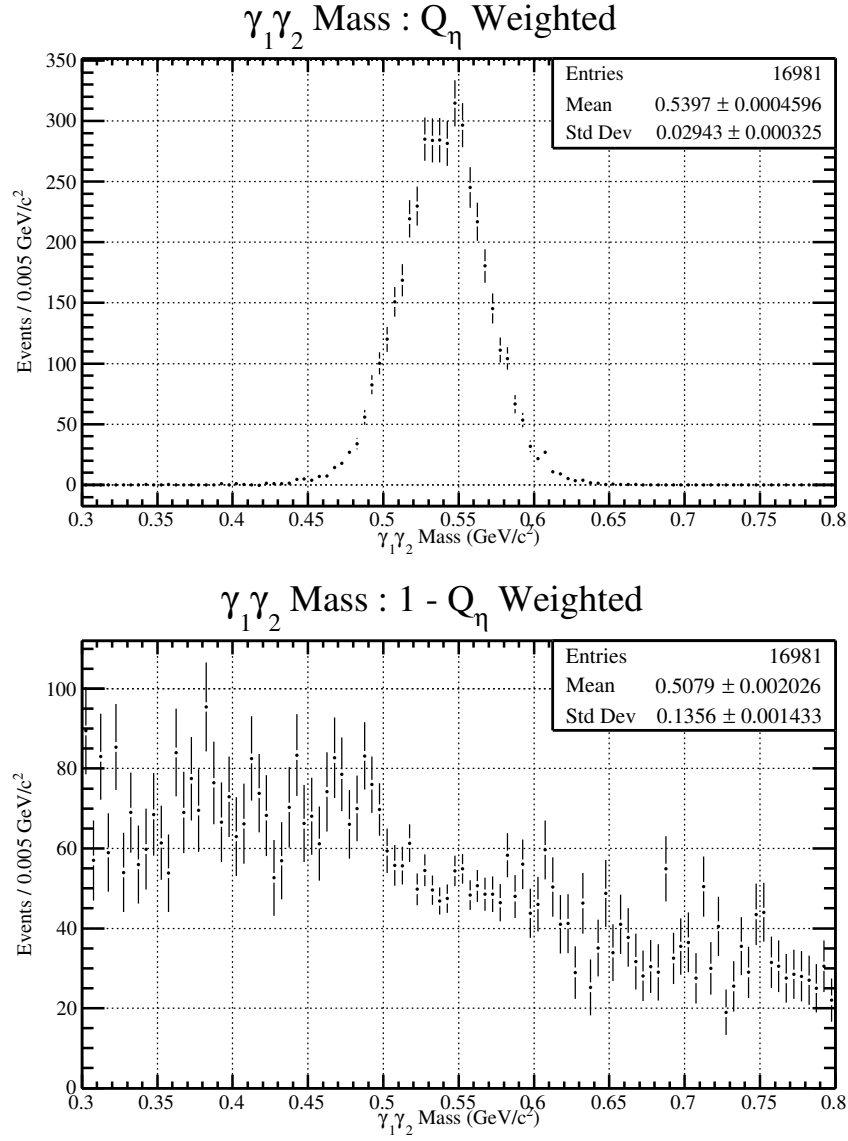
97

Figure 67: The $\gamma\gamma$ invariant mass distribution plotted with the signal weight, Q_η and the background weight $1 - Q_\eta$.

98

6   Analysis of $\phi\eta$ Invariant Mass Plot